

**3D MODELLING, SEGMENTATION, QUANTIFICATION
AND VISUALISATION OF CARDIOVASCULAR
MAGNETIC RESONANCE IMAGES**

by

Yarish Brijmohan
BScEng (Electronic) *Summa cum Laude*
MScEng (Electronic) *cum Laude*

Submitted in fulfilment of the requirements for the
Degree of Doctor of Philosophy in Electronic Engineering
in the College of Agriculture, Engineering and Science
at the University of KwaZulu-Natal, Durban

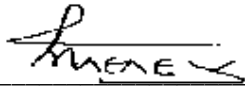
December 2014

Supervisor: Professor Stanley H. Mneney
Co-supervisor: Professor William I.D. Rae

As the candidate's Supervisor I agree to the submission of this thesis.

Date of submission : 14 January 2015

Supervisor : Professor Stanley H. Mneney

Signature : 

Declaration by Candidate:

I, Yarish Brijmohan declare that,

1. The research reported in this thesis, except where otherwise indicated, is my original research.
2. This thesis has not been submitted for any degree or examination at any other university.
3. This thesis does not contain other persons' data, pictures, graphs or other information, unless specifically acknowledged as being sourced from other persons.
4. This thesis does not contain other persons' writing, unless specifically acknowledged as being sourced from other researchers. Where other written sources have been quoted, then:
 - a. Their words have been re-written, but the general information attributed to them has been referenced.
 - b. Where their exact words have been used, then their writing has been placed in italics and inside quotation marks, and referenced.
5. This thesis does not contain text, graphics or tables copied and pasted from the Internet, unless specifically acknowledged, and the source being detailed in the thesis and in the references sections.

Name : Yarish Brijmohan

Signature : _____

Date : 14 January 2015

Acknowledgements

First and foremost, I would like to express my appreciation to God and Her Holiness Shri Mataji Nirmala Devi for inspiration, guidance and support. All work conducted by myself, is in credit to the Divine.

I wish to thank my supervisor, Professor Stanley Mneney, for his deep enthusiasm, guidance, encouragement and supervision during the course of this research. His comments throughout were constructive and insightful.

I would also like to express my sincere gratitude to my co-supervisor, Professor William I.D. Rae, for all his assistance and guidance in the research and also for all the MRI datasets from his team. The time made by him during my visits to the Free State is much appreciated.

Furthermore, I express my appreciation to my fellow engineers, N. Ramchunder, T. Khan and Y. Ramlakhan, for their assistance in proof reading my work.

Last, but not least, a heartfelt thanks to my wife, Asha, and our boys for their inspiration, support and encouragement during this period.

Abstract

Progress in technology in the field of magnetic resonance imaging (MRI) has provided medical experts with a tool to visualise the heart during the cardiac cycle. The heart contains four chambers namely the left and right ventricles and the left and right atria. Each chamber plays an important role in the circulation of blood throughout the body. Imbalances in the circulatory system can lead to several cardiovascular diseases. In routine clinical medical practice MRIs are produced in large quantities on a daily basis to assist in clinical diagnosis. In practice, the interpretation of these images is generally performed visually by medical experts due to the minimal number of automatic tools and software for extracting quantitative measures.

Segmentation refers to the process of detecting regions within an image and associating these regions with known objects. For cardiac MRI, segmentation of the heart distinguishes between different ventricles and atriums. If the segmentation of the left ventricle and right ventricle exists, doctors will be interested in quantifying the thickness of the ventricle walls, the movement of each ventricle, blood volumes, blood flow-rates, etc.

Several cardiac MRI segmentation algorithms have been developed over the past 20 years. However, much attention of these segmentation methods was afforded to the left ventricle and its functionality due to its approximately cylindrical shape. Analysis of the right ventricle also plays an important role in heart disease assessment and coupled with left ventricle analysis, will produce a more intuitive and robust diagnostic tool. Unfortunately, the crescent like shape of the right ventricle makes its mathematical modelling difficult. Another issue associated with segmenting cardiac MRI is that the quality of images can be severely degraded by artefactual signals and image noise emanating from equipment errors, patient errors and image processing errors. The presence of these artefacts attribute to additional difficulty for segmentation algorithms and many of the currently available segmentation methods cannot account for all of the abovementioned categories.

A further downfall of current segmentation algorithms is that there is no readily available standard methodology to compare the accuracy of these approaches, as each author has provided results on different cardiac MRI datasets and segmentation done by human readers (expert segmentation) is subjective. This thesis addresses the issues of accuracy comparison by providing a framework of mathematical, statistical and clinical accuracy measures. The use of publically available cardiac MRI datasets in which expert segmentation is performed is analysed. The framework allows the author of a new segmentation algorithm to choose a subset

of the measures to test their algorithm. A clinical measure is proposed in this thesis which does not require expert segmentation on the cardiac MRI dataset, where the stroke volumes of the left and right ventricle are compared to each other.

This thesis proposes a new three dimensional cardiac MRI segmentation algorithm that is able to segment both the left and right ventricles. This approach provides a robust technique that improves on the use of the difference of Gaussians (DoG) image filter. The main focus was to find and extract the region of interest that contains the ventricles and remove all the unwanted information so that the DoG parameters are created from intensity profiles of this localised region. Two methods are proposed to achieve this localisation, depending on the type of cardiac MRI dataset that is present.

The first method is used if the cardiac MRI dataset contains images from a single MRI view. Local and global motion maps are created per MRI slice using pixel intensities from images at all time points though the cardiac cycle. The segmentation results show a slight drop in evaluation metrics on the state of the art algorithms for the left ventricle and a significant improvement over the state of the art algorithms for the right ventricle using the publically available cardiac MRI datasets. The algorithm is also robust enough to withstand the influence of image noise and simulated patient movement.

The second approach to find the region of interest is used if there are MRIs from three views present in the cardiac MRI dataset. The novel method projects ventricle segmentation in the three dimensional space from two cardiac MRI views to provide an automatic ventricle localisation in the third MRI view. This method utilises an iterative approach with convergence criteria to provide final ventricle segmentation in all three MRI views. The results show increase in segmentation accuracy per iteration and a small stroke volumetric error measurement on final segmentation.

Finally, proposed in this thesis is a triangular surface mesh reconstruction algorithm to create the visualisation of both the left and right ventricles. The segmentation of the ventricles are extracted from the MRI per slice and combined to form a three dimensional point set. The use of segmentation from the three orthogonal MRI views further improves the visualisation. From the three dimensional point set, the surface mesh is constructed using Delaunay triangulation, convex hulls and alpha hulls. The volume of the ventricles are calculated by performing a high resolution voxelisation of the ventricle mesh and thereafter several quantification measures are computed. The volume methodology is compared to the commonly used Simpsons method and the results illustrate that the proposed method is superior.

Table of Contents

Acknowledgements	iii
Abstract	iv
Table of Contents	vi
List of Figures	viii
List of Tables	xi
List of Acronyms	xiii
CHAPTER 1 - INTRODUCTION	1
1.1 Motivation and Research Objectives	2
1.2 Layout of Thesis	3
1.3 Original Contributions of the Thesis	5
1.3.1 Publications	6
CHAPTER 2 - MEDICAL BACKGROUND AND MAGNETIC RESONANCE IMAGING	7
2.1 Cardiovascular System and Cycle	7
2.2 Magnetic Resonance Imaging	9
2.3 Cardiac MRI Views	12
2.4 Functions of Left and Right Ventricles	15
2.5 Effect of Cardiovascular Diseases on MRI	15
2.6 Summary	16
CHAPTER 3 - CARDIOVASCULAR MRI SEGMENTATION COMPARISON METRICS	17
3.1 Evaluation and Comparison of Segmentation Methods	17
3.2 Calculation of ventricular volumes from segmentation	29
3.3 Effectiveness of distance and statistical based measures	32
3.4 Effectiveness of clinical based measures	35
3.5 Summary	37
CHAPTER 4 - EXISTING CARDIOVASCULAR MRI SEGMENTATION APPROACHES	39
4.1 Image and Intensity Based Segmentation	39
4.2 Active Contours and Deformable Models	41
4.3 Model Based Segmentation	43

4.4	Registration Based Segmentation	47
4.5	Other Segmentation Approaches	49
4.6	Location of Region of interest for the ventricles	50
4.7	Summary	51
CHAPTER 5 - PROPOSED SEGMENTATION METHODS		52
5.1	System Overview	52
5.2	Problems in Segmenting Ventricles when using one MRI View	53
5.3	Details of the Proposed Algorithm	56
5.4	Automatic Cardiac MRI Segmentation Using Multiple Views	63
5.4.1	Segmentation by Projection	64
5.4.2	Achieving Convergence	67
5.5	Summary	68
CHAPTER 6 - PERFORMANCE OF THE PROPOSED SEGMENTATION METHODS		69
6.1	Experimental Method	69
6.2	Results for Application of Proposed Method on MRI Datasets in Short Axis View	71
6.3	Results for application of proposed method on MRI datasets that have three views	78
6.4	Summary	86
CHAPTER 7 - VISUALISATION OF CARDIAC VENTRICLES		87
7.1	Triangular Surface Mesh Reconstruction	87
7.2	Ventricle Visualisation Methods	88
7.2.1	Utilising MRI Segmentation Information from Three Views	89
7.2.2	Triangular surface mesh formation and volume calculation	90
7.3	Results of Ventricle Visualisation Method	93
7.4	Summary	96
CHAPTER 8 - CONCLUSION		97
8.1	Chapter Summaries	97
8.2	Future Work	99
REFERENCES		100

List of Figures

Figure 2-1: Cross-sectional view of a human heart clearly depicting the four chambers [8]..... 8

Figure 2-2: Wiggers diagram depicting relationship with the electrocardium, the ventricle and atrium pressures, heart sounds and ventricle volume changes [9] 8

Figure 2-3: RF pulse applied during application of gradient [3]. 10

Figure 2-4: Illustration of patient co-ordinate system and image co-ordinate system from DICOM standard [19]. 11

Figure 2-5: Cardiac MRI along different axes. The next image is in the direction of the cut (shown in yellow). 12

Figure 2-6: Examples of Cardiac MRI in Two Chamber View. (a) to (d) are per slice view depicting the left ventricle and left atrium. (e) to (h) are per slice view depicting the right ventricle and right atrium. 13

Figure 2-7: Examples of Cardiac MRI in Four Chamber View per slice. The left ventricle, left atrium, right ventricle and right atrium are visible. 14

Figure 2-8: Examples of Cardiac MRI in Short Axis View per slice. 14

Figure 3-1: SAV MRI from SCD at the end diastolic cardiac phase for a patient with no cardiac abnormalities with segmentation performed on left ventricle endocardium (blue contours) and epicardium (green contours) from the base slice (upper left image) to apex slice (lower right image) 23

Figure 3-2: : SAV MRI from SCD at the end systolic cardiac phase for a patient with no cardiac abnormalities with segmentation performed on left ventricle endocardium (blue contours)..... 23

Figure 3-3: SAV MRI from SCD at the end diastolic cardiac phase for a patient with heart failure with segmentation performed on left ventricle endocardium (blue contours) from the base slice (upper left image) to apex slice (lower right image)..... 24

Figure 3-4: SAV MRI from RVSCD at the end diastolic cardiac phase for a patient with no cardiac abnormalities with segmentation performed on right ventricle endocardium (blue contours) from the base slice (upper left image) to apex slice (lower right image) 25

Figure 3-5: SAV MRI from YUD at for entire cardiac cycle for a patient with cardiac abnormality with segmentation performed on left ventricle endocardium (red contours) and epicardium (red contours) 26

Figure 3-6: Hausdorff distance calculation on left ventricle which calculates the furthest distance that the red segmentation contour is from the ground truth blue contour. 28

Figure 3-7: Overlap measures to define region based segmentation accuracy..... 29

Figure 3-8: Segmented portions of the left ventricle in the short axis MRI view for a patient with slice thickness of 9mm. 30

Figure 3-9: Segmented portions of the left ventricle encased in a surface plot using Simpsons rule in the short axis MRI view for a patient with slice thickness of 9mm. 31

Figure 3-10: Segmentation of Right Ventricle using 273 contour points. The red arrow indicates the contour points that has moved from the ground truth representation in (a).....	32
Figure 3-11: Segmentation of Left Ventricle using 112 contour points. The red arrow indicates the contour points that has moved from the ground truth representation in (a).....	34
Figure 3-12: Stroke volume for left and right ventricles for Expert 1. Blue line represents the ideal stroke volume.	36
Figure 3-13: Stroke volume for left and right ventricles for average of three experts. Blue line represents the ideal stroke volume.	37
Figure 5-1: Block diagram of the proposed segmentation algorithm	54
Figure 5-2: Examples of MRI degraded by image noise [1]. (a) Flow artefact affecting the detection of ventricle edge. (b) Partial volume effect causing uncertainty in determining the amount of blood that is from the left or right ventricle. (c) Patient movement ó poor image quality and blood intensity not consistent. (d) Wrap around artefact in SAV. (e) Wrap around artefact in 2CV affecting ventricle edge detection.....	55
Figure 5-3: Two level discrete wavelet transform on images. (a) Block diagram of the wavelet transform process. (b) Wavelet transform of the standard deviation map.....	58
Figure 5-4: Distribution of Gaussian filters with two different sigma values and the resultant DoG filter in one dimension.	60
Figure 5-5: Application of DoG algorithm on a two dimensional cardiac MRI in the short axis view.	61
Figure 5-6: Effect of adjusting the filter width values σ_{1s} and σ_{2s}	63
Figure 5-7: Examples of MRIs obtained on different views depicting the cardiac chambers namely Left Ventricle (LV), Left Atrium (LA), Right Ventricle (RV) and Right Atrium (RA). The red circles highlights the minimal difference in pixel intensities from ventricle to atrium.....	64
Figure 5-8: Positioning of MRI slices to obtain different MRI views	64
Figure 5-9: 2 chamber view segmentation contours (magenta) of left ventricle translated to an image in 4CV in patient co-ordinate system.....	66
Figure 5-10: Short axis segmentation contours (red) of left ventricle translated to an image in 4CV in patient co-ordinate system.....	66
Figure 5-11: Region of interest for left ventricle segmentation in 4CV formed from intersecting points from SAV and 2CV segmentations.....	67
Figure 6-1: Various image filters applied to MRI to simulate noise and patient movement.....	71
Figure 6-2: Segmentation of left ventricle in the SAV performed by expert manual delineation (blue contours) and proposed algorithm (red contours) for multiple slices from a patient in the SCD dataset.	73
Figure 6-3: Segmentation of right ventricle in the SAV performed by expert manual delineation (blue contours) and proposed algorithm (red contours) for multiple slices from a patient in the RVSCD dataset. The red arrows shows the portion of the ventricle that the proposed method does not perform well in.....	74
Figure 6-4: Segmentation performed by proposed algorithm for the right ventricle on images where noise and motion effects were introduced.....	76

Figure 6-5: Segmentation of ventricle in the SAV performed by expert manual delineation (blue contour) and proposed algorithm (red contour) for a slice from a patient with Hypertrophy in the SCD dataset. The red arrow shows the portion of the ventricle that the proposed method does not perform well in.	78
Figure 6-6: Segmentation per iteration of proposed method on left ventricle for slice 6 in the short axis view.	81
Figure 6-7: Segmentation per iteration of proposed method on left ventricle for slice 3 in the 4 chamber view.	81
Figure 6-8: Segmentation of left ventricle in the SAV performed by expert manual delineation (blue contours) and proposed algorithm (red contours) for multiple slices from a patient in the UFS dataset.	83
Figure 6-9: Segmentation of right ventricle in the SAV performed by proposed algorithm (red contours) for multiple slices from a patient in the UFS dataset.	84
Figure 6-10: Segmentation of left ventricle in the 4CV performed by proposed algorithm (red contours) for multiple slices from a patient in the UFS dataset.	84
Figure 6-11: Segmentation of right ventricle in the 4CV performed by proposed algorithm (red contours) for multiple slices from a patient in the UFS dataset.	85
Figure 6-12: Segmentation of left ventricle in the 2CV performed by proposed algorithm (red contours) for multiple slices from a patient in the UFS dataset.	85
Figure 6-13: Segmentation of right ventricle in the 2CV performed by proposed algorithm (red contours) for multiple slices from a patient in the UFS dataset.	86
Figure 7-1: Delaunay Triangulation on a set of five points with circumscribed circles.	88
Figure 7-2: Delaunay Triangulation on a three dimensional point set.	88
Figure 7-3: Additional segmentation information from two chamber and four chamber MRI view (red plot) projected onto short axis segmented portions of the left ventricle encased in a surface plot using Simpsons rule.	89
Figure 7-4: Two three dimension plots of segmented area of the left and right ventricle from the two chamber view, four chamber view and short axis view.	90
Figure 7-5: Three dimensional point set of the right ventricle obtained by combining segmentation from all three MRI views.	91
Figure 7-6: Three dimensional point set (red) and Delaunay triangulation (transparent blue faces and yellow edges) of the right ventricle.	91
Figure 7-7: Alpha hull accurately represents the concaved structure of the right ventricle (blue faces and yellow edges).	92
Figure 7-8: Two mesh surface plots of segmented area of the left and right ventricle using the proposed algorithm.	94
Figure 7-9: Visual comparison of the left and right ventricle stroke volume after applying the proposed method of volume calculation.	95

List of Tables

Table 2-1: DICOM tags used to determine patient orientation [17]. 11

Table 2-2: Explanation of each DICOM tag [17]. 11

Table 3-1: Five point rating scale for expert visual assessment 19

Table 3-2: Segmentation accuracy calculation on right ventricle segmentation using various mathematical and statistical methods with the availability of the ground truth (273 contour points) 33

Table 3-3: Segmentation accuracy calculation on right ventricle segmentation using various mathematical and statistical methods with the availability of the ground truth (148 contour points) 33

Table 3-4: Segmentation accuracy calculation on left ventricle segmentation using various mathematical and statistical methods with the availability of the ground truth (112 contour points) 34

Table 3-5: Stroke volume error calculations from three experts on an MRI dataset of 10 patients. 36

Table 4-1: List of image and intensity based segmentation methods provided by various authors 40

Table 4-2: List of deformable model segmentation methods developed by various authors 43

Table 4-3: List of shape model segmentation methods developed by various authors 46

Table 4-4: List of atlas based segmentation methods developed by various authors 48

Table 4-5: List of pixel classification segmentation approaches used by various authors 50

Table 4-6: List of approaches to determine the region of interest (ROI) around heart. 50

Table 5-1: Variable definition for translation to patient coordinate system for each image p_i [7] 65

Table 6-1: Accuracy measurements of proposed segmentation method per MRI slice in the short axis view using MRIs for a patient from three datasets. 72

Table 6-2: Volumetric measurement of proposed segmentation method in the short axis view for three patients from different datasets. 75

Table 6-3: Accuracy measurements of proposed segmentation on distorted MRI in short axis view. 76

Table 6-4: Average Dice coefficient and Hausdorff distance of the proposed segmentation algorithm on the SCD dataset for patients with different pathologies. 77

Table 6-5: Comparison of Proposed segmentation algorithm with other segmentation methods on the SCD dataset for all patients with different pathologies. 77

Table 6-6: Comparison of Proposed segmentation algorithm with other segmentation methods on the RVSCD dataset for all patients with different pathologies. 77

Table 6-7: Accuracy measurements per iteration of proposed segmentation method on left ventricle per MRI slice in the short axis view at end diastolic cardiac phase. 79

Table 6-8: Accuracy measurements per iteration of proposed segmentation method on left ventricle per MRI slice in the 2 chamber view at end diastole cardiac phase. 79

Table 6-9: Accuracy measurements per iteration of proposed segmentation method on left ventricle per MRI slice in the 4 chamber view at end diastole cardiac phase. 80

Table 6-10: Volumetric measurement of proposed segmentation method in the three MRI views for a patient 80

Table 6-11: Average Dice coefficient and Hausdorff distance of the proposed segmentation algorithm in all MRI views on the UFS dataset for all 10 patients.....	82
Table 7-1: Volumetric measurements of Simpsons Rule versus Proposed method for all MRI views at the end diastolic cardiac time.....	93
Table 7-2: Stroke Volume measurements of Simpsons Rule versus Proposed method.....	94
Table 7-3: Comparison of Volumetric measurements of Simpsons Rule versus Proposed method for all MRI views at both cardiac phases for a patient whose results is obtained by using the proposed segmentation algorithm (Table 6-10).....	95

List of Acronyms

2CV	: Two Chamber View
4CV	: Four Chamber View
AAM	: Active Appearance Model
AH	: Alpha Hull
ASM	: Active Shape Model
CMRI	: Cardiovascular Magnetic Resonance Imaging
CVD	: Cardiovascular Diseases
DICOM	: Digital Imaging and Communications in Medicine
DT	: Delaunay triangulation
ED2	: Euclidean Distance 2
EDV	: End Diastolic Volume
EF	: Ejection Fraction
ESV	: End Systolic Volume
FN	: False Negative
FP	: False Positive
FV	: Faces and Vertices
HAUS	: Hausdorff Distance Measure
HH	: High/High
HL	: High/Low
ICM	: Independent Component Analysis
JAC	: Jaccard Index Measure
LA	: Left Atrium
LH	: Low/High
LL	: Low/Low
LPS	: Left, Posterior, Superior
LV	: Left Ventricle
MRI	: Magnetic Resonance Imaging or Magnetic Resonance Image
MRIs	: Magnetic Resonance Images
MSE	: Mean Square Error
NEMA	: National Electrical Manufacturers Association
PCA	: Principal Component Analysis
RA	: Right Atrium
RAAM	: Robust Active Appearance Model
RCS	: Reference Coordinate System

RF : Radio Frequency
RV : Right Ventricle
RVSCD : Right Ventricle Segmentation Challenge Data
SAV : Short Axis View
SCD : Sunnybrook Cardiac Data
SENS : Sensitivity Measure
SV : Stroke Volume
SVM : Support Vector Machines
T1 : Longitudinal Relaxation Time T1
T2 : Transverse Relaxation Time T2
TP : True Positive
UFS : University of the Free State
YUD : The York University Dataset

CHAPTER 1 - INTRODUCTION

Cardiovascular magnetic resonance imaging (CMRI) is a medical imaging method applied to the cardiovascular system that allows the simultaneous visualisation and analysis of both cardiac function and anatomy [4]. It is based on the same principles as magnetic resonance imaging (MRI), but with optimisation for the cardiovascular system. One of the main components of the cardiovascular system is the heart. The human heart is a powerful muscular organ that maintains blood circulation through the body. It contains four chambers namely the left and right ventricles and the left and right atria. The left and right ventricles are adjoined, separated by a wall, with each supporting one of two different circulations. The systemic circulation is maintained by the left ventricle and pumps blood to the organ tissues, the brain, and the rest of the body, while the pulmonary circulation is maintained by the right ventricle which pumps blood through the pulmonary artery and the lungs.

Imbalances in the circulation system lead to cardiovascular diseases (CVD) such as: coronary heart disease, arrhythmia, acute myocardial infarction (heart attack), congestive heart failure, hypertension (forcing the heart to pump against higher pressures), congenital heart diseases (defects or holes between the ventricles), etc. CVD is one of the most common causes of death [5], accounting for 30% of all global deaths in 2008, according to the World Health Organisation. Thus it is essential to diagnose cardiac diseases at the earliest stages.

To date, adult cardiology deals mostly with the left ventricle, hence the kinematics of the right ventricle is not as well-understood as that of the left, although this is slowly changing [1]. Imaging is more difficult due to its thin wall and asymmetric geometry [6], [7]. However, abnormalities in right ventricular function are also associated with a number of life-threatening defects. Also, right ventricle dysfunction can also adversely affect the left ventricle and can lead to heart failure [8]. Unfortunately, because of its different shape and pressures, much of the research on the left ventricle functional assessment cannot be easily transferred to the right ventricle.

In routine clinical medical practice images are produced in large quantities on a daily basis to assist in diagnosis of internal bodily ailments, such as CVD. Improvements in CMRI now provide more detailed anatomical and functional information about the heart and are gaining more importance in CVD diagnosis. However, in practice, the interpretation of these images is generally performed visually due to the minimal presence of automatic tools and software for

extracting quantitative measures. Visual inspection of images performed by human readers or experts is subjective and unreliable. It is thus necessary to have efficient and powerful computer vision techniques to aid and speed up visualisation and analysis of such images. These techniques or algorithms, that automatically identify region of interest in CMRI, are intended to support medical experts in their work.

Segmentation refers to the process of detecting regions within an image and associating these regions with known objects. In other words, segmentation of the medical image distinguishes between different organs, tissues, vessels, blood flow, etc. A precise segmentation allows not only a better visualisation of the object but also makes it possible to quantify that particular area of interest and provide further meaningful information. For example from the MRIs of a human heart, if segmentation of the left and right ventricles exist, doctors will be interested in quantifying the thickness of the ventricle walls, the movement of each ventricle, blood volumes, blood flow-rates, etc. [9] .

1.1 Motivation and Research Objectives

Over the last 20 years, various segmentation techniques for CMRI have been developed [2]. During this time, much attention was afforded to the left ventricle and its functionality due to the cylindrical shape [1] in the short axis MRI view (SAV). This made the left ventricle easy to locate and identify. Thus mathematical shape modelling was possible. Analysis of the right ventricle also plays an important role in heart disease detection and coupled with left ventricle analysis produce a more intuitive diagnosis tool. Unfortunately, the crescent like shape of the right ventricle makes mathematical modelling difficult.

The research topic was formulated on a visit to the University of the Free State, Medical Physics department in February 2008. There was a genuine need by Professor William I.D. Rae and his team, at the Medical Physics department to perform research into the understanding of the right ventricle of the human heart via magnetic resonance imaging, in terms of volumetric calculation and relation to diseases. Hence collaboration was then created between the University of the Free State, Medical Physics department and the University of KwaZulu-Natal, Electronic Engineering department, where research information, results and MRIs were shared and discussed. Ethical approval was obtained through the University of the Free State Ethics Committee (ETOVS NR 56/08).

The main focus areas of this research was to:

- a) Develop and implement a robust three dimensional segmentation algorithm of the human heart, which focussed on:
 - i. Automating the identification process of the left and right ventricle.
 - ii. Utilising multiple CMRI data sets, from multiple planes, which need not be orthogonal to each other.
 - iii. Defining the spatial relationship between the images from different imaging directions.
 - iv. Improving existing shape and intensity models.
 - v. Providing time-continuous segmentation over the full cardiac cycle.
- b) Calculate clinical measures of ventricle functionality such as volume and flow-rate.
- c) Develop a set of mathematical, statistical and clinical methods for the validation of segmentation and quantification models.

1.2 Layout of Thesis

This thesis concerns itself with ventricle segmentation methods performed on cardiac MRI. Thus the first four chapters of this thesis are dedicated in building up the theoretical ground work of these segmentation systems. Furthermore, these chapters provide a literature review of the most commonly used segmentation and evaluation methods developed. The following two chapters utilise specific properties of the segmentation methods highlighted in the literature review, to propose and assess the performance of a new three dimensional ventricle segmentation system.

Chapter 2 provides an introduction to cardiovascular systems and the functioning of the human heart. Thereafter the technology of MRI creation of the heart is discussed and the acquisition of heart images in three different MRI views are presented. Several relevant clinical terms and parameters are introduced to assess and quantify the function of the ventricles. Measurement of these parameters could determine the type of cardiovascular disease that is listed in this chapter.

Chapter 3 addresses the issue of non-standard methodology of comparing the different segmentation algorithms developed by various authors. Discussions of accuracy, precision and efficiency measures of cardiac MRI segmentation algorithms are presented by means of a series of mathematical, statistical and clinical evaluation criteria. Since all published results of segmentation algorithms were not applied to the same cardiac MRI dataset, this chapter provides details of three publically available MRI datasets. Finally, a clinical measure for

evaluation is proposed that does not require a comparison to an expert segmented MRI dataset, but instead requires both left and right ventricle segmentation.

A literature review of existing ventricle MRI segmentation algorithms is provided in Chapter 4. The algorithms or methods are split into four categories namely; image based or intensity models, active contours or deformable, model based and registration based methods and each is discussed in a separate sub-section. The state of art methods for each category is tabled, which provide the specific method used, the ventricle that is segmented and type of MRI dataset used. Finally a discussion of the strengths and weaknesses of each category is presented.

Having embarked on this literary and theoretical review of cardiac MRI segmentation methods, a new three dimensional ventricle segmentation system is proposed in Chapter 5. This segmentation algorithm uses image and intensity based methods combined with three dimensional information from ventricle motion as well as ventricle segmentation from other three cardiac MRI views. This chapter initially presents an outline of the ventricle segmentation system, focussing on the major sub-systems. Thereafter, the entire proposed algorithm is analysed in detail. For each component in the algorithm reasons for choice as well as effectiveness in segmentation are presented. Two proposed methods that aid in the localisation of the ventricles are presented, depending on the MRI information available from the respective cardiac MRI dataset.

Chapter 6 provides details all results obtained during the complete evaluation of the proposed three dimensional ventricle segmentation system. The chapter starts off by defining the platform and testing methods to be used in the evaluation. For the initial testing, the proposed segmentation method focusing on the short axis view is evaluated and compared to other state of the art segmentation systems using the same cardiac MRI dataset. The next set of results assess the proposed segmentation system that utilises MRIs from all three views obtained from the locally created dataset at the University of the Free State. Finally all results achieved during the testing phase are presented and accounted for.

The last chapter, Chapter 7, summarises all important points highlighted throughout this thesis in a methodical manner. A discussion of the strengths and weaknesses of the proposed segmentation system is presented. Based on this discussion, possible improvements and future research are proposed.

1.3 Original Contributions of the Thesis

The main aim of this research was to develop and recommend the best automatic left and right ventricle segmentation method or approach to be performed on cardiac MRI. To achieve this, a framework for accuracy evaluation and comparison of cardiac MRI segmentation algorithms is presented. A five point rating scale is introduced to minimise the subjectivity of expert visual assessment of the segmentation on a set of cardiac MRI. It is recommended that authors of segmentation algorithms utilise the publically available cardiac MRI datasets and the proposed framework to publish their segmentation accuracy results. The effectiveness of commonly used mathematical and statistical segmentation accuracy measures against the ground truth is presented and assessed. The framework concludes by proposing the use of the clinical measure of stroke volume to calculate the accuracy of the segmentation of the left and right ventricles when ground truth segmentation is not available.

A novel and robust three dimensional automatic segmentation algorithm of both the left and right ventricles is developed in this thesis. The algorithm utilises the segmentation information provided in the two chamber, four chamber and short axis MRI views. It also involves an iterative process with convergence criteria to obtain ventricle segmentation in all three MRI views. The heart of the approach uses the Difference of Gaussian edge or feature detection filter by creating a method that automatically chooses the Difference of Gaussian parameters from intensity profiles within the region of interest per MRI.

For segmentation of a cardiac MRI datasets that only contain the short axis view, the segmentation is adjusted by locating the ventricle regions of interest from motion maps for consecutive images in the cardiac cycle as well as from a reference image which is the end systolic cardiac time. Thus local and global motion during the cardiac cycle was tracked. A comprehensive performance evaluation of the proposed system was conducted for both approaches. The results portrayed that the proposed algorithm performs on average better than the state of the art methods, especially on the right ventricle. Furthermore, the closeness to the ground truth by the segmentation is validated through the use of the evaluation framework.

Finally, the ventricle volume calculation is improved by combining segmentation from three cardiac MRI views for both left and right ventricle. This proposed technique constructs a surface mesh around the outer segmentation points from three MRI views using Delaunay triangulation, convex hulls and alpha hulls. A novel method of calculating the alpha radius for the alpha shape is developed in order to account for the right ventricle concave structure. The

left and right ventricle volume is contained within the surface mesh using the ray tracing mesh voxelisation technique.

1.3.1 Publications

- a) Y. Brijmohan, S.H. Mneney, W.I.D. Rae, "Improvement of Ventricle Volumetric Calculation and Visualization in Cardiac MR", World Congress on Medical Physics and Biomedical Engineering, June 1-12, 2015.
- b) Y. Brijmohan, S.H. Mneney, W.I.D. Rae, "Mathematical, Statistical and Clinical Methods for the Evaluation of Segmentation Algorithms as used in Cardiac MRI" ó submitted to SAIEE Africa Research Journal ó Awaiting feedback.
- c) Y. Brijmohan, S.H. Mneney, W.I.D. Rae, "Automatic Cardiac MRI Segmentation Using Multiple Views" ó submitted to IEEE Transaction of Biomedical Engineering ó Awaiting feedback.
- d) A. Moodley, W.I.D. Rae, Y. Brijmohan, et al. "The Impact of Optic Nerve Movement on Optic Nerve Magnetic Resonance Diffusion Parameters", South African Journal of Radiology, Vol. 18(1), 2014 ó Proposed algorithm used to track motion of the eye on MRIs.

CHAPTER 2 - MEDICAL BACKGROUND AND MAGNETIC RESONANCE IMAGING

The understanding of the function and makeup of the human heart is fundamental prior to development of any segmentation algorithms. This chapter provides an introductory material and gives detail on how imaging of the heart is acquired. Section 2.1 is dedicated in providing the medical background for the circulation of blood via expansion and contraction of the ventricles. The following section, Section 2.2, shows how all the four chambers of the heart can be visualised via magnetic resonance imaging. The viewing or imaging planes can be adjusted as demonstrated in Section 2.3. The resultant images from each plane provides different shapes and angles of the ventricles. Once the ventricles are segmented, volumes and clinical metrics can be calculated, as shown in Section 2.4, which can aid in disease diagnosis. Several common causes of cardiovascular diseases are listed in Section 2.5.

2.1 Cardiovascular System and Cycle

The cardiovascular system contains the heart and a closed circuit of vessels such as arteries, veins and capillaries. The heart is a muscular pumping device that circulates blood throughout the body through this circuit of vessels. The heart is divided into four chambers (two atria and two ventricles) as shown in Figure 2-1. The atria receive blood coming into the heart, while the ventricles pump blood out of the heart [10] [11]. The events of a cardiovascular system consist of:

- a) Deoxygenated blood entering the right atrium.
- b) When the right atrium is filled, blood is injected into the right ventricle (RV).
- c) On contraction of the RV, blood is pumped through the pulmonary valve to the lungs. This is known as the pulmonary circulation.
- d) The lungs extract the carbon dioxide and water from the blood and oxygen is absorbed.
- e) This oxygenated blood returns to the heart to the left atrium.
- f) Thereafter the blood is injected into the left ventricle (LV), via the mitral valve.
- g) The blood is then pumped, on contraction of the LV, into the aorta and the rest of the body. This is known as the systemic circulation.

Valves of the Heart

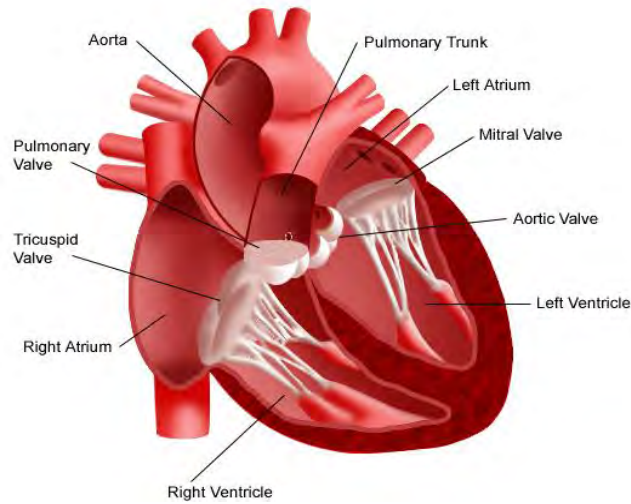


Figure 2-1: Cross-sectional view of a human heart clearly depicting the four chambers [8]

The pulmonary and systemic circulation occurs simultaneously during the cardiac cycle (or complete heartbeat). In terms of times, the cardiac cycle is divided into two sequential phases namely diastole, which is the period of chamber relaxation or filling, and systole, which is the period of chamber contraction or ejection. The Wiggers diagram [13] is a standard diagram used in cardiac physiology that provides a combined representation of the heart's electrical activity, chamber pressures and ventricle volumes during a cardiac cycle. This is graphically represented in Figure 2-2, for the left ventricle and atrium.

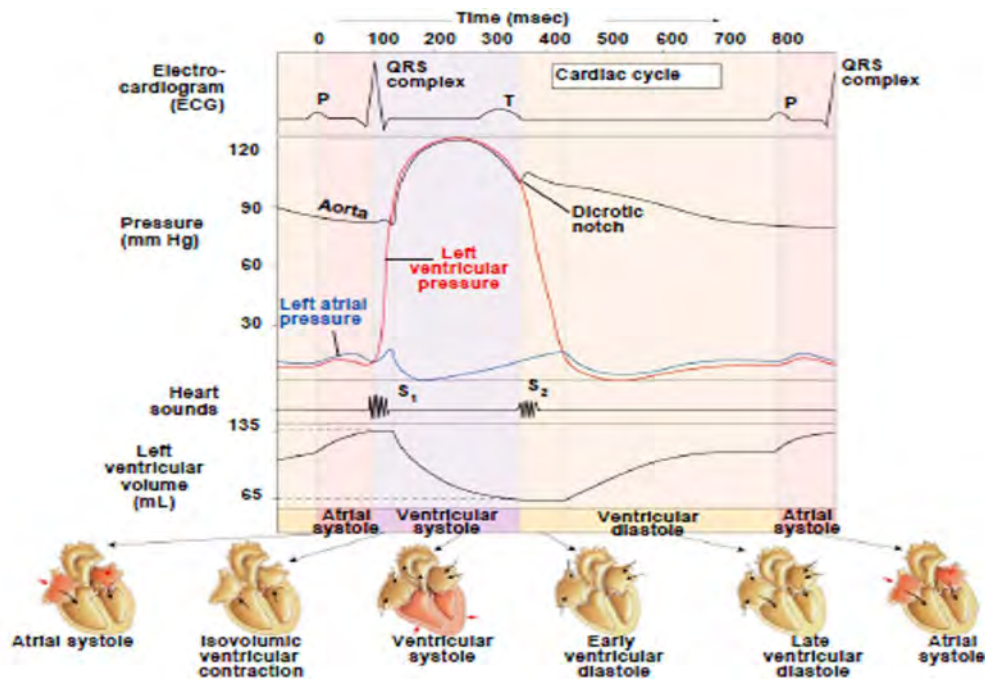


Figure 2-2: Wiggers diagram depicting relationship with the electrocardium, the ventricle and atrium pressures, heart sounds and ventricle volume changes [9]

The heart rate, normally measured in beats per minute, is the frequency of the cardiac cycle. Ventricular systole begins at the apex of the heart and the blood is squeezed to the base of the heart during ventricular contraction [14]. This causes an increase in ventricle pressure, as can be seen at time 200ms in Figure 2-2, and a decrease in blood volume. At the end of contraction, the ventricles relax with rapid pressure reduction in the chambers. During the ventricular diastole period, the volume of blood in the ventricles begin to increase, resulting in an increased ventricular size. To maintain an optimal cardiovascular system, the amount of blood leaving and entering both the ventricles must be the same.

2.2 Magnetic Resonance Imaging

Biological tissues consist mainly of water molecules which contain hydrogen atoms. Magnetic resonance imaging uses the signal from the nuclei of these atoms to produce images [3]. The nucleus of the hydrogen atom contains a proton having a positive charge and an electron having a negative charge, while it being neutral. MRI relies on the magnetic properties of these protons. The protons possess a spin of angular momentum, which induces a magnetic field, coincident with the axis of spin. When the protons are placed in a strong magnetic field, the induced magnetic field of the protons (axis of spin), aligns itself with the applied magnetic field. Thereafter by applying radio-frequency (RF) pulses, the alignment of the protons are disturbed and brought out of their equilibrium state. During the relaxation period when the proton returns to its equilibrium state, a RF pulse having the same frequency is emitted [15]. A receiver coil measures the amplitude and relaxation time of the received signal to generate the image.

The intensity or contrast of the image created at the receiver coil depends on three features of biological tissue [3], namely:

- a) Proton density, which is the number of excitable proton spins per unit volume, determines the maximum signal that can be obtained from a given tissue.
- b) Longitudinal Relaxation time T_1 , which is the time it takes for the excited spins to recover and be available for the next excitation.
- c) Transverse Relaxation time T_2 , which is time that the signal fades after excitation.

Thus MRIs are constructed based on these metrics, by varying the timing of the RF pulses.

MRI generates cross-sectional images of the human body [3]. Each of these images is known as a MRI slice and consist of a two dimensional matrix of pixels. To construct an MRI slice for a particular region within the body a linear magnetic field gradient is introduced during the period that the RF pulse is applied [16]. Gradients are additional magnetic fields that are generated by

gradient coils which adds to or subtracts from the main magnetic field. The process of obtaining an MRI slices is depicted in Figure 2-3, where an application of a strong gradient (red line) yields a thin slice, whereas the application of a weak gradient (green line) produces a thicker slice. The slice position is obtained by changing the centre frequency of the applied RF pulse. As a result, the frequency and phase of the applied RF pulse enables unique spatial identification of each volume element in the body, which is known as a voxel. Thus each pixel of an MRI provides information on a corresponding voxel [3].

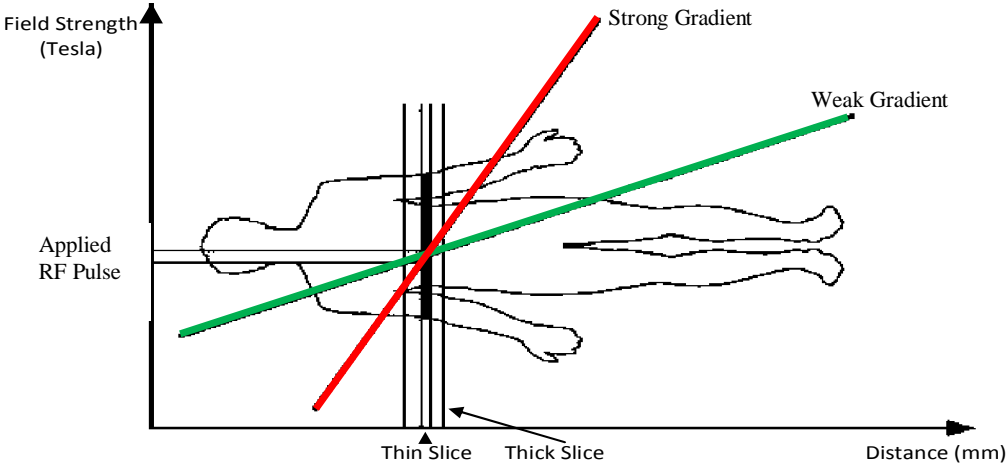


Figure 2-3: RF pulse applied during application of gradient [3].

To enable interoperability amongst different manufacturers of MRI equipment, the DICOM (Digital Imaging and Communications in Medicine) standard was created, which defines the method for the transmission of medical images and accompanying data. DICOM was originally developed by the National Electrical Manufacturers Association (NEMA) and the American College of Radiology for computerised axial tomography and magnetic resonance imaging scan images [17]. In this standard, a medical directory structure is specified to contain all patient metadata, as well as guidelines on how to perform an MRI on a patient, more specifically the orientation of the patient. MRIs are presented in the image co-ordinate system and are contained in DICOM format which provide information about the patient co-ordinate system.

DICOM defines the reference co-ordinate system (RCS) [18] or patient co-ordinate system or Left, Posterior, Superior (LPS) [19] relative to the MRI machine. The direction of the axes is defined fully by the patient's orientation. The x-axis is increasing to the left hand side of the patient. The y-axis is increasing to the posterior (back) side of the patient. The z-axis is increasing toward the superior (head) of the patient. Figure 2-4 depicts this co-ordinate system graphically.

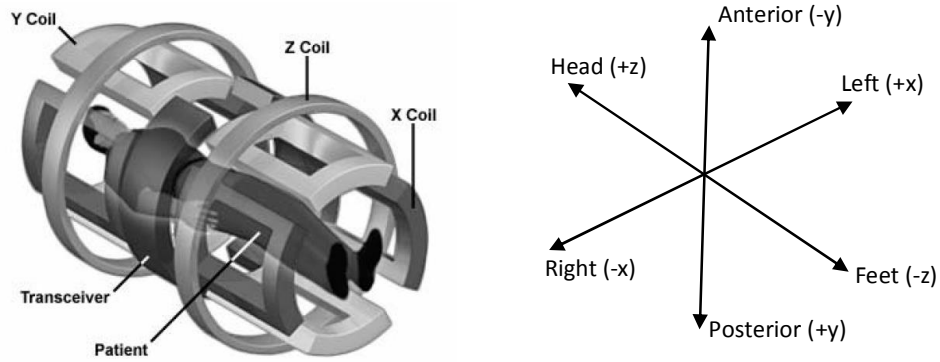


Figure 2-4: Illustration of patient co-ordinate system and image co-ordinate system from DICOM standard [19].

Table 2-1 presents the parameters in the DICOM header (from each MRI) that are important in translating points from image co-ordinate system to points in the patient co-ordinate system and Table 2-2 provides a detailed expansion and explanation of the DICOM tags.

Table 2-1: DICOM tags used to determine patient orientation [17].

Parameter Name	DICOM Tag	Parameter Description
Image Position	(0020,0032)	The x, y and z co-ordinates of the upper left hand corner of the image (centre of the first voxel transmitted) in mm.
Image Orientation	(0020,0037)	The direction of the cosines of the first row and first column with respect to the patient.
Pixel Spacing	(0028,0030)	Physical distance in the patient between the centre of each pixel in mm.
Slice Thickness	(0018,0050)	Nominal slice thickness, in mm.
Slice Location	(0020,1041)	Relative position of the image plane, expressed in mm.

Table 2-2: Explanation of each DICOM tag [17].

Parameter Name	Parameter Expansion	Parameter Description
Image Position	ImagePosition(1)=sx ImagePosition(2)=sy ImagePosition(3)=sz	x co-ordinate in patient co-ordinate system. y co-ordinate in patient co-ordinate system z co-ordinate in patient co-ordinate system
Image Orientation	ImageOrientation(1) = xxdi ImageOrientation(2) = xydi ImageOrientation(3) = xzdi ImageOrientation(4) = yxdj ImageOrientation(5) = yydj ImageOrientation(6) = yzdj	Direction of cosine of row x to x in patient Direction of cosine of row x to y in patient Direction of cosine of row x to z in patient Direction of cosine of row y to x in patient Direction of cosine of row y to y in patient Direction of cosine of row y to z in patient
Pixel Spacing	PixelSpacing(1) = PSi PixelSpacing(2) = PSj	Physical distance between x points in image. Physical distance between y points in image.

Thus each point (i, j) in the MRI (image co-ordinate system) is translated to the patient co-ordinate system point (x, y, z) as shown in (2.1), where the definitions are provided in Table

2-2. The matrix provided in (2.1) is invertible as the determinant will not be zero, thus the image co-ordinates can be obtained from the patient co-ordinates.

$$\begin{bmatrix} x \\ y \\ z \end{bmatrix} = \begin{bmatrix} xxdi & yxdj & sx \\ xydi & yydj & sy \\ xzdi & xzdj & sz \end{bmatrix} \begin{bmatrix} i \times PSi \\ j \times PSj \\ 1 \end{bmatrix}. \quad (2.1)$$

2.3 Cardiac MRI Views

The standard procedure to obtain CMRI is to perform slices in three views namely two chamber view (2CV), four chamber view (4CV) and short axis view (SAV) [1]. Images in each of these views have a link to the patient co-ordinate system. In each view, several slices can be obtained normally from the apex of the ventricle to the base of the ventricle. However, in routine cardiac MRI, only one slice is imaged in the 2CV and 4CV which is used for positioning purposes [1]. Figure 2-5 shows the direction of the slices or gradients required to obtain the specific view. The first image (coronal view) is obtained by taking slices perpendicular to the y-axis in the patient co-ordinate system and the transverse plane is achieved by slices perpendicular to the z-axis.

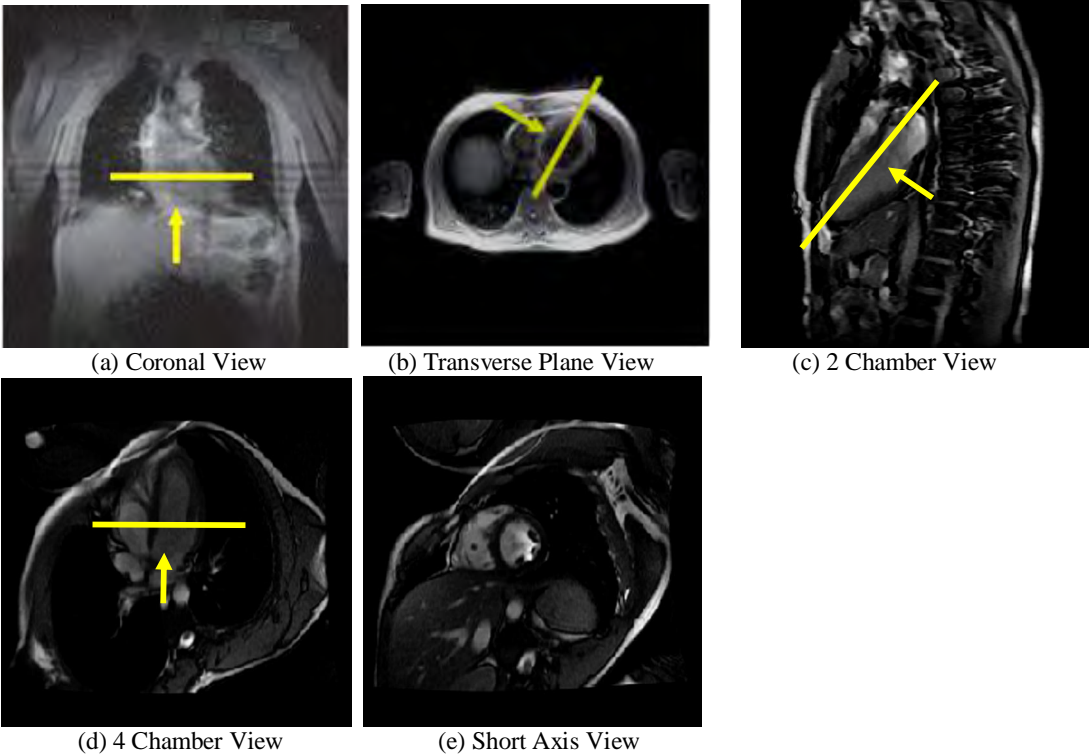


Figure 2-5: Cardiac MRI along different axes. The next image is in the direction of the cut (shown in yellow).

The 2CV is created by slices through the heart where only two chambers are visible on the same image. The chambers are either the left ventricle and left atrium, or right ventricle and right atrium. Figure 2-6 depicts four slices taken in the 2CV for the left hand side and right hand side chambers. On average, 6 slices are required to fully encompass the two ventricles [1]. From Figure 2-6 it can be seen that there is no visual distinction between the ventricle and the atrium, with both having similar intensities and contrasts. This poses a problem for segmentation in the 2CV view.

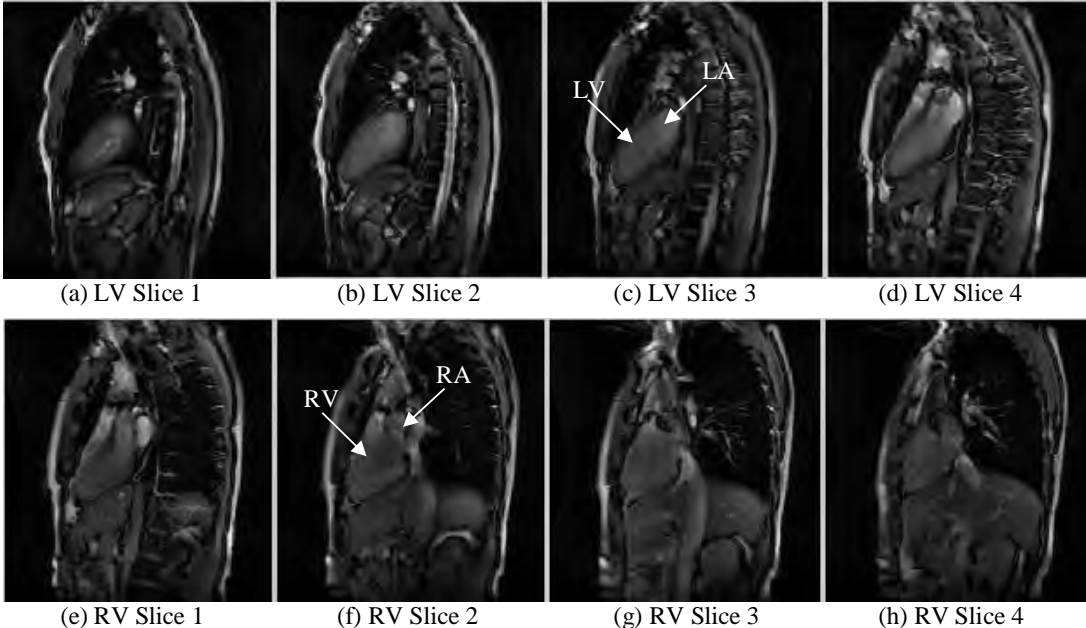


Figure 2-6: Examples of Cardiac MRI in Two Chamber View. (a) to (d) are per slice view depicting the left ventricle and left atrium. (e) to (h) are per slice view depicting the right ventricle and right atrium.

The 4CV provides visualisation of all four chambers on a single MRI as shown in Figure 2-7. It can be seen that overlapping pixel intensity and contrast between the ventricle and the atrium existing, making segmentation difficult. Furthermore, the shape of the ventricles and atrium varies per slice. A certain degree of overlap is also present at the end of Slice 1 and Slice 6. On an average, 6 slices are required to fully visualise the ventricles.

The SAV provides MRI slices where the left and right ventricles are visible on the same image. Figure 2-8 provides ten MRI slices in the SAV, which is the average number required to fully visualise the ventricles. The left ventricle shape is circular, whereas the right is a crescent. At the end slices, Slice 1 and Slice 10, the shape of the ventricle are distorted. A further complication in the ventricle is the presence of the papillary muscle. Some authors choose to include papillary in the segmentation and some do not [20]. Another artefact present is the wrap around effect, where the bottom of the image appears at the top as indicated in Slice 9.

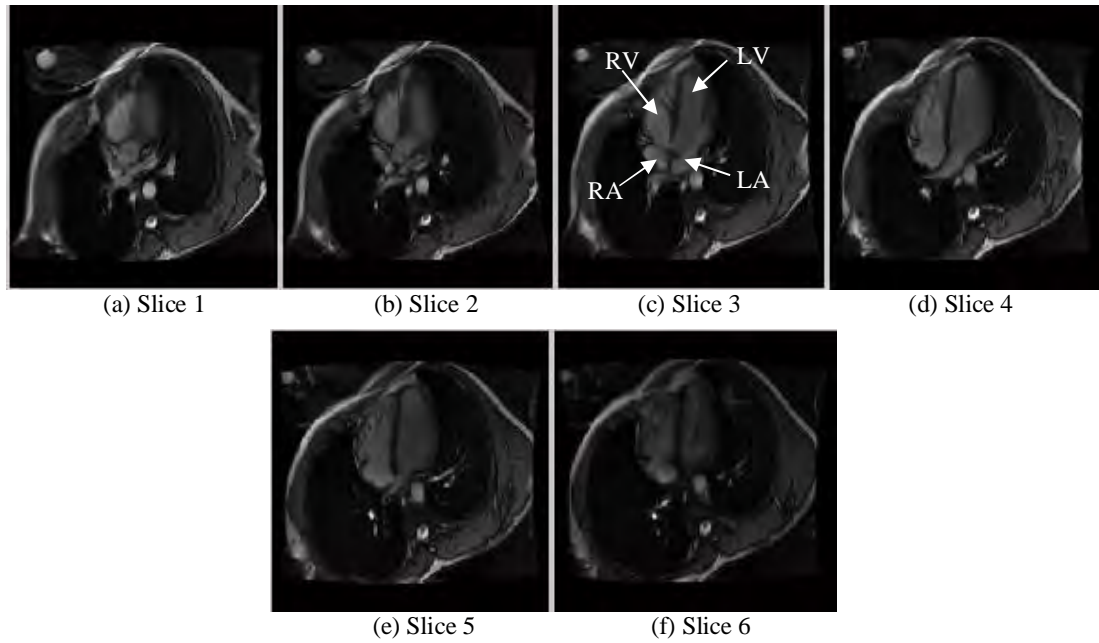


Figure 2-7: Examples of Cardiac MRI in Four Chamber View per slice. The left ventricle, left atrium, right ventricle and right atrium are visible.

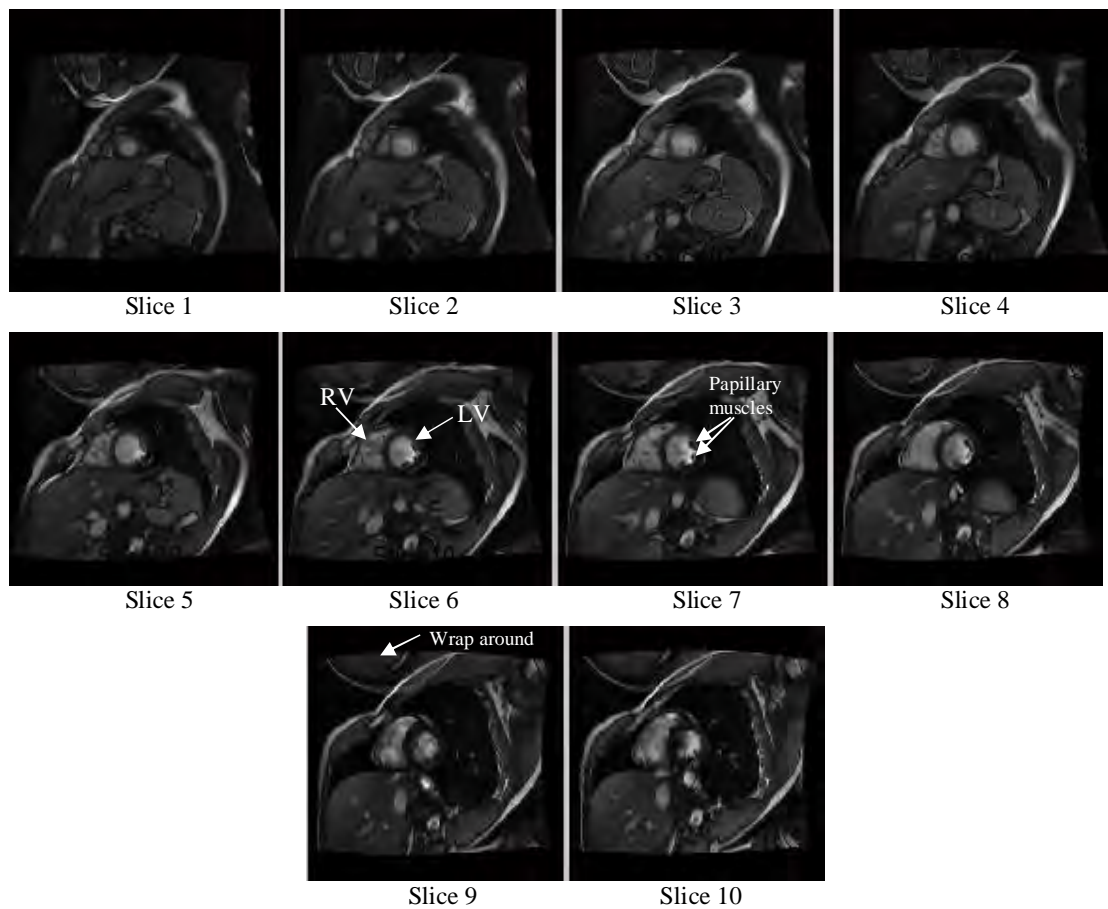


Figure 2-8: Examples of Cardiac MRI in Short Axis View per slice.

2.4 Functions of Left and Right Ventricles

With every heartbeat, the ventricles perform the function of continuously circulating blood throughout the body. As can be inferred from Wiggers diagram (Figure 2-2), during each cardiac cycle, the pressure as well as the volume of the ventricle changes. The volume of blood ejected during the cycle is known as the stroke volume (SV). Two main times in the cycle are the focus area to calculate the stroke volume. The first is the end diastolic volume (EDV) which is volume at the end of diastole phase (chamber relaxation or filling) and the second, the end systolic volume (ESV), which is the end of the systole phase (chamber contraction or ejection). The stroke volume is therefore calculated as the difference between the EDV and ESV as in (2.2). Another measure called the Ejection Fraction (EF) can be computed as shown in (2.3), which is the ratio of volume of blood pumped out a ventricle with each heartbeat.

$$SV = EDV - ESV \quad (2.2)$$

$$EF = \frac{SV}{EDV} \quad (2.3)$$

In a normal functioning heart, to maintain blood circulation, the stroke volume of the left ventricle must equal that of the right. It is shown that the right ventricle EDV is greater than the left; hence the EF of the left will be greater which implies that the left ventricle works harder than the right [1]. Thus the above mentioned measures are a key component in determining the global functioning of the left and right ventricles.

2.5 Effect of Cardiovascular Diseases on MRI

Imaging of the heart via MRI can be used to provide the following information in the cardiovascular system that could be created as a result of an ailment [21], [22], and [23]:

- a) Imbalance in blood circulation calculated by the amount of blood entering and leaving the ventricles.
- b) Reduced blood flow to a ventricle as a result from artery blockages.
- c) Damage of ventricles and tissues due to a heart attack.
- d) Damage of the ventricle valves.
- e) Abnormal growth from cancerous tumours.
- f) Increased or reduced thickness of myocardial, ventricle walls
- g) Aneurisms of the heart.

2.6 Summary

An introduction into the functioning of the human heart is presented in this chapter, describing the cardiac cycle and circulation of blood throughout the human body. Thereafter, the acquisition of images via magnetic resonance imaging, on different viewing planes, is explained and visualised. Finally, several metrics and ventricle volumes calculations are introduced which can be obtained from cardiac MRI. This is key in determining the presence of cardiovascular diseases.

CHAPTER 3 - CARDIOVASCULAR MRI SEGMENTATION

COMPARISON METRICS

Image segmentation refers to the process of detecting regions within an image and associating these regions with known objects. In other words, segmentation of the medical image distinguishes between different organs, tissues, vessels, blood flow, etc. A precise segmentation allows not only a better visualisation of the object but also makes it possible to quantify that particular area of interest and provide further meaningful information. For example from the MRIs of a human heart, if segmentation of the left and right ventricles exist, doctors will be interested in quantifying the thickness of the ventricle walls, the movement of each ventricle, blood volumes, blood flow-rates, etc. [1]. The segmentation of a ventricle from an MRI will produce a closed contour or delineation which encloses the said ventricle.

Section 3.1 provides the framework for the evaluation of ventricle segmentation algorithms. This section initially discusses visual assessment and thereafter looks at comparison to a ground truth. Methods of ground truth creation are also looked at. Three publically available datasets are presented which contain representation of the ground truth by expert manual segmentation. Thereafter mathematical and statistical measures are described in which the segmentation can be compared to the ground truth. Section 3.2 provides methods of volume calculation achieved from segmentation contours for the entire ventricle. This section also contains a proposed clinical assessment method when both the left and right segmentation contours are available. Section 3.3 and 3.4 provides assessment of the segmentation comparison methods stated in Section 3.1 and Section 3.2.

3.1 Evaluation and Comparison of Segmentation Methods

Segmentation methods can be evaluated based on three criteria namely accuracy, precision and efficiency of the recognition and delineation [68]. Accuracy is measured by the closeness to the ground truth, precision by the repeatability of the segmentation method and efficiency by the speed and ease of application of the method used. The main aim of cardiac MRI segmentation is to isolate the inner and outer surfaces of the left ventricle and right ventricle, so that several clinically relevant measurements can be calculated. Although there has been extensive research in the field of cardiac ventricle segmentation, there has been little research performed on the evaluation of such segmentation.

We assume that all MRIs are obtained for a patient P as a series of N two dimensional images P_i and is denoted as follows:

$$P = \{P_i\} \quad 1 \leq i \leq N. \quad (3.1)$$

Each patient image P_i consists of a set of $m \times n$ pixels referenced by location (x_k, y_l) and intensity $I_{i(x_k, y_l)} = P_i(x_k, y_l)$. If an object O_j in the image P_i has been segmented, the resultant delineation by M landmark points is represented as a set of pixel locations as in (3.2).

$$S_{P_i O_j} = \{(x_{1S, P_i O_j}, y_{1S, P_i O_j}), (x_{2S, P_i O_j}, y_{2S, P_i O_j}), \dots, (x_{MS, P_i O_j}, y_{MS, P_i O_j})\}. \quad (3.2)$$

The first method used to evaluate cardiac segmentation accuracy is by subjective evaluation, where an expert visually compares the image segmentation. A method is proposed in Section 3.1.1.1 in which a five point rating scale aims to provide experts with a larger range to accept or decline a segmentation performed on a ventricle. As research in this area progressed, supervised evaluation became more common, where the segmented image is compared against a manually segmented or a representation of ground truth segmentation. Section 3.1.1.6 and Section 3.1.1.7, presents a series of mathematical and statistical methods which are based on supervised evaluation.

3.1.1.1 Visual assessment of segmentation without ground truth

The accuracy of a segmentation algorithm is quantified through comparison against a ground truth which in most cases is manual delineation by an expert [70]. However, manual delineations involve tedious work and is time consuming. Initial assessment of segmentation accuracy was performed visually by experts and was termed subjective evaluation. The major downfall of this method is that the result is exposed to expert bias and variability, due to its subjectivity [73]. Each expert has their own standards to assess the accuracy of the segmentation.

To minimise the subjectivity, the first proposed method of segmentation evaluation is to allow a minimum of three experts E_a , where $3 \leq a \leq Q$, to visually assess the segmentation on a set of images chosen from P . In this method, the experts are provided with the images P_i and the set of associated $S_{P_i O_j}$ for the segmented region j . Each $S_{P_i O_j}$ is superimposed on the corresponding P_i and presented to the experts. Each of the three experts will either accept ($E_{aS_{P_i O_j}} = 1$) or reject ($E_{aS_{P_i O_j}} = 0$) the segmentation for region of interest j . The basic average accuracy calculation, A_{O_j} , as shown in (3.3), can be performed for the region of interest j on a set of K images, where $K \leq N$ and is given by:

$$A_{O_j} = \left(\frac{\sum_{a=1}^Q \sum_{i=1}^K E_{aS_{RO_j}}}{Q \times K} \right) \div \div \times 100\% . \quad (3.3)$$

For further precision, a 5 point rating scale (Likert scale [74]) can be used by each expert where a scoring of each $E_{aS_{RO_j}}$ will be as indicated in Table 3-1. Hence the accuracy calculation from (3.3) will now be represented as:

$$A_{O_j} = \left(\frac{\sum_{a=1}^Q \sum_{i=1}^K E_{aS_{RO_j}}}{Q \times K \times 5} \right) \div \div \times 100\% . \quad (3.4)$$

The method described in (3.4) can also be influenced by bias, depending on the sequence with which the data is presented. To minimise such bias, it is recommended that a large enough datasets (K) and a large number of experts (Q) be used. From the above description it can be seen that this process could become very time consuming, hence this accuracy method evaluation cannot be used for real time systems and diagnosis.

Table 3-1: Five point rating scale for expert visual assessment

Score	Description
1	Poor Segmentation (Does not cover entire ROI)
2	Fair Segmentation (50% to 80% of points lie on boundary of ROI)
3	Good Segmentation (80 to 90 % of points lie on boundary of ROI)
4	Very Good Segmentation (90 to 99% of points lie on boundary of ROI)
5	Excellent Segmentation (All points lie on boundary of ROI)

* ROI = Region of Interest

3.1.1.2 Statistical assessment of segmentation without ground truth

Unsupervised segmentation evaluation approaches do not require a reference image or ground truth, but instead evaluates a segmentation based on how well it matches a broad set of characteristics of a set of segmented images as desired by experts [70]. This ability not to use a ground truth for evaluation purposes allows the segmentation algorithm to function over a wide range of conditions and work with many different types of images.

The Simultaneous Truth and Performance Level Estimation (STAPLE) algorithm [78] employs a probability map to create a best fit from a number of segmentations, a , for an object j . From the segmentations, computation of a probabilistic estimate of the hidden, implicit, true segmentation is computed and a measure of the performance level achieved for each segmentation is calculated. The probabilistic estimate of the true segmentation is formed by

estimating an optimal combination of the segmentations, weighting each segmentation depending upon the estimated performance level, together with a prior model that can account for the spatial distribution of structures and spatial homogeneity constraints.

STAPLE exploits expectation maximisation to calculate segmentation reliability by estimating the performance parameters and a probabilistic estimate of the true segmentation, by iterated estimation [78]. This reliability measure can be represented as $\theta_{aS_{R_{O_j}}G_{R_{O_j}}}^f$ and defined as the probability that a segmentation a , at iteration f , reports that a point $v = (x_k, y_l)$ has a particular segmentation $S_{R_{O_j}}$ given a true segmentation $G_{R_{O_j}}$. The first step of each iteration is estimation of the conditional probability of the true segmentation given the segmentation decisions and previous observed data D_{vfr} with repetition r . The conditional probability that the point v belongs to a class $W_{S_{R_{O_j}}v}^f$ at iteration f is represented as below [78]:

$$W_{S_{R_{O_j}}v}^f = p(G_{R_{O_j}} = S_{R_{O_j}} | D_v, \theta^f) . \quad (3.5)$$

The second step is to update the estimation of the performance parameters $\theta_{aS_{R_{O_j}}G_{R_{O_j}}}^{f+1}$.

3.1.1.3 Establishment of representation of ground truth by experts

The easiest method to obtain a representation of the ground truth is to have an expert manually delineate the object of interest j . However, manual delineations involves tedious work and is time consuming. Furthermore, this method is exposed to expert bias and variability, due to its subjectivity. Each expert has their own standards to assess the accuracy of the segmentation. Thus it is proposed that more than one expert must be used and the representation of the ground truth can be derived from the set of these delineations. The other factor to consider in manual segmentation by experts is precision, which is quantified by the reproducibility of segmentation results obtained from using the same image. Hence it is also proposed that the expert manually segment the same image more than once.

The proposed methods of ground truth estimation calculation must allow a minimum of three experts E_a , where $3 \leq a \leq Q$, to manually segment the object of interest j on a set of images chosen from P . The experts are provided with the images P_i and will create at least two segmented sets $G_{aP_{O_j}e}$, where $2 \leq e \leq E_{\max}$, for each P_i .

The first method in obtaining the ground truth is to use a voting based system [73] where each pixel from the segmented sets $G_{aP_{O_j}e}$ will be classified using a threshold t as follows:

$$t_{P_i} = \frac{(Q \times E_{\max}) + 1}{2}. \quad (3.6)$$

The threshold defines the number of experts that have voted for this pixel to be a part of the ground truth. Thus each pixel in the ground truth, for all $3 \leq a \leq Q$ and $2 \leq e \leq E_{\max}$, is given by:

$$G_{aP_i}e(x) \in G_{P_i} \Leftrightarrow \left(\sum_{q=1}^Q \sum_{f=1}^{E_{\max}} (G_{aP_i}e(x) \in G_{qP_i}f) \right) \geq t_{P_i} \quad (3.7)$$

The second method in obtaining the ground truth is to use a probability based method such STAPLE (Section 3.1.1.2) that creates a best fit from a number of segmentations for an object j . In this method, each $G_{aP_i}e$ is fed into the STAPLE algorithm to obtain G_{P_i} .

3.1.1.4 Establishment of ground truth by use of Cardiac Phantoms

Phantoms of the heart have been built and developed, both physically and digitally. The advantage in using these phantoms is that the exact anatomy of the phantom is known, thus providing a ground truth that can be used to evaluate different segmentation techniques. Physical human heart phantoms are normally constructed from some type of a material, such as Polyvinyl Alcohol hydrogel, that mimics elasticity of human soft tissue and is composed of anatomically correct left and right ventricle structures [77]. Furthermore, the phantom is able to be precisely controlled via software such that motion and independent control of compression, stretching and torsion motion of tissue deformation can be defined. The flexible motion control software allows users to easily program and execute sophisticated cardiac motion events [77]. The physical phantom is thus MRI compatible and imaging through multiple slices is possible throughout the controlled cardiac cycle.

The use of physical phantoms is limited in that there is a high cost associated to create a realistic range of patient sizes, variations, and deformations [78]. Thus the introduction of computer generated digital phantoms offers a more practical solution. Digital phantoms create a virtual model of the human anatomy and imaging of these phantoms is also performed digitally using an accurate computerised model of the physics of the imaging process. With simulation, it is therefore possible to perform clinically relevant experiments entirely on the computer.

Although much work and research has been done in the creation and optimisation of physical and digital phantoms, these phantoms do not fully reflect clinically produced images as it is difficult to construct a phantom that displays a full range of characteristics, such as noise and partial volume effects. Furthermore, the image resolution is substandard in comparison to clinical MRIs.

3.1.1.5 Establishment of ground truth using publically available human sample datasets

Supervised evaluation methods require comparison of the segmented image to a ground truth or gold standard [70]. This explicitly requires a sample dataset which must be easily available to all authors. For medical images, due to ethical considerations, a large dataset is difficult to be made public. In order to use any MRI dataset, for comparison or evaluation purposes, approval must be sought from the respective medical or ethical boards. There are a handful of datasets made publically available on the internet that have obtained relevant approval to be published. The other problem with a publically available dataset is whether the ground truth is correct, as these are created by manual segmentation by experts and are subjective. Each expert has their own set of rules for what to include in the segmentation of the ventricles [71], [72]. The sections below will describe the three most commonly used publically available datasets. For the sections that follow, the expert delineations presented in these publically available dataset will be taken as a representation of the ground truth.

3.1.1.5.1 Sunnybrook Cardiac Data

The Sunnybrook Cardiac Data (SCD), also known as the 2009 Cardiac MR Left Ventricle Segmentation Challenge data [71], consists of 45 MRI datasets from a mixed range of patients having different pathologies, of which 32 are male and 13 are female. Breaking the datasets down further, 9 are from healthy patients, 12 from patients having heart failure with infarction, 12 from patients having heart failure without infarction and 12 from patients having hypertrophy.

For each dataset, DICOM images are presented in the SAV with each image being of size 256x256 pixels. MRI slices are presented from the apex slice to the base slice for the left and right ventricle. Contained with the DICOM images is a set of manually delineated contours of the left ventricle only. Furthermore, these contours are only available for the endocardium (inner contour) and epicardium segmentation (outer contour) at the end diastole cardiac phase and for the endocardium at the end systole cardiac phase. An extract with segmentation of a patient with a normal functioning heart at end diastole cardiac phase and end systole is shown in Figure 3-1 and Figure 3-2, whereas the segmentation of patient having heart failure with infarction at end systole cardiac phase in shown in Figure 3-3.

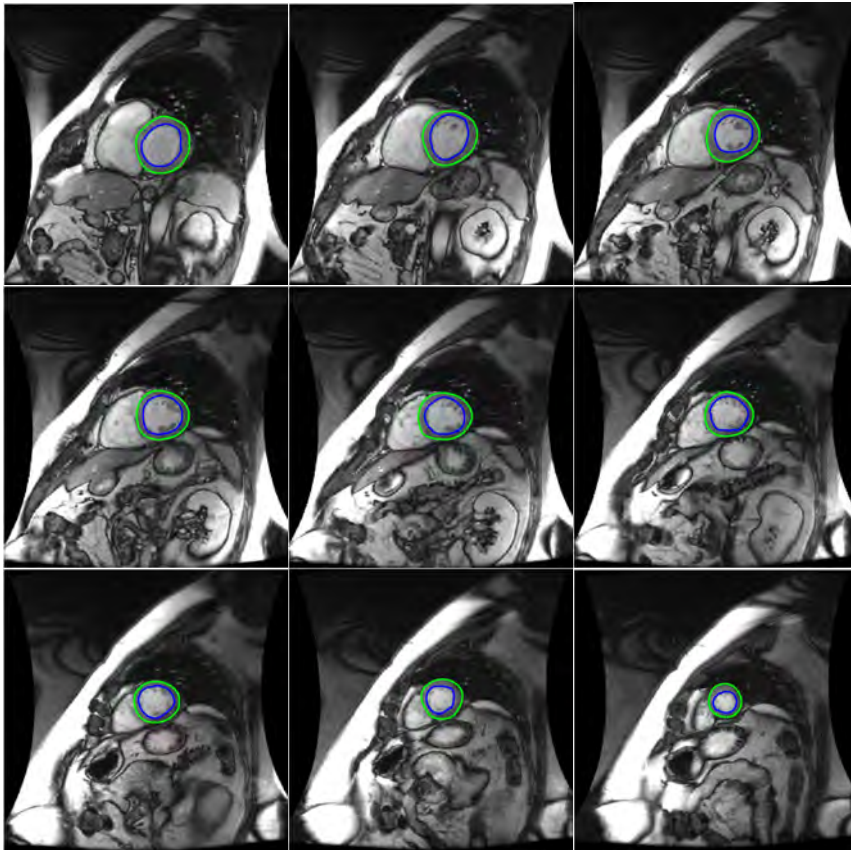


Figure 3-1: SAV MRI from SCD at the end diastolic cardiac phase for a patient with no cardiac abnormalities with segmentation performed on left ventricle endocardium (blue contours) and epicardium (green contours) from the base slice (upper left image) to apex slice (lower right image)

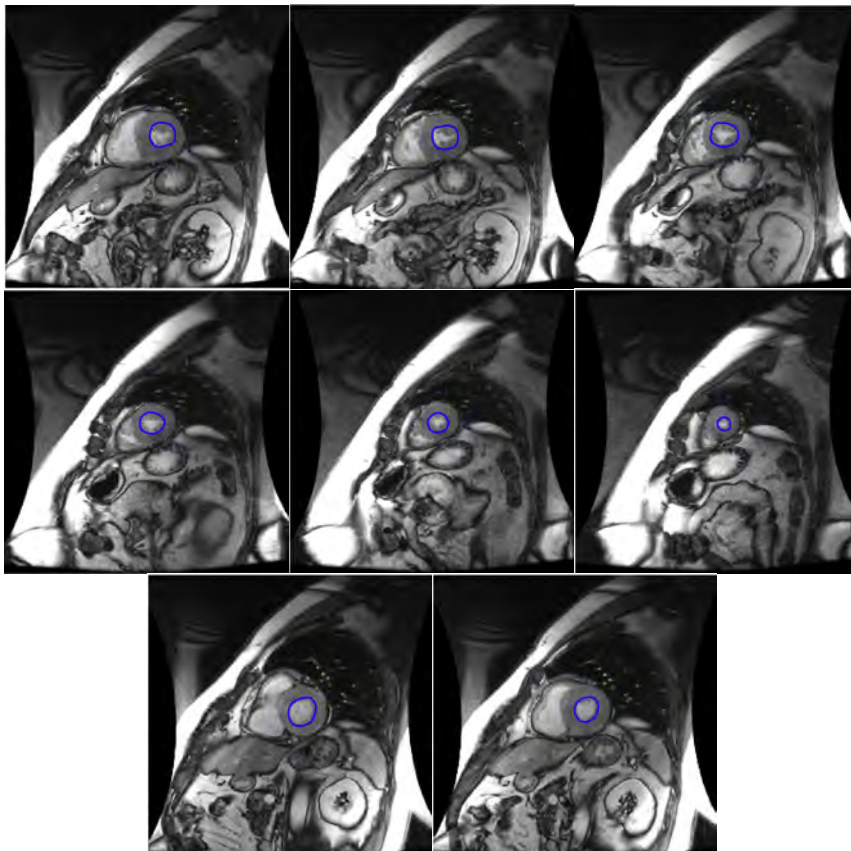


Figure 3-2: : SAV MRI from SCD at the end systolic cardiac phase for a patient with no cardiac abnormalities with segmentation performed on left ventricle endocardium (blue contours)

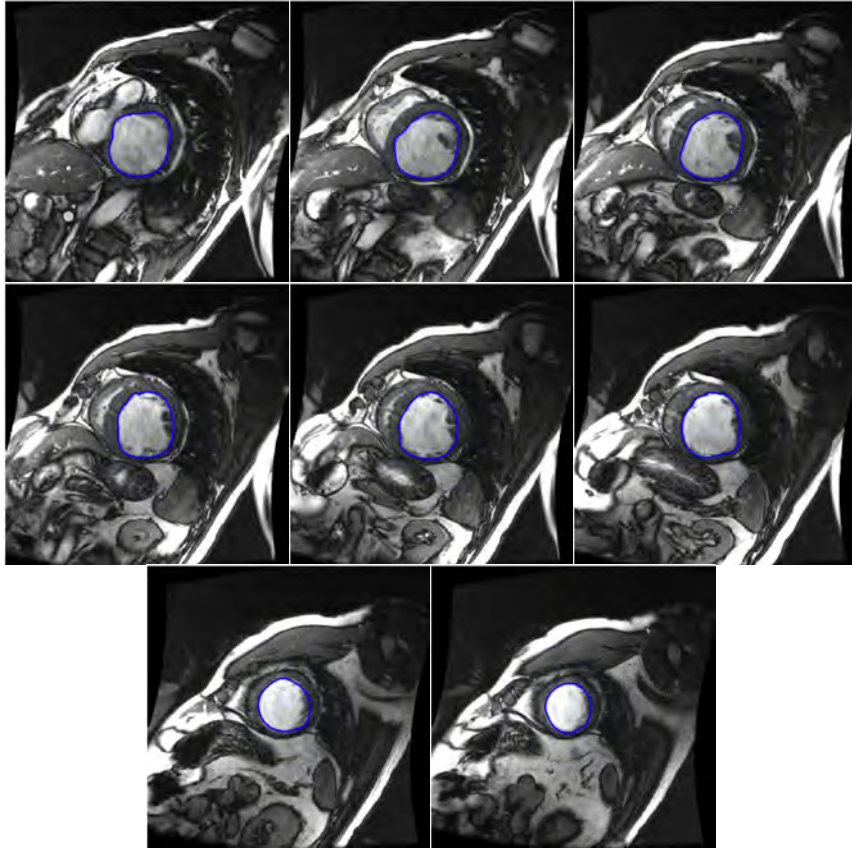


Figure 3-3: SAV MRI from SCD at the end diastolic cardiac phase for a patient with heart failure with segmentation performed on left ventricle endocardium (blue contours) from the base slice (upper left image) to apex slice (lower right image)

A set of rules for expert manual delineation was defined [71] and applied twice to each patient MRI dataset so that the first pass would be the draft and the second the acceptance. The initial procedure was to locate the end diastole and end systole images for all slices by manually browsing through the captured MRI. Thereafter the base and the apex slices were found, where the apex slice is taken to be the lowest slice that includes a blood pool in both the end diastole and end systole images. The contour drawing process then commenced where it was specified that the both the endocardium and epicardium contours for the end diastole phase to be created and was only necessary to draw endocardium contours for end systole phase. In general all contours drawn needed to be in a smooth curve. One assumption made during the above contouring process was to include trabeculae and papillary muscles in the segmentation area.

3.1.1.5.2 Right Ventricle Segmentation Challenge Data

The Right Ventricle Segmentation Challenge Data (RVSCD), provides a series of MRI data for the right ventricle for 48 patients [72] acquired at Rouen University Hospital in 2008. These patients were diagnosed with pathologies of myocarditis, ischaemic cardiomyopathy, arrhythmogenic right ventricular dysplasia, dilated cardiomyopathy, hypertrophic cardiomyopathy, aortic stenosis [72]. The average age of the patients was 52 years with a deviation of ± 18 years, with 36 being male.

The MRIs are presented in DICOM format in the SAV only for each patient. The images have been cropped and zoomed to a resolution of 256x216 pixels, with the ventricles appearing central to the image. For each patient dataset, the number of images were filtered by the relevant expert, such that only the slices from base to the apex of the ventricle were presented. Furthermore images from the end diastole and end systole cardiac phases were identified and numbered accordingly.

The set of rules defined for the expert manual delineation following the same as that used in the SCD (Section 3.1.1.5.1). Initially the base and apex slices were identified and all end diastole and end systole images for slices inclusive and in between were extracted. For these extracted images, contours were drawn to segment the right ventricle endocardium and epicardium areas. Once again, trabeculae and papillary muscles were included in the segmentation area. Figure 3-4 illustrates an extract from this dataset for a patient with no cardiac abnormalities.

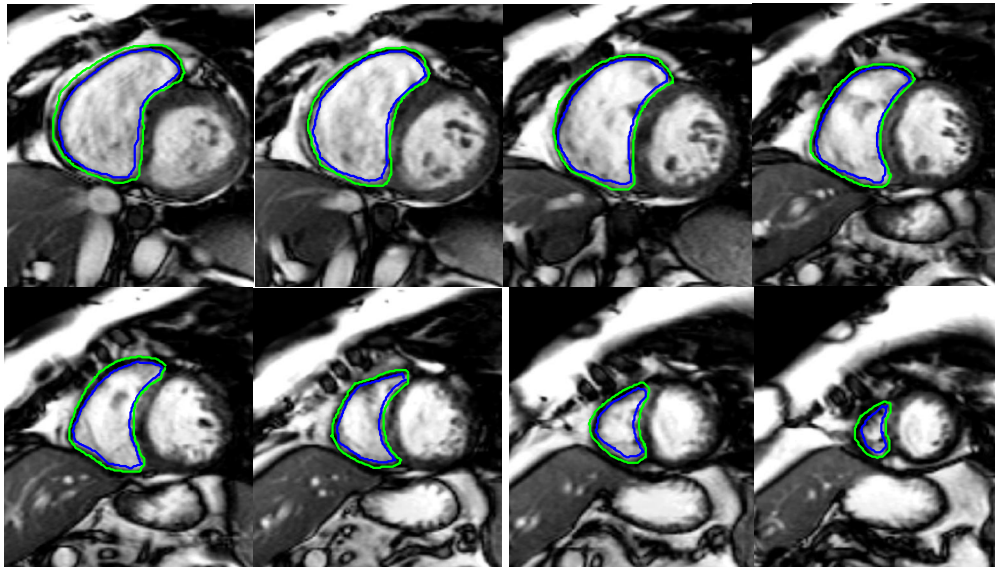


Figure 3-4: SAV MRI from RVSCD at the end diastolic cardiac phase for a patient with no cardiac abnormalities with segmentation performed on right ventricle endocardium (blue contours) from the base slice (upper left image) to apex slice (lower right image)

3.1.1.5.3 York University Dataset

The York University Dataset (YUD) consists of 33 patients under the age of 18 acquired from the Department of Diagnostic Imaging of the Hospital for Sick Children in Toronto. These patients were diagnosed with pathologies such as cardiomyopathy, aortic regurgitation, enlarged ventricles and ischemia [9].

The patient datasets were presented in a raw data image data matrix stored in a Matlab created file. For the 33 patients a total of 7980 images were presented in the stored image matrix. Each

image is of size 256x256. Manual delineation by the expert aimed to create segmentation contours of the left ventricle endocardial and epicardial where visibly possible [9]. This resulted in a total of 5011 segmented images. For this dataset, trabeculae and papillary muscles were also included in the segmentation area. A sample of one of the patient data over single slice for the entire cardiac cycle is shown in Figure 3-5. Unfortunately, the set of rules defined for the expert manual delineation was not publically available.

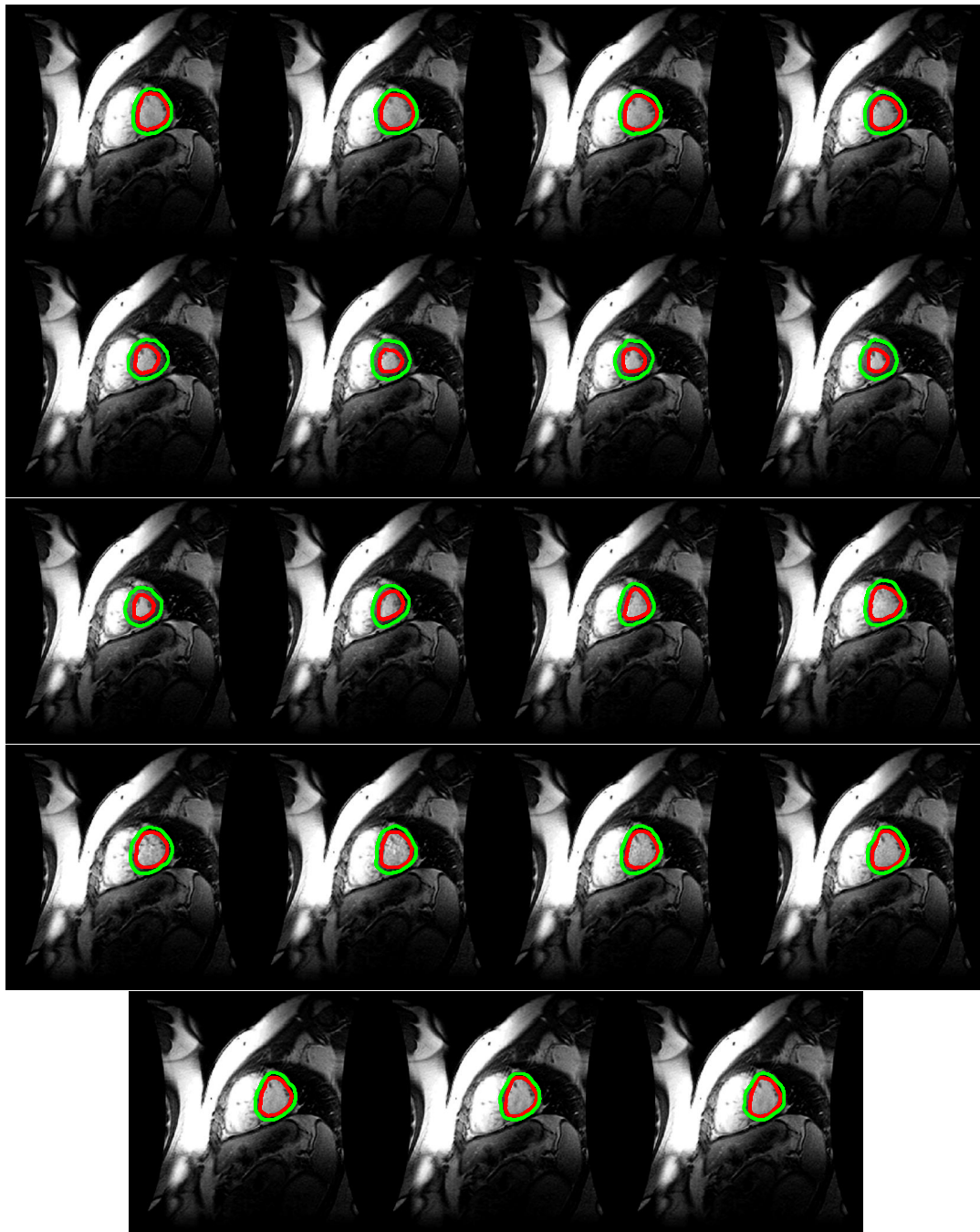


Figure 3-5: SAV MRI from YUD at for entire cardiac cycle for a patient with cardiac abnormality with segmentation performed on left ventricle endocardium (red contours) and epicardium (red contours)

3.1.1.6 Mathematical assessment of segmentation with Ground Truth

For ventricle segmentation, it is almost impossible to get the absolute true segmentation [2]. Thus a representation of the ground truth is required. Section 3.1.1.3 and Section 3.1.1.4 depicts methods that can be used to obtain a representation of the ground truth. In this section, we shall assume that the ground truth segmentation for each region of interest is present and shall be represented as:

$$G_{P_i} = \{(x_{1G,P_i}, y_{1G,P_i}), (x_{2G,P_i}, y_{2G,P_i}), \dots, (x_{MG,P_i}, y_{MG,P_i})\}. \quad (3.8)$$

Several basic metrics based on distance measures are defined below that can be used to compare the segmentation to the ground truth for object j on image P_i . In essence they all follow the principle; the smaller the measured outcome, the better the segmentation accuracy. Equations (3.2) and (3.8) can be re-represented as depicted in (3.9) and (3.10), with the points aligned.

$$S_{P_i} = \{x_{1S,P_i}, x_{2S,P_i}, \dots, x_{MS,P_i}, y_{1S,P_i}, y_{2S,P_i}, \dots, y_{MS,P_i}\}^T. \quad (3.9)$$

$$G_{P_i} = \{x_{1G,P_i}, x_{2G,P_i}, \dots, x_{MG,P_i}, y_{1G,P_i}, y_{2G,P_i}, \dots, y_{MG,P_i}\}^T. \quad (3.10)$$

The simplest method of distance measure is the Mean (3.11), which calculates the average distance between the segmentation points and the ground truth in terms of pixels. Following from this, the Mean Square Error (3.12) can be derived which in essence is the average of the square of the errors. If each point represents a dimension, then the vectors S_{P_i} and G_{P_i} are vectors in $2M$ dimensional space. Hence the Euclidean Distance 1 ($2M$ dimensions), can be defined as in (3.13). Realistically though, the pixel distance measure is in the two dimensional space. Thus (3.13) can be reduced to a two dimensional Euclidean Distance measure as shown in (3.14).

$$Mean_{P_i} = \frac{1}{2M} \sum_{b=1}^{2M} |S_{P_i}(b) - G_{P_i}(b)|. \quad (3.11)$$

$$MSE_{P_i} = \frac{1}{2M} \sum_{b=1}^{2M} (S_{P_i}(b) - G_{P_i}(b))^2. \quad (3.12)$$

$$ED1_{P_i} = \sqrt{\sum_{b=1}^{2M} (S_{P_i}(b) - G_{P_i}(b))^2}. \quad (3.13)$$

$$ED2_{P_i} = \frac{1}{M} \sum_{b=1}^M \sqrt{(S_{P_i}(b) - G_{P_i}(b))^2 + (S_{P_i}(b+M) - G_{P_i}(b+M))^2}. \quad (3.14)$$

The Hausdorff distance (Haus) measure (3.15) and (3.16) is an indication of the extent to which each point in the segmented set S_{P_i} lies near some point in the ground truth set G_{P_i} . The

directed Hausdorff distance function, $h(C, D)$, identifies the point, $c_{\max} \in C$, that is furthest away from all points $d \in D$, and returns the distance measure from point c_{\max} to its nearest neighbour in D [75]. In essence, each point of C must be within a distance of $h(C, D)$ of some point of D . The distance measure $dist(c, d)$ can be calculated using a formula similar to that used in (3.14). Hence the Hausdorff distance calculation aims to measure the degree of mismatch between two sets by measuring the distance of a point in C that is furthest away from a point in D and vice versa. Figure 3-6 illustrates this graphically where the segmentation contour of the left ventricle is visualised in red and the ground truth contour in blue. The Hausdorff distance is the maximum distance from a red point in set $S_{P_{O_j}}$ to a blue point in set $G_{P_{O_j}}$, calculated by:

$$Haus_{P_{O_j}} = \max(h(S_{P_{O_j}}, G_{P_{O_j}}), h(G_{P_{O_j}}, S_{P_{O_j}})), \quad (3.15)$$

where;

$$h(C, D) = \max_{c \in C} \min_{d \in D} dist(c, d). \quad (3.16)$$

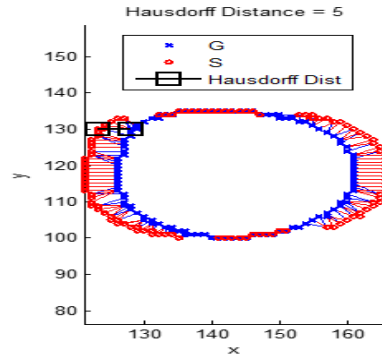


Figure 3-6: Hausdorff distance calculation on left ventricle which calculates the furthest distance that the red segmentation contour is from the ground truth blue contour.

3.1.1.7 Statistical Assessment with Ground Truth

The majority of statistical segmentation accuracy measures are region based and focuses on the region overlap, for object j on image P_i , between the segmented region $RS_{P_{O_j}}$ and representation of the ground truth region $RG_{P_{O_j}}$. The output is normalised from 0 to 1, where 0 represents no overlap and 1 perfect alignment. The degree of overlap can be quantified by three measures namely True Positive (TP), False Negative (FN) and False Positive (FP), as depicted in Figure 3-7.

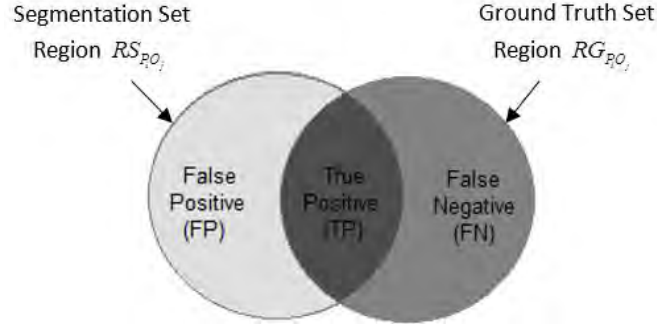


Figure 3-7: Overlap measures to define region based segmentation accuracy

There are several statistical measures based on similarity that can now be defined. The Jaccard Index (3.17) is the size of the intersection divided by the size of the union [76]. The Dice Coefficient (3.18) is similar to the Jaccard and measures two times the area of the intersection between two segmentation and ground truth divided by the sum of the area of the two [76]. The Sensitivity measure [76] is the fraction of positives that are correctly detected and is defined in (3.19).

$$Jac_{PO_j} = \frac{SR_{PO_j} \cap GR_{PO_j}}{SR_{PO_j} \cup GR_{PO_j}} = \frac{TP}{FP + TP + FN} \quad (3.17)$$

$$Dice_{PO_j} = \frac{2(SR_{PO_j} \cap GR_{PO_j})}{(SR_{PO_j} \cap GR_{PO_j}) + (SR_{PO_j} \cup GR_{PO_j})} = \frac{2TP}{TP + FP + TP + FN} \quad (3.18)$$

$$Sens_{PO_j} = \frac{(SR_{PO_j} \cap GR_{PO_j})}{GR_{PO_j}} = \frac{TP}{TP + FN} \quad (3.19)$$

Several other statistical measures can be used to measure segmentation accuracy such as Specificity, Cohen Kappa, Rand Index, Interclass Correlation, Volumetric Similarity Coefficient and Mutual Information [77], but these will not be discussed here.

3.2 Calculation of ventricular volumes from segmentation

The mathematical and statistical methods in Section 3.1.1.6 and Section 3.1.1.7 requires the presence of a ground truth segmentation for that particular MRI dataset. However the publically available cardiac MRI datasets for ventricle segmentation only has ground truth representations in the SAV. Thus if evaluation of ventricle segmentations in other cardiac MRI views is required, then the methods of Section 3.1.1.1 and 3.1.1.2 need to be used, which could be subjective. This section introduces a clinical criterion that is based on unsupervised evaluation which allows an objective accuracy measure of the segmentation algorithm.

3.2.1.1 Clinical Assessment without Ground Truth

One of the main aims of obtaining accurate segmentation of the left and right ventricles of the heart is that certain clinical factors can be computed. The stroke volume (SV) is the volume of blood that is ejected from a ventricle [7]. This volumetric measure can be computed by subtracting the ventricular volume at the end of contraction (systole) from the ventricular volume at the end of relaxation (diastole). This can be represented as shown below, where ESV is the end systole volume and EDV is the end diastole volume:

$$SV = EDV - ESV . \quad (3.20)$$

Another measure called the ejection fraction (EF) can be computed, which is volume of blood pumped out from a ventricle with each heartbeat, and is given by:

$$EF = \frac{SV}{EDV} . \quad (3.21)$$

To maintain equilibrium in a normal functioning heart, the stroke volumes of the left and right ventricles must be the same [1]. Thus this can be used as a measure of accuracy if both the ventricles are segmented. The percentage error in stroke volumes between the left ventricle (SV_{LV}) and right ventricle (SV_{RV}) is defined as:

$$SV_{error} = \left(\frac{SV_{LV} - SV_{RV}}{SV_{LV}} \right) \times 100\% \quad (3.22)$$

The most commonly used method of calculating ventricular volumes is Simpsons rule for measuring volumes [56]. In this method, the volume at a particular cardiac time (either end diastole or end systole) is obtained by multiplying the segmented area by the slice thickness per slice. The volume of the ventricle is achieved by adding each slice volume for all slices that segment that ventricle. This method is visually represented in Figure 3-8 and Figure 3-9, where the distance between the slices (slice thickness) is clearly shown.

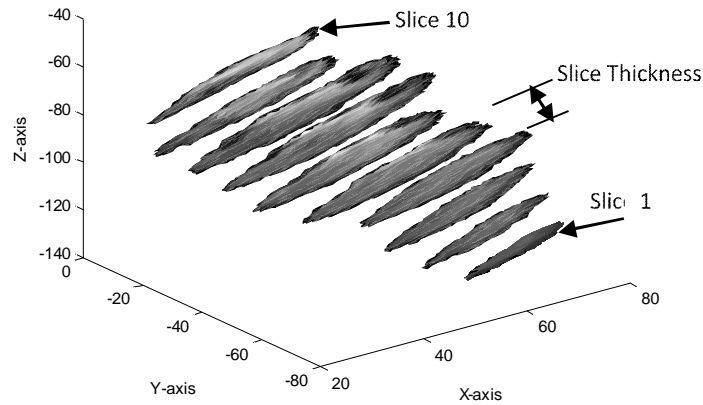


Figure 3-8: Segmented portions of the left ventricle in the short axis MRI view for a patient with slice thickness of 9mm.

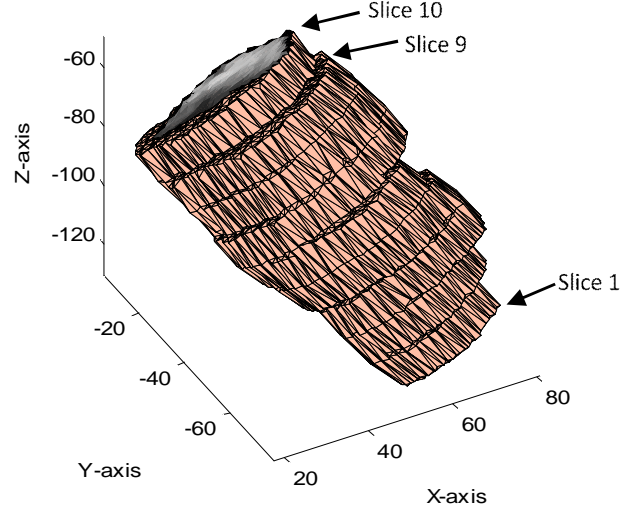


Figure 3-9: Segmented portions of the left ventricle encased in a surface plot using Simpsons rule in the short axis MRI view for a patient with slice thickness of 9mm.

To derive the volume in this figure using Simpsons rule, the area of slice one is multiplied by the slice thickness and added to area of slice two multiplied by the slice thickness, until the 10th slice is reached. From Figure 3-9, the volume for the left ventricle in the short axis MRI view is represented as [56]:

$$V_{SA,LV} = \sum_{i=1}^{10} Area(S_{P_{iO_{LV}}}) \times ST_i, \quad (3.23)$$

where $S_{P_{iO_{LV}}}$ is the segmentation of the left ventricle for MRI i in the short axis view and ST_i is the slice thickness, which is normally a constant for a particular acquisition.

It can also be seen from Figure 3-9 that the Δ step area Δ volume approximation per slice leads to significant errors in the volumetric calculation if the slice thickness is not the same as the voxel dimensions. Furthermore, there is some debate as to the inclusion of the slice thickness at the end slices (above slice 10 and below slice 1) in the volume calculation. Figure 3-9 does not include either.

Although Simpsons rule is the accepted standard for ventricular volumetric calculation from cardiac MRIs [56], several authors have provided methods aimed to be more accurate. The biplane Simpson's disk method assumes that the left ventricle in the short axis view represents a disc [55]. The volume is obtained by the summation of the stack of discs along the left ventricle long axis. The biplane area length method [56] used to calculate atrium volumes, combines a percentage of the four chamber view area and the two chamber view area. Several geometric calculations have also been proposed, which do not require full segmentation of the ventricles. These include hemisphere cylinder model, the single and biplane ellipsoid model and Teichholz

model [56], [59], [61]. The area or volume of the ellipsoid is based on the longitudinal, transverse and anto-posterior diameters which are perpendicular to each other. The last method used is semi-automatic, where the user manually identifies the boundaries in a three dimensional view [56] and a thresholding technique is used.

3.3 Effectiveness of distance and statistical based measures

In order to compute the effectiveness that the distance and statistical measure have in assessing ventricle segmentation contours to the ground truth contour, a series of tests is performed on the ground truth contour. The cardiac MRI dataset used for the first test is a subset from the RVSCD (Section 3.1.1.5.2). For a particular patient from the dataset, the ground truth representation consists of a contour with 273 points which segments the right ventricle. This is visually represented in Figure 3-10 (a) and is denoted by RV1.

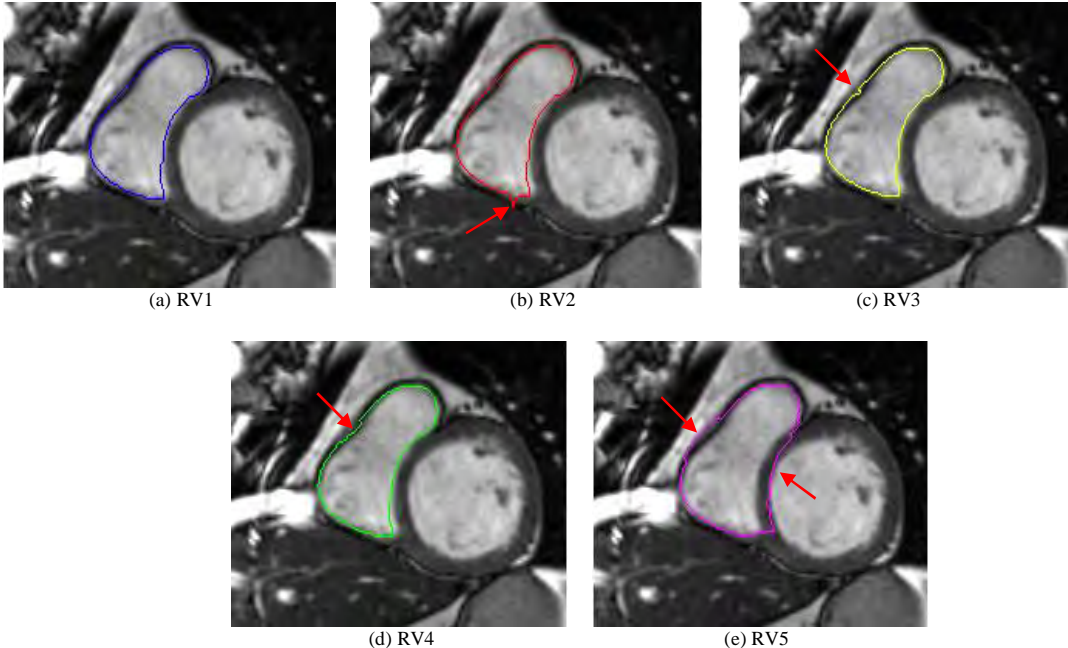


Figure 3-10: Segmentation of Right Ventricle using 273 contour points. The red arrow indicates the contour points that has moved from the ground truth representation in (a)

The series of tests performed is as follows:

- i. Move two points of the contour RV1 away from the right ventricle to create RV2 (Figure 3-10 (b)). This will create a gap in the overlap.
- ii. Move two points of the contour RV1 towards the right ventricle to create RV3 (Figure 3-10 (c)). Theoretically, the overlap result should not be effected.

- iii. Move points of the contour of RV1 to align the contour closer to the endocardium border of the right ventricle to create RV4 (Figure 3-10 (d)). This improves the ventricle segmentation but does not create a smooth contour.
- iv. Move points of the contour of RV1 to align the contour closer to the endocardium border of the left ventricle and the epicardium border of the right ventricle to create RV5 (Figure 3-10 (e)). This is a common occurrence if shape models are used to perform automatic segmentation
- v. Repeat the tests from i to iv above for a contour length of 148 points to determine the effect of using less contour points in the ventricle segmentation.

The distance and statistical based accuracy measures from equations (3.11), (3.12), (3.13), (3.14), (3.15), (3.17), (3.18) and were applied to the series of tests discussed above. For the accuracy calculation of (3.4), three expert observers were used and the parameters chosen are $K = 1$ and $Q = 3$. The segmentation accuracy for all images is tested against the segmentation of RV1 and the results as displayed in Table 3-2.

Table 3-2: Segmentation accuracy calculation on right ventricle segmentation using various mathematical and statistical methods with the availability of the ground truth (273 contour points)

Test Number	A_{O_j} (%)	$Mean_{RO_j}$	MSE_{RO_j}	$ED2_{RO_j}$	$Haus_{RO_j}$	$Dice_{RO_j}$	Jac_{RO_j}	$Sens_{RO_j}$
RV1	86.6	0	0	0	0	1	1	1
RV2	86.6	0.0110	0.0330	0.0220	2.8284	0.9993	0.9986	1
RV3	93.3	0.0110	0.0330	0.0220	2.2361	0.9993	0.9986	0.9986
RV4	100	0.0678	0.2253	0.1355	2.8284	0.9951	0.9903	0.9903
RV5	40	1.5696	14.5476	3.1392	12	0.9141	0.8418	1

A=Visual Expert Accuracy (3.4)

ED2=Euclidean Distance 2 (3.14)

Jac = Jaccard Index (3.17)

Mean=Mean error (3.11)

Haus = Hausdorff Distance (3.15)

Sens = Sensitivity (3.19)

MSE=Mean Square Error (3.12)

Dice = Dice Coefficient (3.18)

Table 3-3 provides segmentation accuracy calculations on a set of images similar to that of Table 3-2 with the difference being that the number of contour points to perform the segmentation has been reduced to 148. This is normally the case for different automatic and semi-automatic segmentation algorithms that have varying contour lengths.

Table 3-3: Segmentation accuracy calculation on right ventricle segmentation using various mathematical and statistical methods with the availability of the ground truth (148 contour points)

Test Number	A_{O_j} (%)	$Mean_{RO_j}$	MSE_{RO_j}	$ED2_{RO_j}$	$Haus_{RO_j}$	$Dice_{RO_j}$	Jac_{RO_j}	$Sens_{RO_j}$
RV1	86.6	0	0	0	0	1	1	1
RV2	86.6	0.0203	0.0608	0.0405	2.8284	0.9990	0.9980	1
RV3	93.3	0.0203	0.0608	0.0405	2.2361	0.9986	0.9972	0.9972
RV4	100	0.0980	0.3682	0.1959	3.1623	0.9947	0.9895	0.9895
RV5	40	1.4865	13.7297	2.9730	12	0.9120	0.8383	1

Figure 3-11 depicts the five images of left ventricle segmentation acquired from the SCD (Section 3.1.1.5.1) and have the contours obtained in the test method similar to Figure 3-10. LV1 contour is a representation of the ground truth (expert manual delineation). LV2 and LV3 have two points that have been moved away from LV1. LV4 aims to improve segmentation accuracy by not including one papillary muscle. LV5 converges on the endocardial border of the right ventricle. Table 3-4 provides detail on the resultant comparative measures to the ground truth representation.

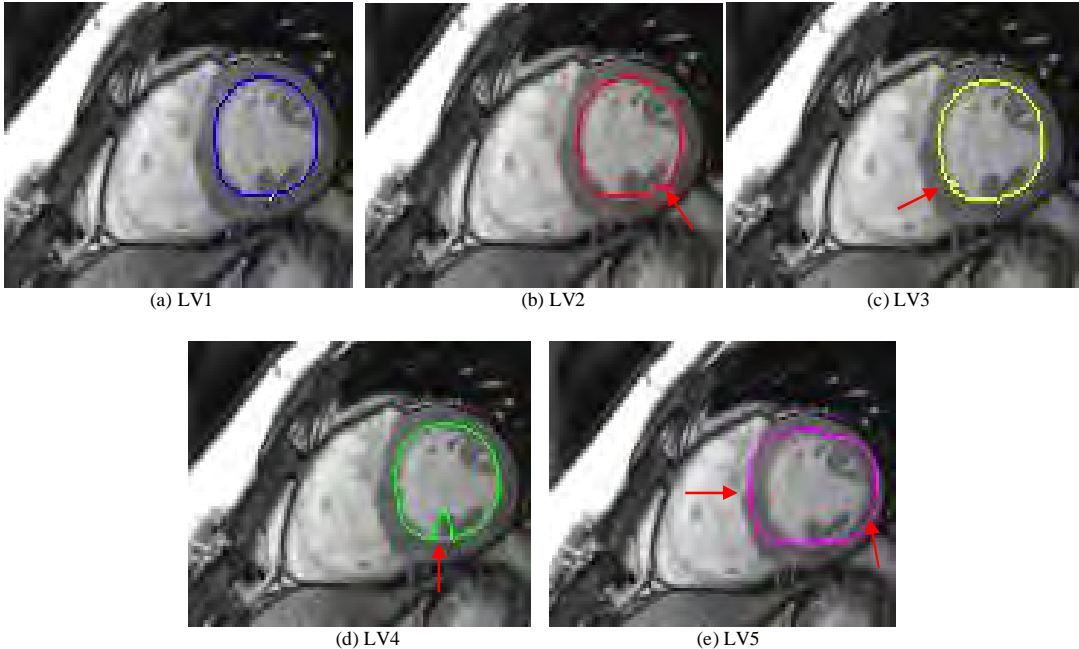


Figure 3-11: Segmentation of Left Ventricle using 112 contour points. The red arrow indicates the contour points that has moved from the ground truth representation in (a).

Table 3-4: Segmentation accuracy calculation on left ventricle segmentation using various mathematical and statistical methods with the availability of the ground truth (112 contour points)

Test Number	A_{O_j} (%)	$Mean_{P_{O_j}}$	$MSE_{P_{O_j}}$	$ED2_{P_{O_j}}$	$Haus_{P_{O_j}}$	$Dice_{P_{O_j}}$	$Jac_{P_{O_j}}$	$Sens_{P_{O_j}}$
LV1	93.3	0	0	0	0	1	1	1
LV2	86.6	0.0268	0.0804	0.0536	2.2361	0.9975	0.9950	1
LV3	86.6	0.0268	0.0804	0.0536	2.8284	0.9990	0.9980	0.9980
LV4	80	0.1473	1.0134	0.2946	8	0.9822	0.9650	0.9650
LV5	40	1.8973	9.4866	3.7946	5	0.8601	0.7545	1

The first source of uncertainty encountered in utilizing the representation of the ground truth from the SCD and RVSCD datasets was that different local experts had their own set of guidelines to manually segment the left and right ventricles. However, once the rules defined in Section 3.1.1.5.1 and Section 3.1.1.5.2 were presented to the observers, the inter-expert variability decreases. For this study, trabeculae and papillary muscles were included in the ventricular segmentation. Thus the results of the Visual Assessment by Experts was within a

four percent variability. It must also be noted that having the three experts present in the same venue at the same time was logistically difficult. Instead, the segmentations were provided to them on an individual basis which led to the process being time consuming.

As expected from the results in Table 3-2 and Table 3-4, when assessing the accuracy of the ground truth representation against itself, all the distance measures are zero and all the statistical overlap measures are one. For the two point deviations (RV2, RV3, LV2 and LV3), the distance measures are very similar. The Hausdorff distance gives a better indication to the degree of point displacement than the other distance measures as it does not depend on the number of contour points. The Jaccard index and Dice-coefficient do depict that there are some non-overlapping areas between the segmentation and ground truth. The Sensitivity measure will always be one if the ground truth is completely overlapped by the segmented area and thus can be misleading as to the segmentation accuracy. For the segmentations with large point misplacement (RV5 and LV5), the value of the distance measures increase significantly. Once again the Hausdorff distance provides a true indication of the degree of the pixel-wise point displacement with values of 8 and 5 respectively. The statistical overlaps are also significantly affected.

Table 3-3 illustrates the effect that the reduction in segmentation points has on distance and statistical accuracy methods. It can be seen for small point variations (RV2 and RV3) that mean, mean square error and Euclidean distance measures almost doubled. This is due to the $1/2M$ and $1/M$ factors equations (3.11), (3.12) and (3.14). However, as more points are displaced from the ground truth (RV4 and RV5), the distance errors mimics the larger contour errors due to the fact that less number of points are displaced in the smaller contour count. It must also be noted that all the statistical accuracy measures and the Hausdorff distance measure remains within 5% irrespective of the number of displaced points for varying contour sizes.

3.4 Effectiveness of clinical based measures

A dataset of 10 volunteers from the Universitas Hospital (University of the Free State) was used to calculate the various clinical measures. The dataset consisted of five male volunteers and five female volunteer with no known cardiac abnormalities. Each image is of size 256x256 pixels, 20 images per cardiac cycle and a slice thickness of 9mm. Together with each dataset is a set of three manually delineated contours, from three experts, that segment the left and right ventricle in the SAV view from the apex slice to the base slice.

In order to perform the volumetric calculation, each contour area was calculated per slice and converted from pixel value to actual area value represented in cm^2 by using the DICOM information. Thereafter, by applying Simpsons rule for measuring volumes, each slice area was multiplied by the slice thickness and a summation of each volume was performed from the apex slice to the base slice.

Table 3-5 contains all the volumetric information for the left and right ventricle calculated for each expert delineation [19]. The stroke volume error from (3.22) is also presented. Figure 3-12 depicts the deviation from the ideal ventricle volumes for one expert. The average stroke volume is calculated over all three experts for each patient dataset and an error plot showing the deviation from the ideal is presented in Figure 3-13.

Table 3-5: Stroke volume error calculations from three experts on an MRI dataset of 10 patients.

Volunteer Number	Expert 1			Expert 2			Expert 3		
	LV SV (ml)	RV SV (ml)	SV _{error} (%)	LV SV (ml)	RV SV (ml)	SV _{error} (%)	LV SV (ml)	RV SV (ml)	SV _{error} (%)
1	91.8	81.5	11.22	81.5	66.1	18.90	71.1	81.0	13.92
2	53.6	56.3	5.04	49.3	34.8	29.41	45.0	33.3	26.00
3	56.5	54.8	3.01	49.8	42.9	13.86	45.9	71.1	54.90
4	37.9	28.9	23.75	37.7	22.7	39.79	43.2	28.8	33.33
5	86.8	74.1	14.63	81.3	34.6	57.44	77.4	77.4	0.00
6	76.8	64.0	16.67	74.4	61.2	17.74	86.4	77.4	10.42
7	53.7	45.7	14.90	46.6	30.0	35.62	52.2	46.8	10.34
8	53.7	43.6	18.81	51.8	46.1	11.00	62.1	52.2	15.94
9	72.2	77.0	6.65	65.6	63.5	3.20	78.3	70.2	10.34
10	54.3	51.3	5.52	57.6	53.6	6.94	56.7	63.9	12.70

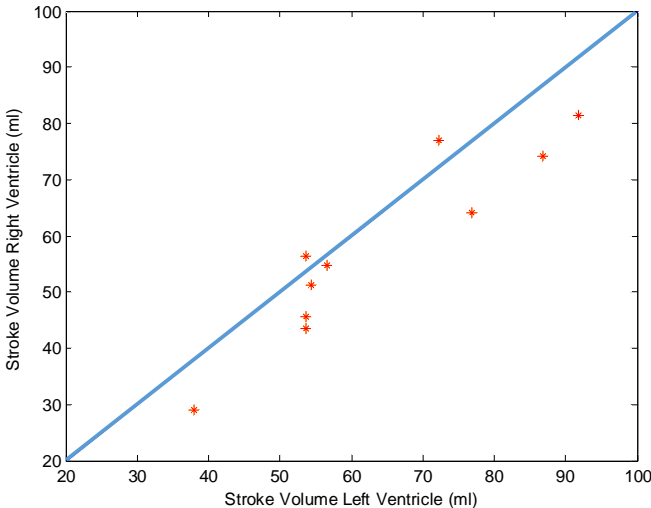


Figure 3-12: Stroke volume for left and right ventricles for Expert 1. Blue line represents the ideal stroke volume.

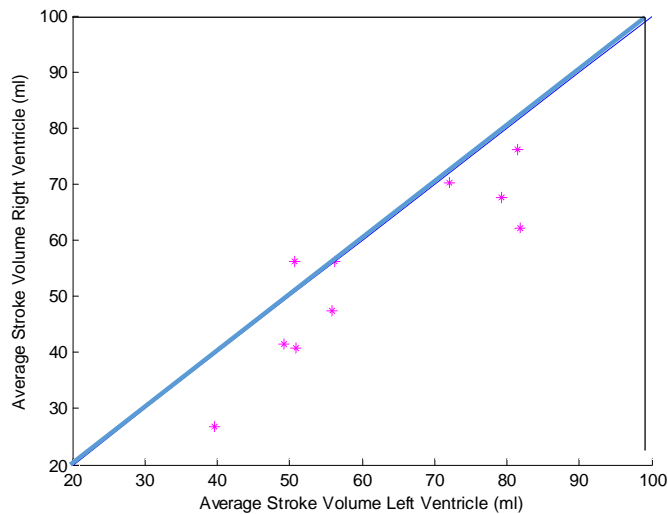


Figure 3-13: Stroke volume for left and right ventricles for average of three experts. Blue line represents the ideal stroke volume.

As can be inferred from Table 3-5, there is a variation in the stroke volume errors between volunteers and also between experts. Simpson's method can be one factor that influences the stroke volume error per volunteer. The inter-expert variation can be attributed to the interpretation of the set of rules in performing the manual delineation. Figure 3-12 shows graphically the segmentation error for Expert 1 around the blue line which represents the equality of the stroke volumes of the left and right ventricles. For four volunteers, the clinical segmentation accuracy is within 7%. Averaging the stroke volume error among the three experts may not necessarily improve the segmentation accuracy due to the inter-expert variability (Figure 3-13).

3.5 Summary

This chapter has presented a series of mathematical, statistical and clinical measures that can be used to calculate the accuracy of the segmentation performed on cardiac MRI. The mathematical and statistical methods are dependent on the availability of a ground truth segmentation. The difficulty in obtaining a representation of the ground truth is due to inter-expert variability and the set of rules that define an accurate segmentation, such as the inclusion or exclusion of papillary muscles. The lack of publically available datasets with ground truth segmentations of the left and right ventricle further hamper segmentation algorithm comparisons. It is proposed that the datasets of SCD, RVSCD and YUD be used as they are supplied with ground truth representations by expert manual delineations. However, these ground truth representations are subjective and conform to a set of rules that the expert has used.

Phantoms (physical or digital) can be used to obtain the ground truth segmentation of the ventricles. However, work in this field is still at its infancy and it shows the difficulty of constructing a phantom that displays a full range of characteristics, such as partial volume effect and noise. In the absence of the ground truth, it is proposed that the visual assessment of segmentation method be used. This method is time-consuming and not suitable for real time diagnosis. The STAPLE algorithm may also be used, but this algorithm requires a large segmented dataset. A method of obtaining a representation of the ground truth by expert manual delineation is also discussed.

The mathematical or distance based measures are particularly sensitive to the "panhandle problem", where there is a strong local deviation that does not necessarily take up much volume, but results in a large shape difference. Furthermore, it was shown that the Hausdorff distance is one of the best to use, due to the small number of pixels between the ventricles. Region based measures are sensitive to misplacement of the segmentation contour. Jaccard is numerically more sensitive to mismatch than Dice. Region based measures become unsuitable for objects that differ in size. The clinical measure required that both left and right ventricle segmentation be performed at the end diastole and end systole, so that the stroke volume could be computed. This measure did not require the ground truth.

Depending on the type of ventricle segmentation algorithm (manual delineation, semi-automatic, fully automatic), if at least two of the mathematical, statistical or clinical measure are used, it will provide a good indication of the accuracy of the algorithm. Thus the effectiveness of various algorithms can be assessed and compared.

CHAPTER 4 - EXISTING CARDIOVASCULAR MRI SEGMENTATION APPROACHES

Ventricle segmentation methods can be represented in three categories namely manual segmentation, semi-automatic segmentation which requires human interaction and fully-automatic segmentation [2]. The manual segmentation methods are normally performed by medical experts who have a defined set of rules as to what anatomical objects to include and exclude in a segmentation. The semi-automatic method requires limited assistance from the user, which normally includes specifying the centre of the ventricle or tracing a part of the ventricle border. In literature, most existing methods have focused in segmenting the left ventricle in the short axis MRI view [2]. The semi-automatic and fully automatic methods can be further broken down into four categories namely; image based or intensity models, active contours or deformable, model based and registration based. These will be explained further in the subsections below. A full review on how these segmentation methods are applied to CMRI is provided in [2] and [25].

4.1 Image and Intensity Based Segmentation

Image and intensity based segmentation methods perform some form of processing on the pixel intensities in the MRI image, by exploiting different features such as edges, texture and shapes. The types of processing include edge based filters, thresholding and region based analysis or dynamic programming which searches for optimal paths. These techniques require little or no prior knowledge of the region of interest. A literature survey of the methods used to segment ventricles in cardiac MRI is presented in Table 4-1.

Edge based filters aims to find the boundary between portions of the image that show intensity discontinuities or an abrupt local change in the pixel intensity. There are several standard edge detection filters present in literature, which can be grouped by either being gradient based or Laplacian based [26]. Gradient based edge detectors find the boundaries by looking for the maximum and minimum in the first order derivative of the image, whereas Laplacian based finds the zero crossings in the second derivative of the image.

Table 4-1: List of image and intensity based segmentation methods provided by various authors

No.	Author	Filter or Thresholding Type	Ventricle Segmented	Dataset and MRI View Used for Results
1	Goshtasby et al. [81]	Laplacian of Gaussian	Left and Right	Own, SAV
2	Kaushikkar et al. [82]	Laplacian of Gaussian (3D)	Left	Own, SAV
3	Weng et al. [83]	Bell image intensity model	Left and Right	Own, SAV
4	Nachtomy et al. [84]	Gradient-echo protocol	Left	Own, SAV
5	Waiter et al. [85]	2D weighted polynomial fitting	Left	Own, SAV
6	Katouzian et al. [86]	Threshold decomposition opening	Left and Right	Own, SAV
7	Lin et al. [52]	Fourier Transform	Left	Own, SAV
8	Liu et al. [87]	topological stable-state thresholding	Left	SCD, SAV
9	Lee et al. [88]	Region growth with iterative thresholding	Left	Own, SAV

For an image P_i that consists of a set of $m \times n$ pixel, referenced by location (x, y) and intensity $I_{i(x,y)} = P_i(x, y)$, the gradient of the image is given in (4.1) and its vector magnitude represented in (4.2) [27]. Thus the gradient vector points in the direction of maximum rate change in $\nabla I_{i(x,y)}$ at coordinates (x, y) , where G_x and G_y is the first order derivative with respect to (x, y) .

$$\nabla I_i = \begin{bmatrix} G_x \\ G_y \end{bmatrix} = \begin{bmatrix} \partial I_i / \partial x \\ \partial I_i / \partial y \end{bmatrix}, \quad (4.1)$$

$$|\nabla I_i| = \sqrt{G_x^2 + G_y^2}. \quad (4.2)$$

Some of the gradient based edge detectors are Sobel, Robert Cross and Canny [28]. The Laplacian based edge filter is given by the second-order derivative given by [27]:

$$\nabla^2 I_i = \left[\frac{\partial^2 I_i}{\partial x^2} + \frac{\partial^2 I_i}{\partial y^2} \right]. \quad (4.3)$$

The one dimensional Gaussian filter [29] can be created in terms of the normal distribution function given below, where σ (sigma) defines the width of the distribution:

$$G(x) = \frac{1}{\sqrt{2\pi}\sigma} e^{-\frac{x^2}{2\sigma^2}}. \quad (4.4)$$

The Gaussian filter can be extended to a two dimensional space for images, as depicted in (4.5) by the product of two Gaussians [30]. $G_1(x, y)$ will form a matrix with x being the distance from the origin in the horizontal axis and y the distance from the origin in the vertical axis.

$$G(x, y) = \frac{1}{2\pi\sigma^2} e^{-\frac{x^2+y^2}{2\sigma^2}}. \quad (4.5)$$

The disadvantage of edge based detectors is that they assume that every sub-region in an image is sufficiently uniform so that the transition between the two regions can be determined purely on the basis of discontinuities [28]. Furthermore, these methods are susceptible to noise and thus some form of pre-processing, such as image smoothing, need to be performed.

Region based analysis attempts to group a set of pixels according to intensity, colour and texture. Thresholding is the simplest form of region based analysis whereby the object of interest is separated from the background by choosing the qualifying value as depicted below [28]:

$$B(x, y) = \begin{cases} 1, \forall I_i(x, y) > T \\ 0, \forall I_i(x, y) \leq T \end{cases}. \quad (4.6)$$

Equation (4.6) will result in the creation of a binary image. If the threshold qualifying value, T , is constant throughout the whole image, the process is known as global thresholding. Variable thresholding is achieved by allowing T to be changed in the image according to some algorithm. The challenge in the region based approach is to select the optimal T per image. These thresholding techniques become effective only if the pixel intensities of the segmented object fall outside the range of the intensity levels of the background and becomes problematic at blurred region boundaries.

4.2 Active Contours and Deformable Models

Deformable models have been the pioneering segmentation method used for ventricle segmentation during the 1980s and 1990s. It was made popular by the introduction of active contours or snakes [53] [54], in which the contours iteratively deform their shapes according to internal and external forces. The internal forces, which are the regularisation terms, control the smoothness of the curve. The focus of the algorithm development is to optimise the external forces, which pulls the contour towards the segmentation region. The advantage of the active contour segmentation method is that it will always produce a continuous boundary segmentation.

The active contour algorithm is initialised by a set of control points, S_{P_i} , that aim to segment object O_j in the image P_i with M points and is represented as:

$$S_{P_{O_j}} = \{(x_{1,P_{O_j}}, y_{1,P_{O_j}}), (x_{2,P_{O_j}}, y_{2,P_{O_j}}), \dots, (x_{M,P_{O_j}}, y_{M,P_{O_j}})\}. \quad (4.7)$$

The control points form the contour with a smooth curvature, where the control points are evenly spaced and the contour adheres to image edges [31]. The process involves minimising the energy function below:

$$E(S_{P_{O_j}}) = \sum_{S_{P_{O_j}}} \left(\underbrace{\alpha E_{continuity}(S_{P_{O_j}}) + \beta E_{curvature}(S_{P_{O_j}})}_{\text{internal forces}} + \underbrace{\gamma E_{image}(S_{P_{O_j}})}_{\text{external force}} \right) \quad (4.8)$$

where α , β and γ are the controlling coefficients, depending on whether even control point spacing, contour smoothness or binding the contour to the edge takes preference respectively [31].

A review of all different external forces methods is provided in [2] and [26] and a summary of the state of the art work is provided in Table 4-2. The initial methods involved focussing on edge detection or boundary detection [89], [90], [93] using approaches similar to those described in Section 4.1, where the contour starts at some initial point and then deforms to the boundary of the epicardium or endocardium. However, these approaches require the ventricle boundaries to have sharp intensity transitions and very low noise. Improvements in the active contour algorithms utilise region based terms, where the intensity and texture are considered within sub-regions of the image and overlaps between regions of different intensity profiles forms the segmentation. These methods are highly dependent on the overlap criteria specified which usually requires assistance from the user for the first segmented image. Another improvement was to replace the edge or boundary detection with the use of a gradient vector flow (GVF) field [120], which is calculated as a diffusion of the gradient vectors of an edge or boundary map as computed from the image and allows convergence of the contours from both inner and outer sides.

All the improvements discussed above allow the contours to shift predefined points based on the chosen energy minimisation function. Another approach of active contour segmentation for cardiac MRI is to use the level set theory developed by Osher et. al. [155] or geodesic active contour introduced by Caselles et al. [156]. With this approach, the contours move completely as a particular level of a function, with the initial contour being at the zero level. This approach catered for the segmentation of multiple objects. Combination of both level sets and edge or region based have been investigated, which improved efficiency in both initialisation and convergence [26].

The major step or downfall in the deformable methods is the initialisation of the active contours and in most cases the algorithms are slow converging [31]. User interaction is also a requirement, either minimally or extensively, especially at the initialisation of the contour stage. The presence of image noise and low contrast on the ventricles still pose challenges with these methods.

Table 4-2: List of deformable model segmentation methods developed by various authors

No.	Author	Deformable Model Type	Ventricle Segmented	Dataset and MRI View Used for Results
1	Ranganath [89]	Active contours – Edge	Left	Own, SAV
2	Heiberg et al. [90]	Active contours – Edge (3D)	Left	Own, SAV
3	Hautvast et al. [91]	Active contours – Region	Left and Right	Own, SAV
4	Zhukov et al. [92]	Active contours – Region (3D)	Left	Own, SAV
5	Chakraborty et al. [93]	Active contours – Edge and Region	Left	Own, SAV
6	Santarelli et al. [120]	Active contours – Edge and Gradient Vector Flow	Left	Own, SAV
7	Wang et al. [121]	Active contours – Edge and Gradient Vector Flow	Left	Own, SAV
8	El Berbari et al. [122]	Active contours – Edge and Gradient Vector Flow	Left	Own, SAV
9	Wu et al. [123]	Active contours – Edge and Gradient Vector Flow	Left	Own, SAV
10	Pham et al. [124]	Active contours – Region and Gradient Vector Flow (3D)	Left	Own, SAV
11	Pieciak [125]	Active contours and Fourier descriptors	Left	Own, SAV
12	Gotardo et al. [126]	Active contours and Fourier descriptors and Principle component analysis (3D)	Left	Own, SAV
13	Battani et al. [127]	Level set	Right	Own, SAV
14	Ammar et al. [128]	Level set and Active contours – Edge	Left	Own, SAV
15	Pluempitiwiriyaewj et al. [129]	Level set and Active contours – Edge and Region	Left and Right	Own, SAV
16	Paragios [130]	Level set and Gradient Vector Flow	Left	Own, SAV
17	Yezzi et al. [131]	Level set and Principle Component Analysis	Left	Own, SAV
18	Lynch et al. [132]	Level sets and coupling of contours	Left	Own, SAV
19	Ben Ayed et al. [133]	Level set and coupling of contours	Left	Own, SAV
20	Ngo et al. [134]	Level sets and Deep belief networks	Left	SCD, SAV

4.3 Model Based Segmentation

Model based segmentation exploits a prior knowledge about the properties of an object of interest which is to be segmented [2]. The shape and appearance of the left ventricle is well

known in the SAV. Using this knowledge, an automated segmentation algorithm/model can be developed. This model is then superimposed over the unknown, un-segmented patient data. The model's appearance and parameters are subsequently adjusted until the model matches the un-segmented data within a defined tolerance value. The final shape and position of the model will reflect the shape and position of the object of interest.

Active Appearance Models of the human heart do exist [32]. These represent the appearance of the heart in terms of statistical features which considers the spatial form of the ventricles (shape) and the volumetric colour distribution inside the ventricle (texture) [33]. Multiple instances of similar data are analysed statistically to obtain a model.

In order to segment an image, the image is matched to the model iteratively, until the difference between model and MRI image is minimised. The shape variation of the model is commonly achieved by using Principal Component Analysis (PCA) [34], on a training dataset of example shapes, to describe the main direction of variance. However, these models assume that the data is normally distributed, which is not always the case. Respiration, fat and any movement of the patient while the MRI is being performed will result in large shape variations. This may lead to a creation of a model that has the incorrect desired shape. Another problem with this method is that appearance matching may lock on incorrect features and get stuck in a local minimum. This is a problem for quantitative analysis. Also, local structures and boundary information is not specifically considered.

Active shape models (ASM) and Active appearance models (AAM) are both statistical models that consider both shape and texture variability within a training set. ASM only considers the texture distribution surrounding landmark points. Landmark points are the significant points that segment the area of interest. The general method in creating these models is to have N training dataset of images, with each image having M landmark points, which outlines the area of interest.

If an object O_j in the image P_i has been segmented the resultant training set by M landmark points is represented as:

$$S_{P_i O_j} = \{(x_{1,P_i O_j}, y_{1,P_i O_j}), (x_{2,P_i O_j}, y_{2,P_i O_j}), \dots, (x_{M,P_i O_j}, y_{M,P_i O_j})\}. \quad (4.9)$$

For 2D images these n landmark points can be represented as [33]:

$$S_{P_i O_j} = \{x_{1S,P_i O_j}, x_{2S,P_i O_j}, \dots, x_{MS,P_i O_j}, y_{1S,P_i O_j}, y_{2S,P_i O_j}, \dots, y_{MS,P_i O_j}\}^T. \quad (4.10)$$

The above representation (4.10) is a vector in $2M$ dimensional space. The training set now can be represented as:

$$S_{O_j} = (S_{P_1 O_j} | S_{P_2 O_j} | S_{P_3 O_j} | \dots | S_{P_N O_j}). \quad (4.11)$$

The first step in building a model is to align each training vector in S_{O_j} into a common coordinate frame. There are various methods to achieve this [33]. Assume S_{O_j} is now aligned to produce $\overline{S_{O_j}}$.

The next step is to reduce the dimensionality of the aligned training vector $\overline{S_{O_j}}$, by applying principle component analysis. PCA will produce a set of eigenvectors, $PCA_{O_j} = (p_1 | p_2 | p_3 | \dots | p_{2M})$, that are orthogonal to each other and its associated eigenvalue vector, $\lambda_{O_j} = (\lambda_1, \lambda_2, \lambda_3, \dots, \lambda_{2M})$. The eigenvector p_e corresponding to the largest value of λ_e is called the principle component. In essence, if we choose g eigenvectors (p_e) corresponding to the largest values of λ_e we can approximate any of the aligned training vectors $\overline{S_{P_1 O_j}}$ by [33]:

$$\overline{S_{P_1 O_j}} \approx \overline{S_{P_1 O_j}} + PCA_{O_j} b, \quad (4.12)$$

where $\overline{S_{P_1 O_j}}$ is the mean of $\overline{S_{P_1 O_j}}$ and:

$$b = PCA_{O_j}^T (\overline{S_{P_1 O_j}} - \overline{S_{P_1 O_j}}). \quad (4.13)$$

$PCA_{O_j}^T$ now forms the model and b is the shape parameter. To recover the original image points $S_{P_1 O_j}$, the following equation is applied iteratively [33]:

$$S_{P_1 O_j} = T_{X_t, Y_t, s, \theta} (\overline{S_{P_1 O_j}} + PCA_{O_j} b), \quad (4.14)$$

where $T_{X_t, Y_t, s, \theta}$ performs a rotation by θ , a scaling by s , and a translation by X_t, Y_t .

To fit the model to a new image is a little tricky. A set of parameters, that define shape and position, must be found that best matches the model to the image. The parameters that can be varied are b, X_t, Y_t, θ, s . To aid in the matching/searching process, texture surrounding each of the model points are considered.

There are various searching algorithms and improvements that have been developed. Table 4-3 provides detail on the different approaches made by various authors in improving ventricle segmentations using ASM and AAM. Mitchell et al. [35], was the first to apply AAM to automatically segment the left and right ventricles of the heart. They developed a hybrid ASM/AAM which improved the searching method in AAM. Mitchell et al. extended their research to produce a full 3D AAM, and applied it to 3D cardiac MR data and 2D + time

echocardiograms [37]. Results of the above applications of AAM have shown to be superior to other segmentation approaches, since they combine correlated intensity and shape knowledge, resulting in increased robust performance.

Table 4-3: List of shape model segmentation methods developed by various authors

No.	Author	Shape Model Type	Ventricle Segmented	Dataset and MRI View Used for Results
1	Mitchell et al. [35]	AAM	Left	Own, SAV
2	Stegmann et al. [15]	AAM	Left	Own, SAV
3	Mitchell et al. [37]	ASM and AAM	Left and Right	Own, SAV
4	Lelieveldt et al. [95]	AAM (3D)	Left	Own, SAV
5	Mitchell et al. [94]	AAM (3D)	Left	Own, SAV
6	Ordas et al. [135]	ASM and Invariant optimal features	Left and Right	Own, SAV
7	Stegmann et al. [136]	AAM (3D)	Left	Own, SAV
8	van Assen [48]	ASM (3D)	Left	Own, SAV
9	Abi-Nahed et al. [137]	ASM and Robust point matching	Right	Own, SAV
10	Zambal et al. [138]	ASM (3D) using 2D AAM	Left	Own, SAV
11	Zhang et al. [139]	ASM and AAM (3D)	Left and Right	Own, SAV
12	Davatzikos et al. [38]	ASM and Wavelet Transforms	Left	Own, SAV
13	Mehmet [40]	AAM with Independent component analysis	Left and Right	Own, SAV
14	Yuan et al. [41]	ASM and Support Vector Machines	Left	Own, SAV
15	Beichel et al. [42]	AAM with improved searching	Left	Own, SAV
16	Andreopoulos et al. [9]	AAM (3D) with improved searching	Left	YUD, SAV

An interesting approach was developed by Davatzikos et al. called hierarchical active shape models using the wavelet transform [38]. Here the data is decomposed into the wavelet transform and thereafter PCA is performed on each wavelet band separately. With this method global and local shape variations can be described and the performance of this method is better than standard ASM when a small number of training samples is used. However, when the training dataset is large, the performance is comparable to standard ASM.

An effective method as an alternative to PCA is called Independent Component Analysis (ICA). Vectors computed using ICA show localised shape variation. The selection of ICA vectors to use in the shape model is not natural as with PCA. Several methods do exist that make this choice of vectors. Mehmet has developed a novel method of combining PCA and ICA using AAM [40]. This method was successfully applied in segmentation of short-axis cardiac MRI. ICA was used in the shape model, while PCA was used in the texture modelling.

Support Vector Machines (SVM) has shown potential for learning classification functions that can be applied to object recognition. SVM finds strength in object discrimination. Yuan et al [41] have successfully combined ASM and SVM to produce a better segmentation model. Beichel et al [42] have developed the Robust Active Appearance Model (RAAM). Their main focus was to optimise the searching method by means of mean-shift based mode detection. Also in their algorithm, they have made no assumptions about the distribution of noise disturbances in the image to be matched (to the AAM model). They claim that this method is robust enough to tolerate up to 50% of image area covered by noise disturbances.

One of the major issues with the AAM is that it uses PCA which describes the main direction of shape variation within a training data set. However, PCA fits a Gaussian hyper-ellipsoid to the training data set and thus assumes that the data is normally distributed, which in most cases it is not. Furthermore, PCA produces eigenvectors which describe global variations, in that if a shape parameter that corresponds to a particular eigenvector is changed, the entire shape deforms. This poses a serious problem if we are trying to achieve a locally accurate segmentation.

4.4 Registration Based Segmentation

Registration based methods utilises an atlas that describes the different structures (ventricles) present in the image. Image segmentation is performed by mapping the target image coordinates to the atlas by using a registration process by means of a mathematical transform [43]. Thereafter, segmentation of ventricles throughout the entire cardiac cycles is possible by utilising the same principle. Registration based segmentation methods have only recently (from 2010) gained popularity and research interest [4]. The focus of the research investigated various registration algorithms to match atlases to target cardiac MRI and also strategies for atlas construction. Table 4-4 summarises the state of art research in this field.

The initial step in these approaches is the creation of the atlas, which is normally obtained from a selection and combination of expert manually delineated images which extracts the ventricles. The initial works by Lorenzo-Valdes et al [44] [140], used only a single atlas, and thus the atlas was constructed by means of averaging over a several manually delineated images. Since 2008, multi-atlas segmentation started to become popular [143] and hence the atlas set consisted of multiple segmented images, where each image is treated equally for the registration portion.

If an object O_j in the image P_i has been segmented with points $S_{P_i O_j}$ the resultant atlas of size N created is denoted as follows:

$$A_i = (P_i, S_{P_i O_j}), i = \{1, \dots, N\}. \quad (4.15)$$

Table 4-4: List of atlas based segmentation methods developed by various authors

No.	Author	Atlas Registration Type	Ventricle Segmented	Dataset and MRI View Used for Results
1	Lorenzo-Valdes et al. [44]	Non rigid registration (NRR)	Left and Right	Own, SAV
2	Lorenzo-Valdes et al. [140]	Expectation minimisation, NRR	Left and Right	Own, SAV
3	Lotjonen et al. [141]	Principle component analysis, Expectation minimisation, NRR	Left and Right	Own, SAV
4	Zhuang et al. [142]	Local Affine transform and NRR	Left and Right	Own, SAV
5	İşgum et al. [151]	NRR and Weighted decision fusion	Left	Own, SAV
6	Zhuang et al. [143]	NRR and patch-based label fusion	Left and Right	Own, 2CV and 4CV
7	Zuluaga et al. [144]	Affine transformation and locally normalised cross correlation	Left and Right	RVSCD, SAV
8	Ou et al. [145]	NRR, attribute-based	Right	RVSCD, SAV
9	Bai et al. [146]	B-spline NRR, Gaussian kernels	Right	RVSCD, SAV
10	Zhuang et al. [147]	Region Based and Fluid registration	Left and Right	Own, SAV and 2CV
11	Kirisli et al. [148]	affine transformation and B-spline NRR	Left and Right	Own, 2CV and 4CV
12	Hoogendoorn et al. [149]	NRR with spatial normalization	Left and Right	Own, 2CV and 4CV
13	Yang et al. [150]	affine transformation and B-spline NRR	Left and Right	Own, 2CV and 4CV
14	Tsadok et al. [57]	Fast Marching Method and B-spline NRR	Left	Own, 2CV and 4CV

Several methods have been proposed to differentiate images in the atlas and to preselect the ones that are most suited to segment the target image. These methods include visual inspection [150], feature selection [151] and population level processing [147]. Pre-processing of the atlas images may be performed to further sort the atlas so that it aids the registration process to efficiently compute distances between the atlases and target image.

The next step in the segmentation method is to obtain spatial correspondence between each atlas image P_i and the target image to be segmented P_{Target} . This is achieved by using a registration method $T_{i X_t, Y_t, s, \theta}$, which performs a rotation by θ , a scaling by s , and a translation by X_t, Y_t . In this way a set of registered atlas is formed which can be represented as:

$$\tilde{A}_{P_{Target}} = T_{i X_t, Y_t, s, \theta}(A_i) = (\tilde{P}_i, \tilde{S}_{P_i O_j}), i = \{1, \dots, L < N\}. \quad (4.16)$$

It must be noted that a subset, L , of the total number in the atlas is chosen for the registration. The resultant \tilde{S}_{p,o_j} are then fused together by a fusion criteria to form the final segmentation of the target image P_{Target} .

In literature, several authors have proposed different methods in which the registration and fusion processes are performed so that the computational cost is kept to a minimum and segmentation accuracy to a maximum. The initial research used non-rigid registration, where the transformation that accounts for elastic deformations and the similarity between the atlas and the target image is maximised. Thereafter, several other methods such as expectation minimisation, Markov random fields, deformable registration, etc. [44] [45] have been used.

Registration based methods are dependent on the creation of the atlas, which is normally obtained from a large set of manually segmented images. Due to the registration process, the segmentation is computationally expensive, depending on the size of the atlas used. There is a trade-off between a reduction of atlas pool size and the accuracy of the segmentation.

4.5 Other Segmentation Approaches

There are several other image segmentation methods that have been applied to cardiac MRI, but are less popular than those described above. The graphcut method [96], [97], [100] and [152] aims to perform segmentation by constructing a graph that separates the boundary and region information of the ventricles from the rest of the image, by utilising a minimal cost algorithm. For this to happen, the pixel vertices are the graph nodes and the boundary pixels are the edges of the graph. The graph edges are assigned weighting which is obtained from the image gradient magnitude and directional information [96]. Thus segmentation is obtained by finding a minimum cost path between the start and end vertex. This method normally requires expert user interaction for the initial vertices. To minimise on the user interaction, hybrid models have been proposed that utilise shape models or atlas based models [98] and machine learning [99].

Pixel classification approaches find use where disconnected regions in an image or set of images belonging to the same tissue class need to be identified. The regions normally have similar grey-level values and segmentation is performed by either Gaussian Mixture Model fitting using the Expectation minimisation algorithm or clustering (K-means or Fuzzy). A list of these approaches is presented in Table 4-5.

Table 4-5: List of pixel classification segmentation approaches used by various authors

No.	Author	Pixel Classification Type	Ventricle Segmented	Dataset Used for Results
1	Boudraa [101]	Fuzzy Clustering	Left	Own, SAV
2	Gering [102]	GMM and Markov Random Fields	Left and Right	Own, SAV
3	Lynch et al. [103]	K-Means Clustering	Left	Own, SAV
4	Kedenburg et al. [104]	Fuzzy clustering and graphcut	Left	Own, SAV
5	Pednekar et al. [105]	GMM and Fuzzy clustering and graphcut	Left	Own, SAV
6	Cocosco et al. [106]	Clustering	Left	Own, SAV
7	Chittajallu et al. [153]	Knowledge driven Markov Random Field	Left	SCD, SAV

4.6 Location of Region of interest for the ventricles

Several authors have performed a method of locating the region of interest (ROI), which in this case is the heart ventricles, as the initial step to their segmentation algorithm. The reasons for this is that unnecessary information or artefacts (partial volume effects) are removed from the MRI, thereby reducing the computational load. There are various algorithms that can achieve this localisation namely intensity statistics based as recommended in [103], image filter based as described in [52], [108] and motion based as mentioned in [104], [109], [105]. A summary of the methods used to locate the region of the heart is shown in Table 4-6 below.

Table 4-6: List of approaches to determine the region of interest (ROI) around heart.

No.	Author	ROI Detection Method	Ventricle Segmented	Dataset and MRI View Used for Results
1	Lynch et al. [103]	Texture analysis and K-means clustering	Left	Own, SAV
2	Huang et al. [107]	Motion – Texture analysis and K-means clustering	Left	Own, SAV
3	Lin et al. [52]	Fourier Transform	Left	Own, SAV
4	Jolly [108]	Time based Fourier analysis	Left	Own, SAV
5	Hadhoud et al. [109]	Motion – Standard deviation map	Left	Own, SAV
6	Pednekar et al. [105]	Motion – Hough transform	Left	Own, SAV
7	Cocosco et al. [110]	Motion – Variance maps	Left	Own, SAV

Motion based methods rely on that basis that the heart is the only moving organ in the MRI for a cardiac cycle at a particular slice. This method described in [109] depends on calculating the standard deviation motion map between all images for different time frames in the middle slice. Thereafter the resultant standard deviation motion map image is converted to a binary image by applying a threshold. After thresholding, there is a possibility that other objects may be selected. Thus the authors propose to use a window that is of radius 55mm from the centre of the image.

This may not be adequate in patients with larger hearts, but can be adapted upward as required. The use of the Hough transform is also common in these approaches as it has the ability to detect circular regions around the ventricles.

4.7 Summary

This Chapter has provided a literature survey on the most common methods that are used to segment the ventricles of the heart. Amongst the segmentation methods studied, approximately 65.7% of the approaches focused on segmentation of the left ventricle only, 5.7% on the right ventricle only and 28.6% on both the left and right ventricles. Furthermore, approximately 5.7% of the methods presented provided results on the publically available datasets described in Section 3.1.1.5. This poses a challenge when trying to compare newly developed segmentation algorithms to the current state of the art.

Another observation made is that 94.2% of the methods segmented the ventricles in the SAV. From the discussions in Section 3.2, the error with regards to the utilisation of Simpsons rule for the volume calculation could hamper the clinical measures. User interaction in the segmentation process is prominent in registration based, image and intensity based and active contours. Image and intensity techniques become effective only if the pixel intensities of the ventricles fall outside the range of the intensity levels of the background MRI and becomes problematic at blurred region boundaries. Active contours algorithms are slow converging and presence of image noise and low contrast on the ventricles still pose challenges. Model based and registration based segmentation is highly dependent on the training dataset and performs poorly if required to describe local variations such as papillary muscles.

CHAPTER 5 - PROPOSED SEGMENTATION METHODS

The main aim of this research was to develop an automatic ventricle segmentation method that is able to distinguish between the left and right ventricles from cardiac MRI. From the observations presented in Chapter 4, it can be seen that about two thirds of the segmentation algorithms focussed on the left ventricle. Only in recent years has more attention been afforded to the right ventricle and resulted in the Right Ventricle Segmentation Challenge competition [111]. Also, from Chapter 4, it is noticed that segmentation focus was in the SAV. This Chapter will initially propose a new algorithm for automatic segmentation of left and right ventricles in the SAV using an image and intensity based segmentation method. This forms the basis of the next algorithm, to utilise segmentation information from all MRI views concurrently in an iterative fashion to achieve final segmentation.

Section 5.1 provides a brief overview of the algorithm used in the proposed segmentation model. This gives a basic idea of the different sub-components involved in the segmentation process. Thereafter in Section 5.2 reasons are provided as to why there is a need to utilise and segment the ventricles in other MRI views than in the SAV. Section 5.3 will analyse each sub-component in detail and account for the reason of choice in each case. The next Section, 5.4, will describe the approach of segmentation in three MRI views.

5.1 System Overview

This section presents an automatic image and intensity based ventricle segmentation algorithm that uses the difference of Gaussians (DoG) weighting function on cardiac MRIs obtained from multiple views. The choice of utilising this type of method were as follows:

- (i) Segmentation of both left and right ventricles can be performed using image and intensity based methods as described in the review in Section 4.1.
- (ii) The University of the Freestate required that papillary muscles be excluded from the ventricle volume calculations as motivated in [7] and [112]. Model based and registration based methods cannot with ease exclude papillary muscles as the shape and size of these muscles vary.
- (iii) The difference of Gaussians technique is believed to mimic how neural processing in the retina of the eye extracts details from images destined for transmission to the brain [113].

- (iv) There are several factors that provide a challenge to ventricle segmentation in the SAV. These factors include similar intensity profiles across different region of interests, difficulty in identifying ventricles at the end slices, partial volume artefacts, relatively fast movement of the heart during contraction causing blurring and patient movement (both voluntary and involuntary). As a result of the problems above, other MRI information is required to provide an accurate segmentation.

Being a filter based method, several parameters must be chosen with each dependent on the intensity profile of the current image. This selection issue is addressed by proposing an automatic method of choosing the parameters based on the creation of region of interest in close proximity to the ventricles. This segmentation algorithm is presented in Figure 5-1 and discussed in detail in Section 5.3.

5.2 Problems in Segmenting Ventricles when using one MRI View

The quality of MRIs can be severely degraded by noise. Image noise can result from a number of factors which can be grouped into three categories namely those resulting from equipment factors, patient factors and image processing factors [3]. Examples of some of these categories are shown in Figure 5-2 [1].

An MRI, acquired from a patient, consists of a two dimensional matrix of pixels which provides information of a corresponding three dimensional volume element within the patient which is known as a voxel. The size of the voxel is dependent on the MRI slice thickness, field of view and matrix size [3]. As a general rule of thumb, as the voxel size decreases, the MRI resolution increases, which will in turn provide a better representation of the object of interest, but reducing the voxel size comes at a cost. In clinical practice, an optimal slice thickness is sought. Thinner slices can be susceptible to a high level of RF noise, where thicker slices are associated with issues such as increased partial volume effect. To take into account all of these equipment sources of noise, the following parameters are considered and optimised namely; magnetic field strength, number of excitations, echo time, repetition time, flip angle, selection of transmit and receive RF coils [3].

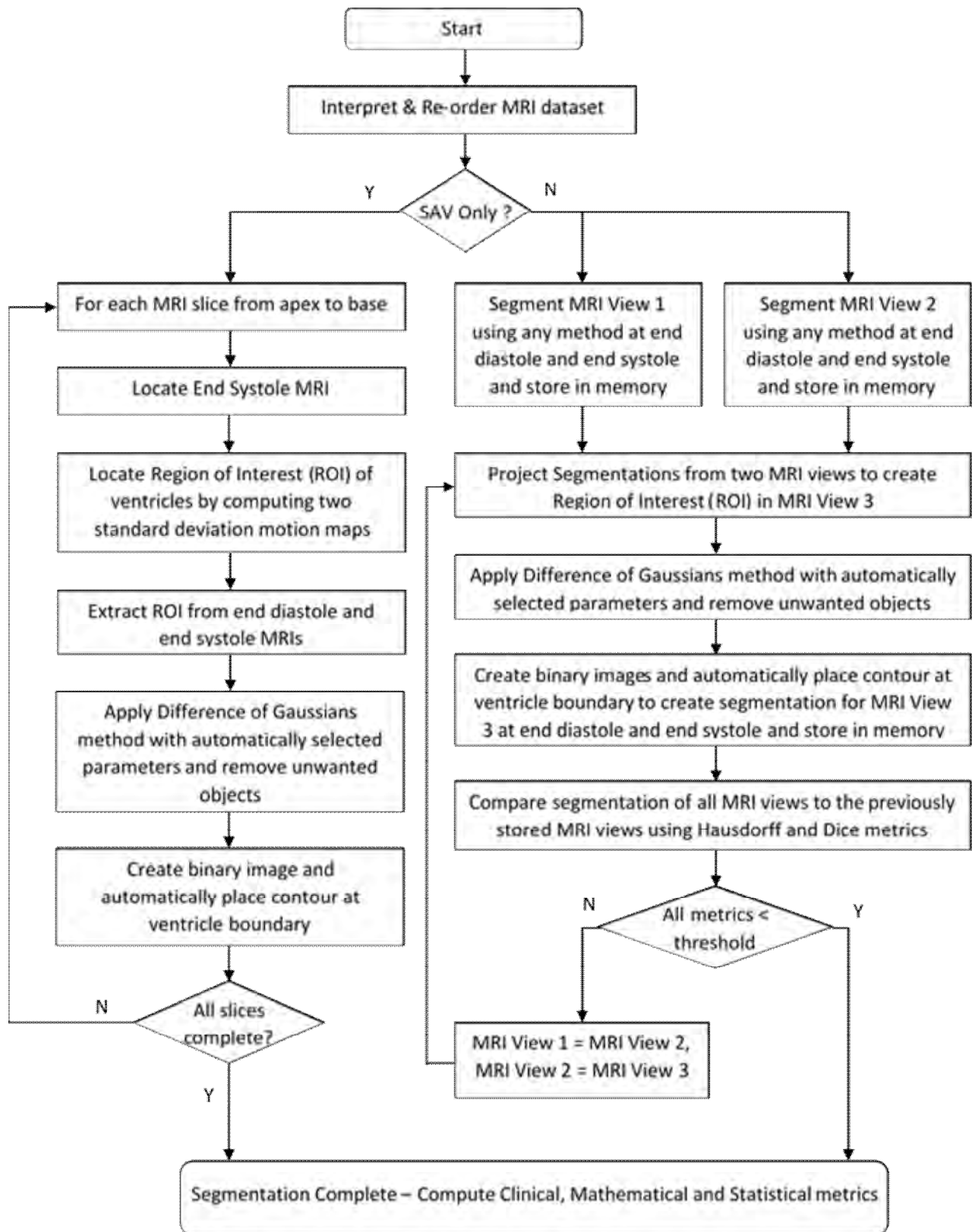


Figure 5-1: Block diagram of the proposed segmentation algorithm

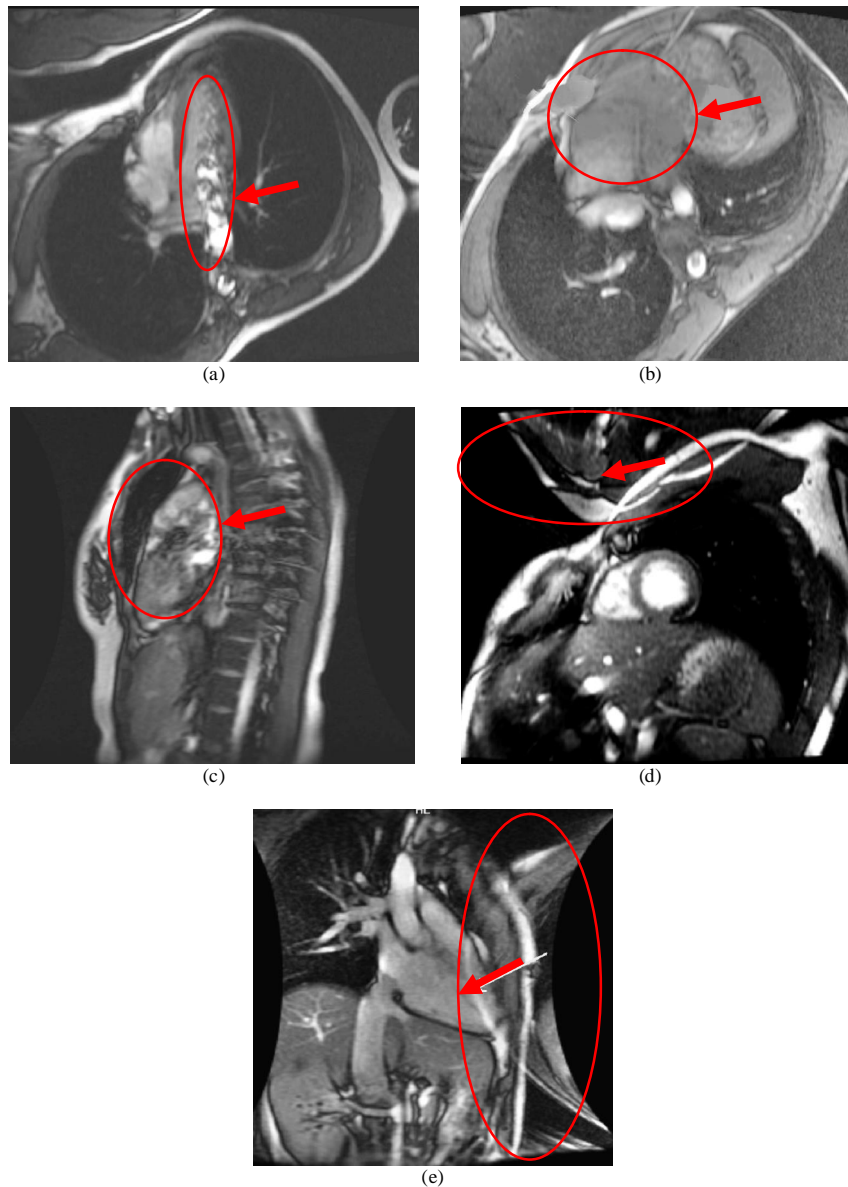


Figure 5-2: Examples of MRI degraded by image noise [1]. (a) Flow artefact affecting the detection of ventricle edge. (b) Partial volume effect causing uncertainty in determining the amount of blood that is from the left or right ventricle. (c) Patient movement - poor image quality and blood intensity not consistent. (d) Wrap around artefact in SAV. (e) Wrap around artefact in 2CV affecting ventricle edge detection.

Patient movement as well as blood flow movement and respiration movement will result in certain artefacts being created which may influence the quality of the image in the object of interest, as well as volumetric calculations. Furthermore, excessive patient movement could disrupt the MRI co-ordinate system, which could lead to different slices being out of sync, thus causing a range of interference effects and other artefacts.

Image processing errors normally stem from the following factors in the SAV, 1) the overlap between the intensity distributions within the cardiac regions; 2) the lack of edge information;

3) the shape variability of the ventricles across slices and phases; and 4) the inter-subject variability of these factors [4]. Furthermore due to voxel sizes, the ventricles at the apex and base slices are more difficult to identify. The presence of papillary muscles further adds to the complexity of ventricle segmentation.

Also, analysis of cardiac functionality is focused and quantified through the ventricle volumes. More specifically, the measures required are the end diastole volume, end systole volume, stroke volume and ejection fraction [1]. These volumetric measurements are dependent on the accuracy of the ventricle segmentation and the MRI slice thickness. Section 3.2 has discussed the problem in ventricle volume calculations using Simpsons rule. Furthermore, if the apex and the base slice is not at the ventricle ends, due to the slice thickness, the calculated volume error increases. Research has been performed at the University of the Freestate, to determine and calculate right ventricular volumes by utilising MRIs from different views [1]. However, this process was very manual. From the discussion above, it can be concluded that if more information and a higher image resolution is provided, some of these issues can be mitigated. This is the basis of the proposed segmentation method, where additional image information is sought from other MRI views.

5.3 Details of the Proposed Algorithm

This section is dedicated in examining the details of the different components in the proposed ventricle segmentation algorithm. The proposed algorithm requires a set of cardiac MRIs obtained for a patient P consisting of a series of N two dimensional images, P_i , and is denoted as follows:

$$P = \{P_i\}, \quad 1 \leq i \leq N, \quad N = S \times T. \quad (5.1)$$

N is a count of the total number of slices, S , from the apex to base of the ventricles multiplied by the number of MRIs per cardiac cycle T multiplied by number of views to segment. Each patient image P_i consists of a set of $m \times n$ pixels referenced by location (x_k, y_l) and intensity $I_{i(x_k, y_l)} = P_i(x_k, y_l)$. The sections below will describe each step in achieving segmentation of both the left and right ventricles.

5.3.1.1 Interpreting and Re-ordering the MRI Dataset

The first step in the proposed algorithm is to manually assess the cardiac MRI dataset to be segmented. This process includes determining the number of MRI views present in the dataset and extracting the images that covers the ventricles from the apex slice to the base slice for the

entire cardiac cycle. The University of the FreeState [1] provided guidelines in selecting the apex and base slice for all three views.

The publically available datasets described in Section 3.1.1.5 only contains MRIs in the SAV. The datasets are already interpreted and ordered such that only the MRIs from the apex slice to the base slice are present and the end diastole and end systole MRIs are also clearly ordered. Thus in order to utilise these datasets, the proposed algorithm is split into two parts, with the first only dealing with segmentation in the SAV and the other with segmentation using multiple MRI views.

5.3.1.2 Identification of End-Systole Image

The next step in the proposed segmentation algorithm is to identify the MRI at the end systole cardiac phase for each image slice s , $1 \leq s \leq S$ and utilise this as the reference, $P_{ref,s}$. The end systole phase is when the ventricles are contracted and contains the least amount of blood. This identification process is manual and guidelines to extract the end systole is once again provided by the University of the FreeState [1]. This step is required if the MRI dataset only contains the SAV.

5.3.1.3 Localisation of the Cardiac Ventricles via Motion Maps

Due to the large distribution of pixel intensity throughout a single MRI, the image needs to be cropped so that the region of interest focuses mainly in the immediate vicinity of the ventricles. There are several approaches to extract the region of interest which is provided in Section 4.6. The approach proposed here builds on the methodology introduced by Hadhoud et al. [109], with the difference being that two standard deviation motion maps are used.

The two standard deviation motion maps are computed per MRI slice and denoted as σ_s and $\sigma_{s,ref}$. The first map (σ_s) is computed as described in [109] and depicted in (5.2), where the standard deviation per pixel for all MRIs in the cardiac cycle per slice s is calculated. T is the number of MRIs per cardiac cycle and μ is the average difference pixel intensity value.

$$\sigma_{s(x_k, y_l)} = \sqrt{\frac{1}{T-1} \sum_j^{T-1} (|I_{s, j+1(x_k, y_l)} - I_{s, j(x_k, y_l)}| - \mu)^2} . \quad (5.2)$$

The second standard deviation map is computed similar to the first, but the difference is applied from the current image $P_{s,j}$ to the end systole image $P_{ref,s}$. In essence the first map provides local motion and the second global motion for that particular slice.

To remove all the unwanted objects and noise from the image, the wavelet transform on the standard deviation motion maps is applied. This is where the proposed method differs from the one in [109]. The wavelet transform has the ability of providing a multi-resolution and multi-frequency decomposition of images. One of the most important properties is that the wavelet transform de-correlates mutually dependent parts of the image and performs an energy compaction of the samples representing the image. Furthermore both anomalies and trends can be analysed on an equal statistical footing. The Discrete Wavelet Transform of an image at scale a_0 is defined as in (5.3), where $b = H, V, D$ (Horizontal, Vertical and Diagonal) and $m \times n$ is the size of P_i [23]. $W_\varphi(a_o, g, h)$ are the approximation coefficients at scale a_0 , while $W_\psi^b(a, g, h)$ are the horizontal, vertical and diagonal coefficients at scales $a \geq a_0$.

$$W_\varphi(a_o, g, h) = \frac{1}{\sqrt{m \times n}} \sum_{x=0}^{m-1} \sum_{y=0}^{n-1} P_i(x, y) \varphi_{a_o, g, h}(x, y)$$

$$W_\psi^b(a, g, h) = \frac{1}{\sqrt{m \times n}} \sum_{x=0}^{m-1} \sum_{y=0}^{n-1} P_i(x, y) \psi_{a, g, h}^b(x, y)$$
(5.3)

The effect of the wavelet transform using the Haar coefficients is depicted in Figure 5-3(a).

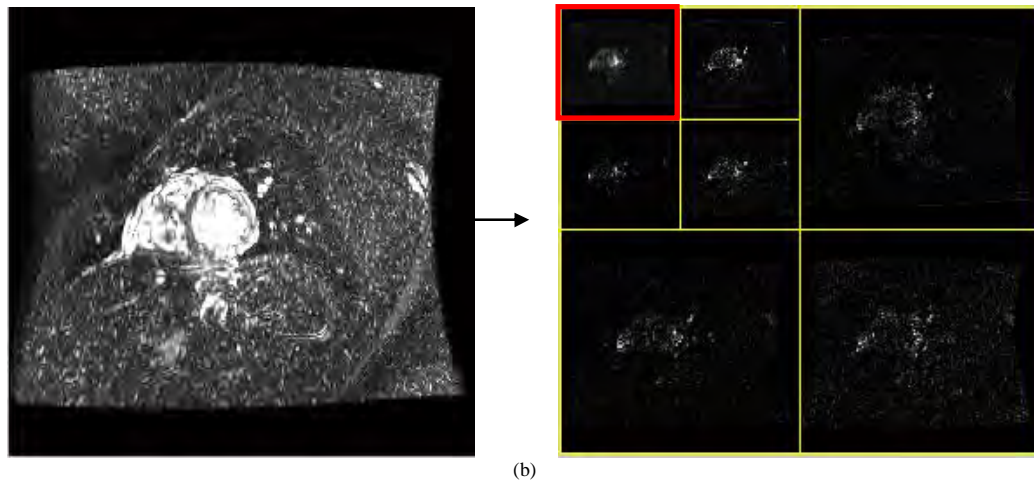
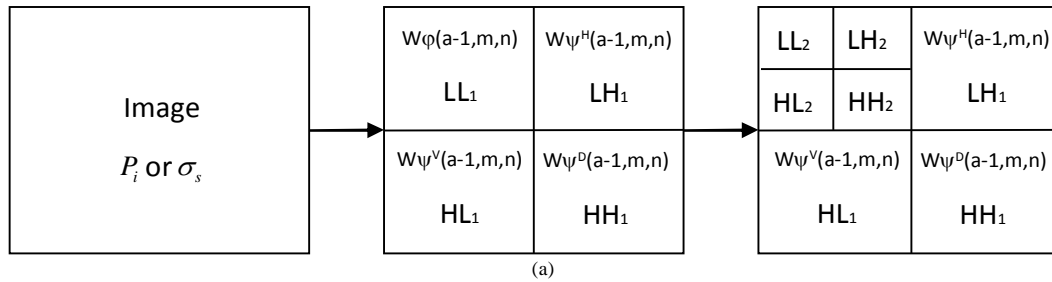


Figure 5-3: Two level discrete wavelet transform on images. (a) Block diagram of the wavelet transform process. (b) Wavelet transform of the standard deviation map.

In order to create the region of interest around the ventricles, the wavelet transform in two levels is applied to both standard deviation motion maps. Figure 5-3(b) displays the resultant

transform of the first standard deviation motion map. From this figure it can be seen that the unwanted areas are distinctly contained in regions the LH, HH and HL regions. Thus these regions are removed and the inverse wavelet transform is performed on LL_2 (demarcated in red in Figure 5-3(b)). All low intensity values from the inverse wavelet transform are removed and each image is converted to a binary image. From the binary image the region of interest is calculated for both standard deviation maps. The final region of interest for slice s is the union of region of interest for the processed inverse wavelet transform of both σ_s and $\sigma_{s,ref}$ and is depicted as ROI_s .

5.3.1.4 Application of Difference of Gaussians within the Region of Interest

5.3.1.4.1 Pixel Statistics in Region of Interest

Once the final region of interest, ROI_s , is calculated as described in Section 5.3.1.3, several pixel statistic measures need to be calculated. These include the maximum intensity value, minimum intensity value, mean intensity value and the grey level co-occurrence matrix [22]. The grey level co-occurrence matrix calculates how often a pixel with intensity value of c , occurs adjacent to a pixel with the value d .

5.3.1.4.2 Selection of Difference of Gaussian Parameters

The one dimensional Gaussian filter [29], from Section 4.1, can be created in terms of the normal distribution function given below, where σ (sigma) defines the width of the distribution:

$$G_1(x) = \frac{1}{\sqrt{2\pi}\sigma_1} e^{-\frac{x^2}{2\sigma_1^2}}. \quad (5.4)$$

As shown in Figure 5-4, the filter decays rapidly at some value of x (position), which in this case is -3 and 3 and for $\sigma = 1$. Although the filter is non-zero for $x \in [-\infty; \infty]$, defining a filter window $-3 \leq x \leq 3$ would yield a reasonable filter implementation with reduced processing complexity.

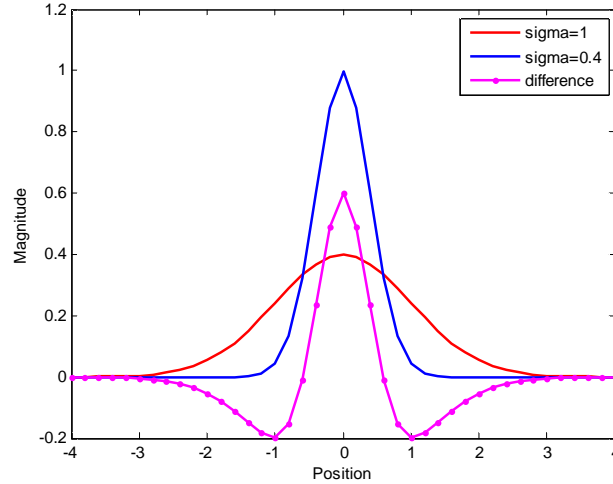


Figure 5-4: Distribution of Gaussian filters with two different sigma values and the resultant DoG filter in one dimension.

The Gaussian filter can be extended to a two dimensional space for images, as depicted in (5.5), by the product of two orthogonal Gaussians [29].

$$G_1(x, y) = \frac{1}{2\pi\sigma_1^2} e^{-\frac{x^2+y^2}{2\sigma_1^2}}. \quad (5.5)$$

$G_1(x, y)$ will form a matrix with x being the distance from the origin in the horizontal axis and y the distance from the origin in the vertical axis. Once again a filter window can be applied where $-x_w \leq x \leq x_w$ and $-y_w \leq y \leq y_w$. The net result will be a Gaussian filter matrix of size $(2x_w + 1, 2y_w + 1)$. To apply the Gaussian filter, with a specific width σ and window w , to an image P_i , the convolution is used as below:

$$P_{iG_1} = G_1(x, y) * P_i(x, y). \quad (5.6)$$

The net result is a blurred image as depicted in Figure 5-5(b) and (c). The Difference of Gaussian (DoG) is an approach that can be used to increase the visibility of edges and other details present in the image. It uses the band pass filter property of the Gaussian filter to remove the high frequency detail of the image which often contains noise and also some low frequency components representing the homogeneous areas in the image.

The algorithm involves the subtraction of one blurred version of the image from another blurred version. This can be visualised in Figure 5-5(d). The blurring effect can be modified by choosing different σ values for the Gaussian filter. As can be seen from Figure 5-4, the resultant DoG filter is a band-pass filter that will preserve spatial information that lies between

the ranges of frequencies from the two blurred images. In essence, only a small amount of spatial frequencies, that are present in the original greyscale image, will be kept.

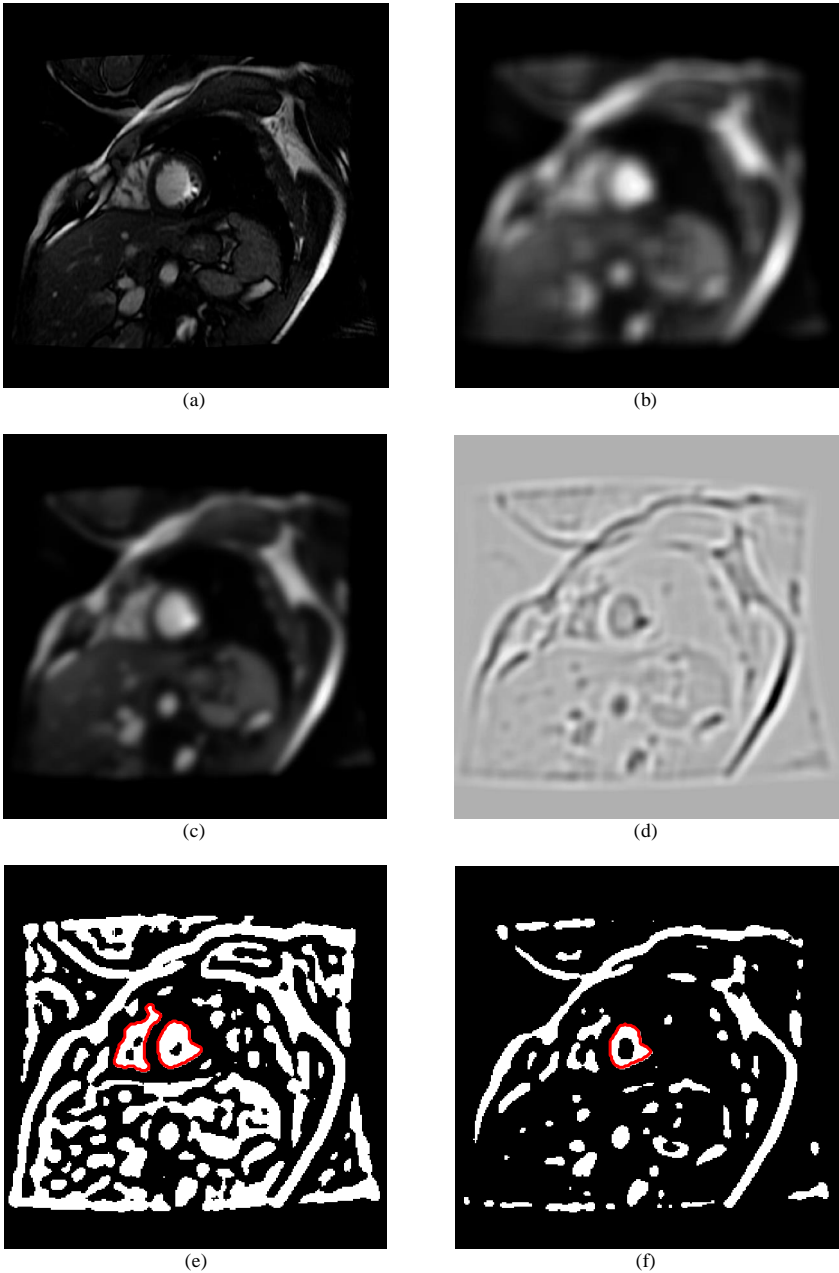


Figure 5-5: Application of DoG algorithm on a two dimensional cardiac MRI in the short axis view. (a) Original MRI image. (b) Gaussian filter applied with a high sigma value. (c) Gaussian filter applied with a low sigma value. (d) DoG filter applied with sigma values used in (b) and (c). (e) Application of small threshold value on (d). Red contours segment both the right and left ventricle (f) Application of large threshold value on (d). Red contour segments on the left ventricle.

In order for the DoG method to be used as an edge detector, a threshold, t , must be applied to the resultant DoG image in order to keep strong zero-crossings (large difference between the positive maximum and the negative minimum). Figure 5-5(e) and (f) depict two such threshold

application, with the former being a much lower threshold value. From the application of the threshold, ventricle segmentation can be performed which is also shown in these images by the red contour lines. In Figure 5-5(f), it can be seen that due to the high threshold value, portions of the right ventricle have been omitted. Thus, for ventricle segmentation per MRI slice, the optimum filter width σ , window w and threshold t , must be chosen.

The region of interest and subsequent pixel statistics measures are computed per image slice as described in Section 5.3.1.3 and Section 5.3.1.4.1 above. From experimentation on a large number of datasets obtained from different sources, the optimal DoG parameters are obtained as follows:

- i) The window (w) must be a matrix whose rows and columns must be of equal width. The number of pixels enclosing the region of interest is computed. The choice of w is calculated as follows:

$$w_s = \left\| \frac{1}{5} \sqrt{\sum_c ROI_s[c]} \right\|. \quad (5.7)$$

This will ensure that almost the entire Gaussian bell curve is taken into account and the filter will decay to nearly zero at the edges of the curve, so that no discontinuities is present in the image. As the window size decreases, smaller image features are detected.

- ii) The filter width (σ_{1_s} and σ_{2_s}) are chosen from the grey level co-occurrence matrix for slice s . σ_{1_s} is the column number that contains the most number of occurrences and σ_{2_s} is the right most column number of occurrences greater than 50. In essence the spread of the DoG is dependent on the spread of the pixels within the region of interest. The effect of choosing the filter width values are shown graphically in Figure 5-6. A small difference in σ_{1_s} and σ_{2_s} results in less feature points being selected as it considers points that separate areas of high pixel intensity difference. This produces difficulty in creating the segmentation contour. The optimum selection of σ_{1_s} and σ_{2_s} is depicted in Figure 5-6 (d), where more feature points are included due to the increased filter band and thus the segmentation contour of both the left and right ventricle can easily be created. Increasing the filter width difference too much could lead to non-detection of smaller features as more points of similar texture are included. This is shown in Figure 5-6 (e), where the papillary muscles are not detected (red arrows).
- iii) The threshold (t_s) is chosen to be 60% of the value of the mean intensity for region of interest, ROI_s . This will ensure that the strongest features or edges are kept in the filtered image which results from areas large intensity differences. The effect is shown in Figure 5-5(e) and (f).

The resultant MRI image is then converted to a binary image, resulting from the application of the threshold (t_s). The segmentation contours of the left and right ventricle can be automatically drawn by focussing on the region of interest and tracing the areas of the binary image.

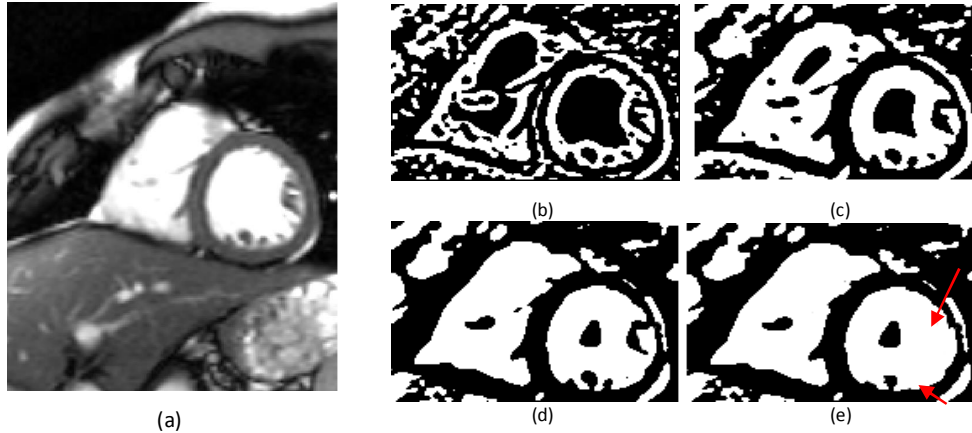


Figure 5-6: Effect of adjusting the filter width values σ_{1s} and σ_{2s} .

(a) Original MRI image. (b) Small difference in value between the two filter widths.
(c) Increase in value between the two filter widths. (d) Optimum filter widths as chosen by proposed algorithm.
(e) Large difference in value between the filter widths.

5.4 Automatic Cardiac MRI Segmentation Using Multiple Views

Researchers on cardiac MRI segmentation algorithms have focussed their efforts in the SAV as the left and right ventricles are visible on the same image and there is a clear separation between both. Furthermore, in routine cardiac MRI acquisition, only one slice is imaged in the two chamber view (2CV) and one in the four chamber view (4CV), which is used for patient positioning purposes. Another problem in the 2CV and 4CV is that there is overlapping pixel intensity and contrast between the ventricle and the atrium, which leads to segmentation complexity as can be seen in Figure 5-7.

Volumetric imaging is the acquisition of MRI data from a volume rather than a single slice. In clinical practice, image acquisition is performed in two parts, with the first being to determine the general position of the heart and the second for volumetric images. The volumetric images are obtained in three views namely, short axis view, two chamber view and four chamber view. By choosing the gradient axes, one set of image view slices can be selected from another set of image view slices. Hence all these three views are linked to an orthogonal co-ordinate system as described in Section 2.2 and Section 2.3 .

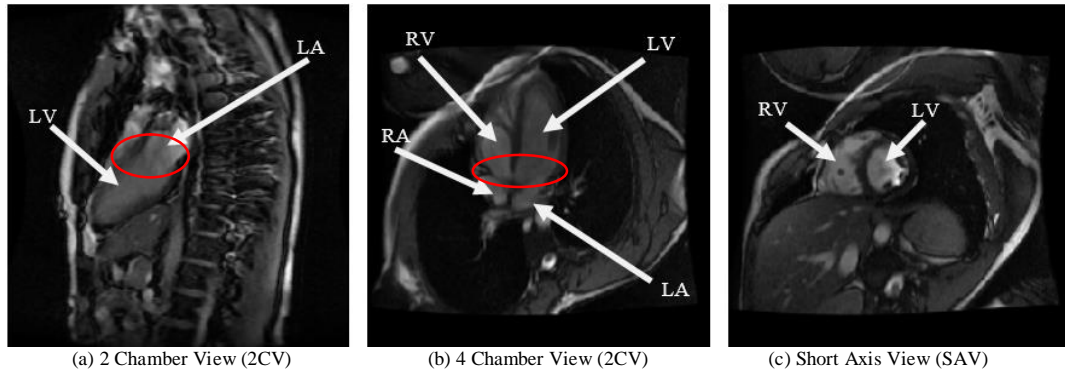


Figure 5-7: Examples of MRIs obtained on different views depicting the cardiac chambers namely Left Ventricle (LV), Left Atrium (LA), Right Ventricle (RV) and Right Atrium (RA). The red circles highlights the minimal difference in pixel intensities from ventricle to atrium

Figure 5-7 depicts samples of the images obtained in each view. The SAV is obtained by taking slices perpendicular to the long-axis as shown in Figure 5-8. In this view the left and the right ventricles are clearly visible between the apex slice to the base slice. From the base slice onwards, the atria appear in the images. The 2CV is obtained for the left and right side of the heart with the combination of ventricle and atrium. The 4CV is obtained from a gradient parallel to the long-axis (Figure 5-8). In this view all four chambers are visible. From experimental data, the ventricles can be clearly seen in approximately 10 slices in the SAV, 6 slices in the 2CV and 8 slices in the 4CV, depending on the slice thicknesses selected and the size of the patient's heart.

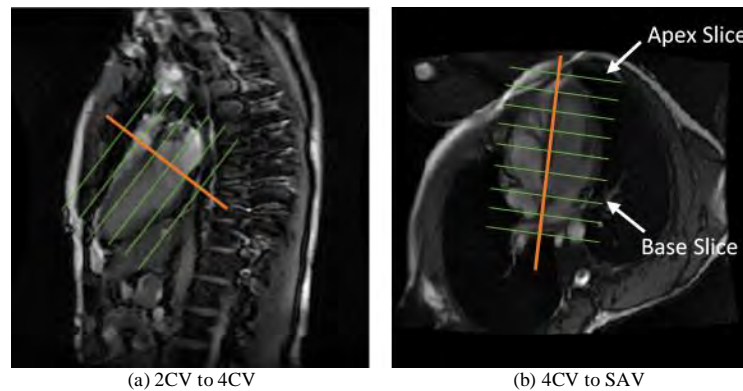


Figure 5-8: Positioning of MRI slices to obtain different MRI views

5.4.1 Segmentation by Projection

The cardiac MRIs obtained for a patient P consist of a series of N two dimensional images, P_i and is denoted as per equation (5.1). The DICOM [7] information per P_i will contain information about the image and patient orientation. If an object O_j in the image P_i has been segmented (for example the left ventricle), the resultant delineation by M landmark points is represented as:

$$S_{P_{O_j}} = \{(x_{1,P_{O_j}}, y_{1,P_{O_j}}), (x_{2,P_{O_j}}, y_{2,P_{O_j}}), \dots, (x_{M,P_{O_j}}, y_{M,P_{O_j}})\}. \quad (5.8)$$

Since all MRI views are linked to a common coordinate system called the patient coordinate system [8], each landmark point $(x_{q,P_{O_j}}, y_{q,P_{O_j}})$ in (5.8) can be translated to $(x_{qT,P_{O_j}}, y_{qT,P_{O_j}}, z_{qT,P_{O_j}})$ as shown in (5.9), where each variable is described in Table 5-1, which is extracted from Table 2-2.

$$\begin{bmatrix} x_{qT,P_{O_j}} \\ y_{qT,P_{O_j}} \\ z_{qT,P_{O_j}} \end{bmatrix} = \begin{bmatrix} xxdi_{P_i} & yxdj_{P_i} & sx_{P_i} \\ xydi_{P_i} & yydj_{P_i} & sy_{P_i} \\ xzdi_{P_i} & xz dj_{P_i} & sz_{P_i} \end{bmatrix} \begin{bmatrix} x_{q,P_{O_j}} \times PSi_{P_i} \\ y_{q,P_{O_j}} \times PSj_{P_i} \\ 1 \end{bmatrix}. \quad (5.9)$$

Table 5-1: Variable definition for translation to patient coordinate system for each image P_i [7]. The example value column is from a typical patient for translation from SAV.

Parameter Name	Variable	Example value	Parameter Description
Image Position	sx	-4.9091	x co-ordinate in patient co-ordinate system.
	sy	-253.0448	y co-ordinate in patient co-ordinate system
	sz	-1.7645	z co-ordinate in patient co-ordinate system
Image Orientation	xxdi	0.8306	Direction of cosine of row x to x in patient
	xydi	0.5556	Direction of cosine of row x to y in patient
	xzdi	0.0389	Direction of cosine of row x to z in patient
	yxdj	-0.3478	Direction of cosine of row y to x in patient
	yydj	0.5718	Direction of cosine of row y to y in patient
	yzdj	-0.7430	Direction of cosine of row y to z in patient
Pixel Spacing	PSi	1.3672	Physical distance between x points in image.
	PSj	1.3672	Physical distance between y points in image.

Note: The above table parameters are obtained from the DICOM information per image.

Hence (5.8) can be represented in the three dimensional patient coordinate systems as:

$$S_{P_{O,T}} = \{(x_{1T,P_{O_j}}, y_{1T,P_{O_j}}, z_{1T,P_{O_j}}), \dots, (x_{MT,P_{O_j}}, y_{MT,P_{O_j}}, z_{MT,P_{O_j}})\}. \quad (5.10)$$

Let us suppose that we are presented with 10 MRIs from the SAV and 5 MRIs from the 2CV. Using the existing segmentation methodologies described in Chapter 4, we can achieve approximate segmentation of the left ventricle in these MRIs, which will be represented as follows:

$$S_{SA,2CV,LV} = \{S_{P_{O_j}}\}: 1 \leq i \leq 15, j = 1. \quad (5.11)$$

Translating all these segmentation points to the patient coordinate system will result in:

$$S_{SA,2CV,LV,T} = \{S_{P_{O,T}}\}: 1 \leq i \leq 16, j = 1. \quad (5.12)$$

Given the q^{th} MRI in the 4CV, P_{4CV_q} , where $P_{4CV_q} \in P$, automatic segmentation of the ventricle can be performed on this MRI by initially translating the entire MRI slice into the patient coordinate system by applying (5.9) to each point (x_k, y_l) of P_{4CV_q} . This will result in P_{4CV_qT} .

Finding the intersecting points of this translated 4CV MRI with all the translated segmentation points from the SAV and 2CV, will create a segmentation region of interest in the 4CV MRI as per:

$$S_{4CV_q, LV, T} = S_{SA, 2CV, LV, T} \cap P_{4CV_q, T}. \tag{5.13}$$

This is depicted graphically in Figure 5-9 and Figure 5-10.

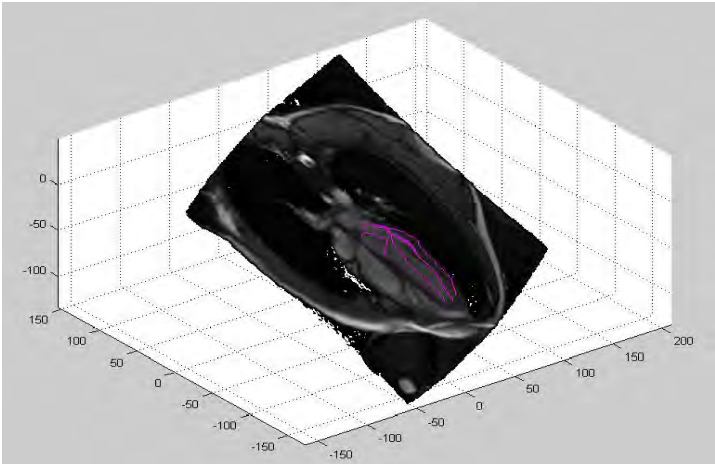


Figure 5-9: 2 chamber view segmentation contours (magenta) of left ventricle translated to an image in 4CV in patient co-ordinate system

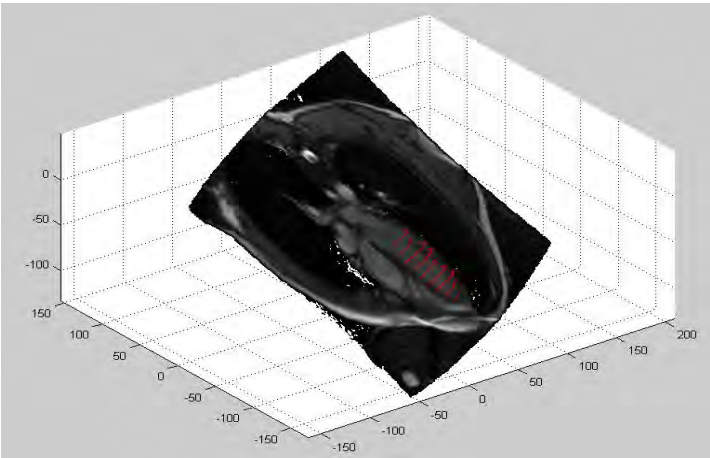


Figure 5-10: Short axis segmentation contours (red) of left ventricle translated to an image in 4CV in patient co-ordinate system.

It can be shown that the matrix in (5.9) is invertible, as the determinant will not be zero, and thus each intersecting point $(x_{fT, P_{4CV_q}, O_1}, y_{fT, P_{4CV_q}, O_1}, z_{fT, P_{4CV_q}, O_1})$ of $S_{4CV_q, LV, T}$ can be translated back onto the original MRI 4CV as follows:

$$\begin{bmatrix} x_{r,P_{4CV_q}O_1} \\ y_{r,P_{4CV_q}O_1} \\ z_{r,P_{4CV_q}O_1} \end{bmatrix} = \begin{bmatrix} xxdi_{P_{4CV_q}} & yxdj_{P_{4CV_q}} & sx_{P_{4CV_q}} \\ xydi_{P_{4CV_q}} & yydj_{P_{4CV_q}} & sy_{P_{4CV_q}} \\ xzdi_{P_{4CV_q}} & xzdj_{P_{4CV_q}} & sz_{P_{4CV_q}} \end{bmatrix}^{-1} \begin{bmatrix} x_{rT,P_{4CV_q}O_1} \\ y_{rT,P_{4CV_q}O_1} \\ z_{rT,P_{4CV_q}O_1} \end{bmatrix} \cdot \begin{bmatrix} PSi_{P_{4CV_q}} \\ PSj_{P_{4CV_q}} \\ 1 \end{bmatrix}. \quad (5.14)$$

The resultant segmentation region of interest in the 4CV image, after applying (5.14) to $S_{4CV_q,LV,T}$, can now be represented by $S_{P_{4CV_q},OLV}$. A rectangular border can enclose the region of interest by finding the maximum and the minimum x and y coordinates in $S_{P_{4CV_q},OLV}$ (Figure 5-11). By using the DoG approach described in Section 5.3.1.4, the left ventricle in the P_{4CV_q} image can be automatically segmented by focusing within the rectangular region of interest. Thus the segmentation of the left ventricle on the q^{th} MRI at the f^{th} iteration in the 4CV will be represented as $S_{P_{4CV_q},OLV,f}$. Similarly by using all the respective 4CV images the entire left ventricle can be segmented.

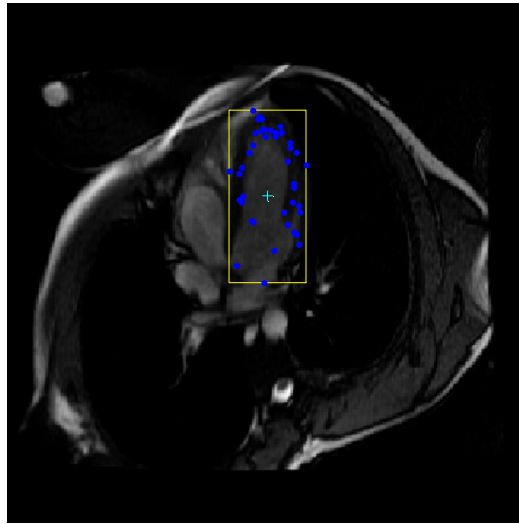


Figure 5-11: Region of interest for left ventricle segmentation in 4CV formed from intersecting points from SAV and 2CV segmentations.

The above method can be applied to other objects of interest such as the right ventricle. Furthermore, given segmentation of the ventricle in any two views, this methodology can be used to automatically segment the third view.

5.4.2 Achieving Convergence

The method described in Section 5.4.1 above is based on the assumption that approximate segmentation is available in two cardiac MRI views. This approximate segmentation can be improved by projecting the newly segmented view back onto that particular view. This process will continue to be iterative until a convergence is reached. The convergence measure used will

be both mathematical (distance based) and statistical (overlap based) by using the Hausdorff Distance and Dice Coefficient measures respectively. These measures are described in Section 3.1.1.6 and Section 3.1.1.7.

The aim of convergence is to minimise the Hausdorff Distance between the current segmentation in all three views to the previous segmentation from the respective MRI view and similarly maximise the degree of overlap between the current and previous segmentation. In essence, as depicted in (5.15), convergence is reached for ventricle segmentation on the q^{th} MRI at the f^{th} iteration in the 4CV if the Hausdorff distance is less than the threshold $Conv_H$ and Dice coefficient is greater than the threshold $Conv_D$. This convergence criterion can be applied to all MRI views.

$$\begin{aligned} Haus_{S_{P_{4CV_q}, O_{LV, f}}, S_{P_{4CV_q}, O_{LV, f-1}}} &\leq Conv_H \\ Dice_{S_{P_{4CV_q}, O_{LV, f}}, S_{P_{4CV_q}, O_{LV, f-1}}} &\geq Conv_D \end{aligned} \quad (5.15)$$

5.5 Summary

This chapter has presented a novel automatic segmentation method, whereby the segmentation of a ventricle in the third MRI view can be obtained from projecting the ventricle segmentations from two other views. The segmentation after the projection is provided by the difference of Gaussians edge detector in which the parameters for the filter were chosen by analysing the subsequent region of interest intensity profiles. If only a single cardiac MRI view is provided in the dataset to be segmented, the proposed algorithm reduces and finds the ventricle region of interest by analysing motion of the ventricle intensities throughout the cardiac cycle and thereby creating a standard deviation motion map. It can be concluded that in order for the DoG method to be used in efficient cardiac segmentation and algorithm is required to choose the parameters of the DoG filter optimally.

CHAPTER 6 - PERFORMANCE OF THE PROPOSED SEGMENTATION METHODS

This chapter is dedicated to assess the performance of the proposed MRI ventricle segmentation method that was presented in Chapter 5. The evaluation criteria used follows the mathematical, statistical and clinical measures that are described in Chapter 3. Due to limitations in the publically available datasets, discussed in Section 6.1 when it comes to the image acquisition and expert segmentation, a new dataset from the University of the Freestate is also utilised in the evaluation.

Section 6.1 will provide a description of the platform and testing method used in assessing the performance of proposed segmentation method. Section 6.2 and Section 6.3 will use the platform defined above and carry out different tests on the two proposed algorithms.

6.1 Experimental Method

It is of importance that in order to compare the complexity of different segmentation algorithms, they must be computed on similar platforms. Hence all results, for the proposed methods were obtained on an Intel® Core i5, 2.5 GHz PC platform. This system was equipped with 4 Gigabyte of RAM, running the Windows 7 64 bit operating system. The results of the proposed segmentation algorithms on different cardiac MRI datasets were executed from within the Matlab environment.

Section 3.1.1.5 recommends the usage of the publically available datasets in order to assess the performance of any newly developed segmentation algorithm. However, these datasets have several problems as described below:

- i) MRI contained in the dataset is from the SAV only.
- ii) Representation of ground truth via expert manual segmentation required the segmentation contours to be smooth.
- iii) Representation of ground truth enclosed papillary muscles and trabeculae within the segmented region.
- iv) Left and right ventricle segmentation contours are not from the same set of MRIs.

- v) Approximately 5.7% of the state of the art methods presented in Chapter 4 utilise these datasets for presentation of their results.

As a result of the issues stated above with regards to publically available datasets, a dataset from the Universitas Hospital (University of the Free State) was used to evaluate the accuracy of the proposed segmentation algorithm. The dataset consisted of five male patients and five female patients with no cardiac abnormalities. Full 2CV and 4CV imaging were also performed in obtaining this dataset. Each image is of size 256x256 pixels, 20 images per cardiac cycle and a slice thickness of 9mm. The dataset also consisted of expert manual delineation of the left ventricle and right ventricle in the SAV, 2CV and 4CV at the end diastole and end systole cardiac phases. Initially, from the given dataset, all images from SAV, 2CV and 4CV for a particular patient were identified at the end diastole and end systole cardiac times. A set of rules was defined in performing the expert manual delineation of these images [1], so that the segmentation contours could be as close to the anatomy as possible. As a result, papillary muscles were excluded from the segmentation region.

To assess the performance of the proposed method of ventricle segmentation, the mathematical and statistical measures described in Section 3.1.1.6 and Section 3.1.1.7 respectively will be used. More specifically, it will include the Hausdorff Distance and Dice coefficient metrics. The clinical based measure of comparing left and right ventricle volumes (Section 3.2.1.1) using Simpsons rule will also be calculated.

Finally, to test the robustness of a segmentation algorithm it is proposed that a series of images, from any of the cardiac MRI datasets described above be chosen, and various noise and motion effects be added to the images. These effects will be created by image based filters that will attempt to simulate noise and patient movement which is currently present on some MRI acquisitions. The filters to use are described below and depicted visually in Figure 6-1:

- i) Gaussian white noise with constant mean and variance,
- ii) Speckle noise which adds multiplicative noise to the image, P_i , using the equation $P_{i, speckle} = P_i + n * P_i$, where n is uniformly distributed random noise with zero mean and variance.
- iii) Point-spread function which simulates a blurred image to represent patient motion. The filter corresponds to the linear motion across 15 pixels at an angle of 5 degrees. To simulate the blur, the filter is convolved with the image P_i .

Segmentation of the ventricles in each of these filtered images will be performed and compared against the representation of the ground truth for the original image.

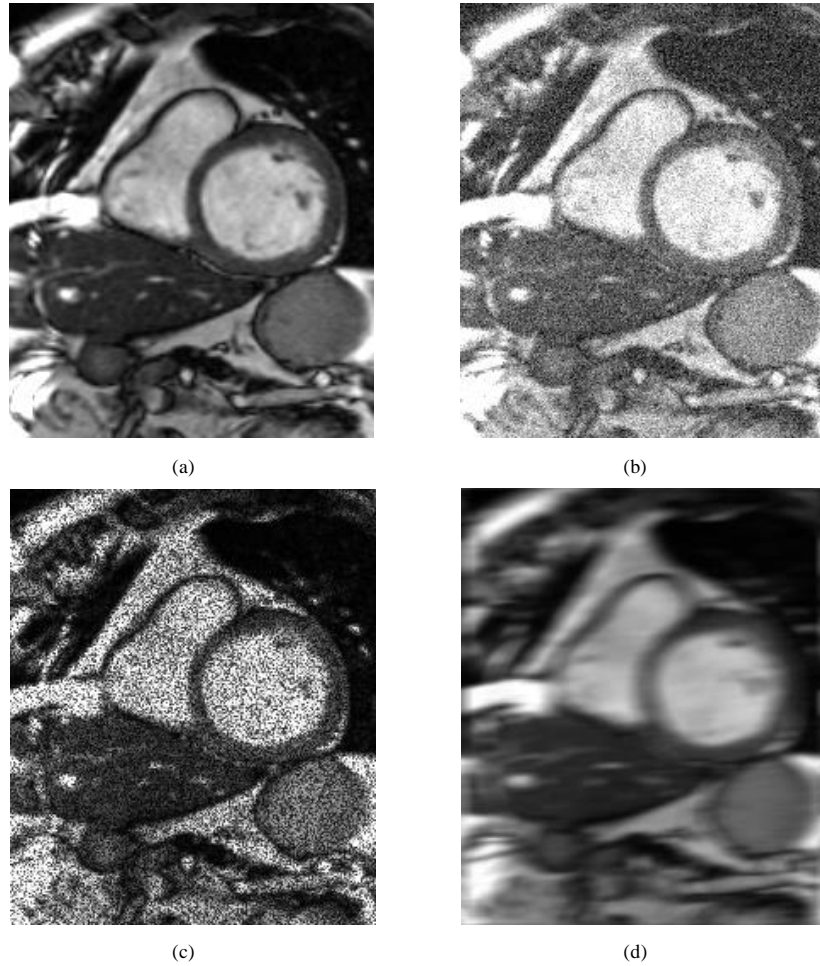


Figure 6-1: Various image filters applied to MRI to simulate noise and patient movement. (a) Original MRI. (b) Gaussian white noise applied to MRI. (c) Speckle noise filter applied to MRI. (d) Point-spread function which simulates a blurred image on MRI that represents patient motion.

6.2 Results for Application of Proposed Method on MRI Datasets in Short Axis View

The proposed segmentation algorithm was tested on three datasets namely, the Sunnybrook Cardiac Data (SCD) [25], Right Ventricle Segmentation Challenge Data (RVSCD) [26] and the locally obtained dataset from Universitas Hospital. The patients with no cardiac abnormalities were chosen for the initial test set.

The proposed algorithm is applied to nine slices for each patient in each dataset in the SAV at the end diastole and end systole cardiac phases. These times were chosen as the expert manual segmentation or ground truth representation was available together with each dataset and

clinical quantification metrics could be computed after segmentation. To evaluate the segmentation, the Hausdorff distance and Dice coefficient were calculated for each segmentation by using the proposed segmentation method against the ground truth representation. Table 6-1 depicts the segmentation results on each dataset per MRI slice for a chosen patient or volunteer from that dataset. The distance and statistical measures are averaged for the end diastolic and end systolic MRI for that slice. Figure 6-2 and Figure 6-3 shows graphically the segmentation performed by the proposed algorithm on slices from the SCD and RVSCD datasets respectively for a particular patient.

Table 6-1: Accuracy measurements of proposed segmentation method per MRI slice in the short axis view using MRIs for a patient from three datasets.

Slice Number	Left Ventricle (SCD)		Right Ventricle (RVSCD)		Left Ventricle (UFS)		Right Ventricle (UFS)	
	Haus	Dice	Haus	Dice	Haus	Dice	Haus	Dice
1	4.8593	0.7915	4.7488	0.9063	4.4930	0.8765	3.5136	0.8892
2	4.2355	0.8266	4.3141	0.9159	3.3961	0.8963	3.1686	0.9095
3	3.8008	0.8329	3.6236	0.9206	2.9369	0.9095	2.8720	0.9270
4	3.6764	0.8430	3.4122	0.9206	2.7802	0.9095	2.6890	0.9352
5	3.6056	0.8568	3.3730	0.9352	2.1787	0.9206	2.4727	0.9501
6	4.3350	0.8568	3.5136	0.9418	2.1213	0.9352	2.3160	0.9569
7	5.5322	0.8451	3.4650	0.9486	2.6418	0.9418	2.5323	0.9420
8	5.7151	0.8162	3.4122	0.9501	3.1820	0.9418	3.0764	0.9150
9	5.9789	0.7619	4.9438	0.8874	3.3686	0.9176	3.4122	0.8953
Average	4.6376	0.8256	3.8674	0.9252	3.0110	0.9165	2.8948	0.9244
Deviation	± 1.34	± 0.06	± 1.08	± 0.04	± 1.48	± 0.04	± 0.62	± 0.04

Haus = Hausdorff Distance of proposed segmentation in comparison to expert delineation.
 Dice = Dice Coefficient of proposed segmentation in comparison to expert delineation.
 SCD = Sunnybrook Cardiac Data RVSCD = Right Ventricle Segmentation Challenge Data
 UFS = Universitas Hospital Data from University of the Free State

The results depicted in Table 6-1 and Table 6-2 illustrate the ability of the proposed segmentation algorithm to provide an accurate segmentation over a variety of datasets. The segmentation accuracy on the right ventricle shows an average pixel-wise distance of less than 4 and an overlap of approximately 92%±2% over all slices from different datasets. The results for the SCD dataset show a slight reduction in segmentation accuracy as compared to the UFS dataset. This is due to the proposed segmentation algorithm not including papillary muscles whereas the representation of the ground truth in the SCD does. The results from Table 6-1 also depict the general observation that slices close to the apex and base of the ventricles in the short axis view are difficult to segment with a high accuracy, due to the close proximity of other features and partial volume effects due to the relatively thick slices. It can also be seen from Figure 6-3, as indicated by the red arrow, that the segmentation of the proposed method does not perform well at the bottom left of the right ventricle due to similar intensity profiles. Thus if more information is provided, from other views (Section 5.4.1), then the segmentation contour will be refined to not include that region and be closer to the expert manual delineated contour.

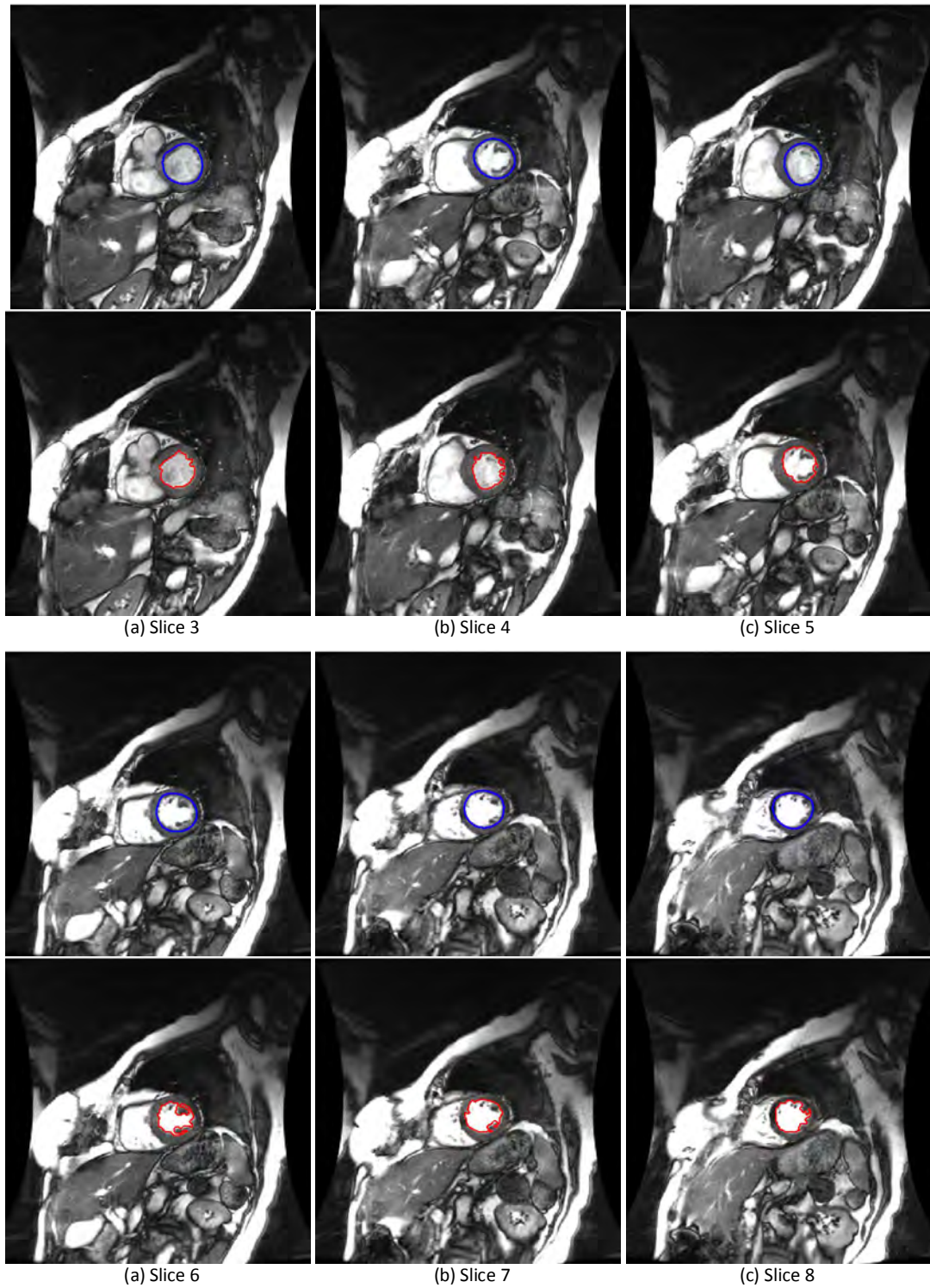


Figure 6-2: Segmentation of left ventricle in the SAV performed by expert manual delineation (blue contours) and proposed algorithm (red contours) for multiple slices from a patient in the SCD dataset.

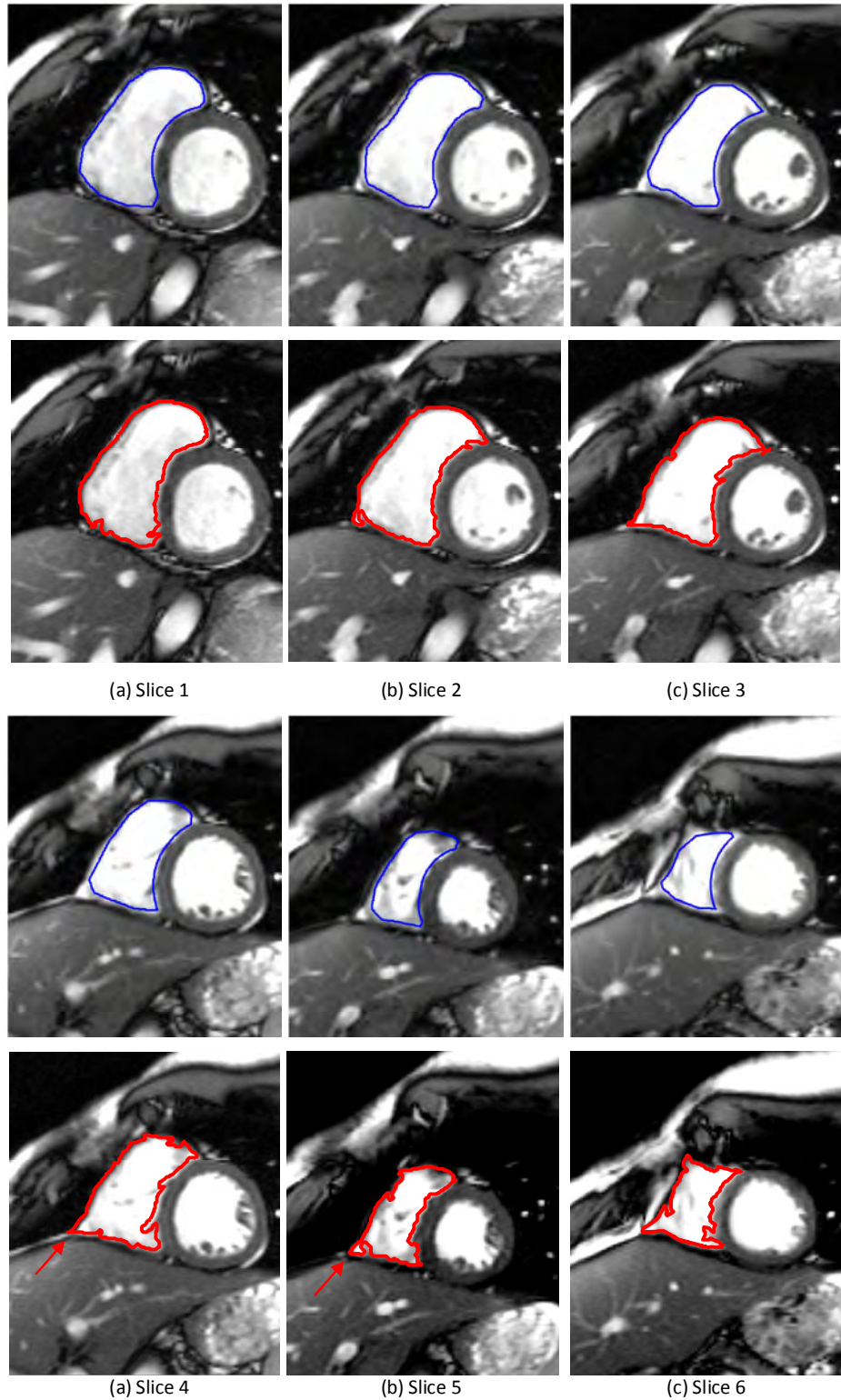


Figure 6-3: Segmentation of right ventricle in the SAV performed by expert manual delineation (blue contours) and proposed algorithm (red contours) for multiple slices from a patient in the RVSCD dataset. The red arrows shows the portion of the ventricle that the proposed method does not perform well in.

As expected, the standard deviation motion maps were different per slice per dataset and hence the DoG parameters per MRI slice was different, yielding a better accuracy. The window size varied from the apex to about the fourth slice, due to the size of the ventricle increasing. The intensity profile across different datasets varied, hence the filter width (σ_{1s} and σ_{2s}) varied according to the grey level co-occurrence matrix. The results showed an average σ_{1s} of 5 ± 3 and σ_{2s} of 2 ± 2 . The mean intensity for region of interest varied by approximately 30, which resulted in a respective threshold deviation of ± 18 .

To remove the comparison to the ground truth representation, several clinical measures were calculated on both the left and right ventricle segmentation as shown in Table 6-2 for three patients. These measures included end systolic volume, end diastolic volume, stroke volume and ejection fraction. The stroke volume error between the left and right ventricle is thus calculated. It must be noted that even though the SCD did not contain contours for the right ventricle, the right ventricle was still segmented using the proposed segmentation method. The same applies for the RVSCD, where the left ventricle was also segmented.

Table 6-2: Volumetric measurement of proposed segmentation method in the short axis view for three patients from different datasets

Volunteer Dataset		EDV (ml)	ESV (ml)	SV (ml)	EF (%)	SV Error (%)
SCD	LV	119.2	37.8	81.4	68.3	8.4
	RV	125.3	43.4	74.6	59.5	
UFS	LV	66.5	20.2	46.3	69.6	3.7
	RV	76.7	32.1	44.6	58.1	
RVSCD	LV	77.8	27.5	50.3	64.7	6.9
	RV	97.2	43.4	53.8	55.3	

The stroke volume error over all patients is less than 10%, averaging approximately $6\pm 2.5\%$. The errors can be attributed to the small segmentation errors (SCD and RVSCD datasets) as well as the voxel error from Simpsons Rule, which is due to the 9mm slice thickness.

To test the robustness of the proposed algorithm, a series of images for one patient at the end diastole and end systole phase, from the apex slice to the base slice, in the RVSCD and UFS dataset was chosen. Various noise and motion effects were added to these images. The resultant images to which the filters were applied in creating the effects and the respective segmentation contours are depicted visually in Figure 6-4. Table 6-3 provides the average Hausdorff and average Dice coefficients and deviation obtained over all segmented images from this series for both datasets.

Table 6-3: Accuracy measurements of proposed segmentation on distorted MRI in short axis view.

MRI Dataset	Average Haus	Haus Deviation	Average Dice	Dice Deviation
RVSCD	6.3620	0.5439	0.9245	0.0254
UFS	6.8620	0.1586	0.9045	0.0261

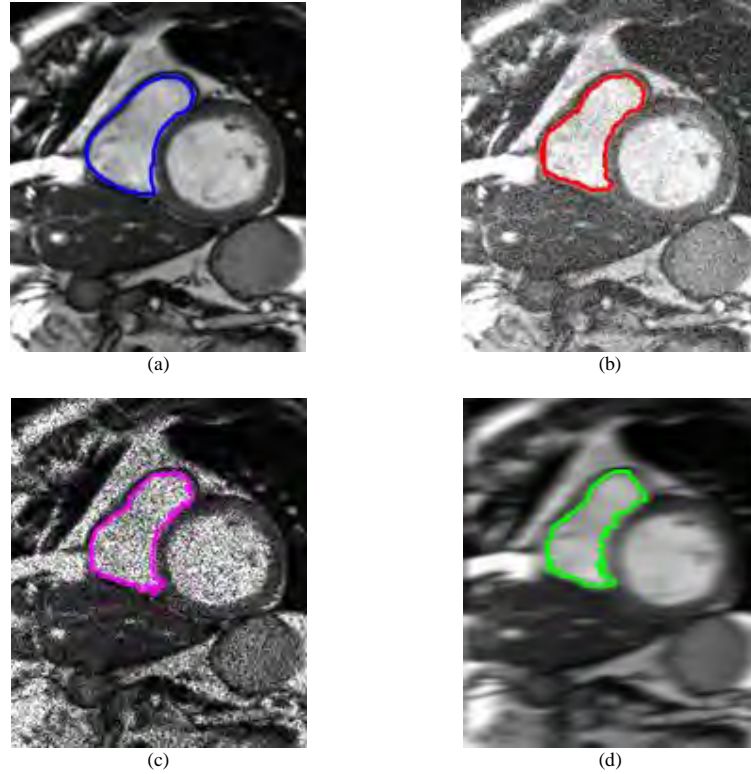


Figure 6-4: Segmentation performed by proposed algorithm for the right ventricle on images where noise and motion effects were introduced.

- (a) Original MRI in the short axis view with the blue contour depicting expert delineation of right ventricle.
- (b) Gaussian white noise applied to MRI from (a). Red contour is the segmentation achieved by algorithm.
- (c) Speckle noise filter applied to MRI from (a). Purple contour is the segmentation achieved by algorithm.
- (d) Point-spread function which simulates a blurred image on MRI from (a) that represents patient motion. Green contour is the segmentation achieved by the proposed algorithm

The robustness test results of Table 6-3 shows that the proposed algorithm still performs very well on images that have noise and motion effects. In comparison to the segmentation of Table 6-1 on the normal images, the robustness tests shows a deviation of less than 3 pixel distance in terms of the Hausdorff measure and less than 0.016 in terms of overlap using the Dice coefficient. Thus the proposed method can be used to accurately segment MRIs that contain patient movement as well as other artefacts which are created as a side effect of the MRI capture process.

For further in-depth analysis of the proposed segmentation method, the entire datasets of the SCD and RVSCD was tested. These will include cardiac MRIs from patients with cardiac problems and abnormalities. As discussed in Section 3.1.1.5.1, the SCD dataset contains MRI of 9 healthy patients, 12 having heart failure with infarction, 12 having heart failure without infarction and 12 having hypertrophy. The segmentation results of these patient MRIs are presented in Table 6-4, with the metrics averaged at the end diastole and end systole over all slices for patients with a particular cardiac abnormality. Thereafter the results for all patients is compared to the existing state of the art segmentation algorithms/methods discussed in Chapter 4, which is depicted in . Similarly Table 6-6, compares the segmentation results on the RVSCD dataset to other segmentation methods.

Table 6-4: Average Dice coefficient and Hausdorff distance of the proposed segmentation algorithm on the SCD dataset for patients with different pathologies.

	Normal	HF-NI	HF-I	HYP	All
Average Haus	3.0415	3.5125	3.3075	4.385	3.5613
Average Dice	0.8367	0.865	0.870	0.8175	0.8473

HF-NI=Heart failure with No infarction, HF-I= Heart failure with Infarction, HYP=Hypertrophy

Table 6-5: Comparison of Proposed segmentation algorithm with other segmentation methods on the SCD dataset for all patients with different pathologies.

	Proposed	Mahapatra et al. [99]	Mahapatra et al. [152]	Chittajallu et al. [153]	Ngo et al. [134]	Liu et al. [87]	Dreijer et al. [154]
Average Haus	3.56 ±1.2	3.3 ±0.5	1.8 ±0.4	2.2 ±0.3	2.08 ±0.46	2.3 ±0.36	1.84 ±0.32
Average Dice	0.85 ±0.07	0.85 ±0.09	0.91 ±0.11	0.88 ±0.07	0.90 ±0.04	0.89 ±0.04	0.91 ±0.04

Table 6-6: Comparison of Proposed segmentation algorithm with other segmentation methods on the RVSCD dataset for all patients with different pathologies.

	Proposed	Zuluaga et al. [144]	Ou et al. [145]	Maier et al. [100]	Bai et al. [146]	Grosgeorge et al. [98]
Average Haus	4.89 ± 1.67	10.51 ± 9.17	23.16 ± 19.86	11.15 ± 6.62	9.26 ± 4.93	9.97 ± 5.49
Average Dice	0.87 ± 0.09	0.55 ± 0.32	0.80 ± 0.19	0.78 ± 0.20	0.76 ± 0.20	0.78 ± 0.23

For the SCD dataset, the proposed segmentation algorithm does not perform as well as compared to the others. This is due to the proposed method excluding papillary muscles and trabeculae from the segmentation contour as depicted in Figure 6-2 and the resultant segmentation contour is not smooth. However, the deviation from the best performing method [154] is 1.72 in terms of the Hausdorff distance and 0.06 for the Dice coefficient on average

over all MRIs from the SCD dataset. The majority of the deviation comes from the segmentation of MRIs from patients with Hypertrophy as indicated in Table 6-4. This can be visualised in Figure 6-5, where the red arrow shows the area of the right ventricle in which the proposed method segmented as the left ventricle. This is due to the similar intensity profiles. Once again if more information was provided from segmentation from other MRI views, the region of interest created for the left ventricle will exclude that overlapping region.

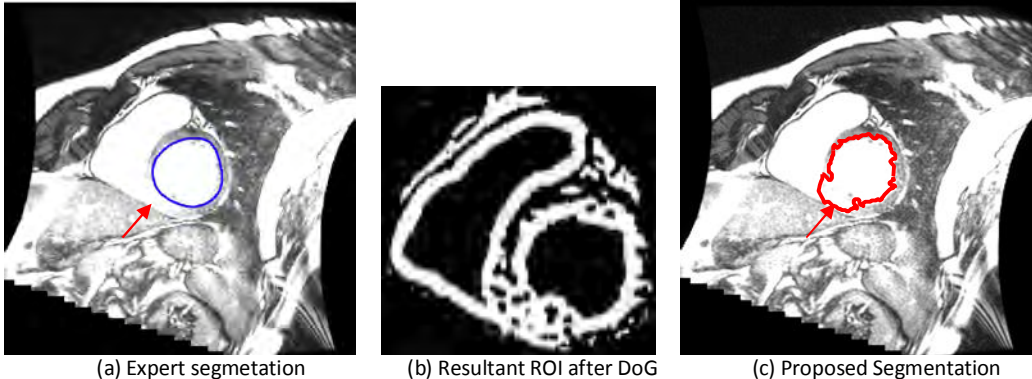


Figure 6-5: Segmentation of ventricle in the SAV performed by expert manual delineation (blue contour) and proposed algorithm (red contour) for a slice from a patient with Hypertrophy in the SCD dataset. The red arrow shows the portion of the ventricle that the proposed method does not perform well in.

6.3 Results for application of proposed method on MRI datasets that have three views

The publically available datasets, namely the Sunnybrook Cardiac Dataset (SCD) [11], Right Ventricle Segmentation Challenge Dataset (RVSCD) [12] and the York University Dataset (YUD) [13], cannot be used in the evaluation of the proposed segmentation algorithm as they contain only MRIs in the short axis view.

A dataset from the Universitas Hospital (University of the Free State - UFS) was used to evaluate the accuracy of the proposed segmentation algorithm. The dataset consisting of five male patients and five female patients with no cardiac abnormalities was chosen. The Hausdorff distance and Dice coefficient measures are used to compare the accuracy of the proposed segmentation algorithm to the expert manual delineation.

To provide the initial segmentation estimates, left and right ventricles in the SAV were segmented using Active Appearance Model (AAM), described in Section 4.3. The training set for the AAM was obtained from SCD and RVSCD. It must be noted that these training sets included papillary muscles as a part of the segmentation. The left and right ventricles in the

2CV were segmented using the proposed method in Section 5.3. User interaction was required to identify two points on the mitral valve, pulmonary valve and tricuspid valve that separates the ventricles from the atrium on each MRI slice at the end diastole and end systole cardiac phase. The results of the initial segmentation accuracy of the left ventricle of a patient in the SAV and 2CV are shown in Table 6-7 and Table 6-8 respectively in the columns Iteration 1. The Hausdorff distance and Dice coefficient are averaged for the resulting segmentation on the end diastole and end systole images per MRI slice.

The segmentation of the left and right ventricles of all slices in the 4CV was performed by applying the proposed algorithm using the initial segmentation in the SAV and 2CV. The results are depicted in Table 6-9 for the left ventricle. Iteration 2 results in the SAV were achieved by using the segmentations of the 2CV Iteration 1 and 4CV Iteration 1. Thereafter the Iteration 2 2CV segmentation was obtained by using the proposed algorithm on the segmentation of SAV Iteration 2 and 4CV Iteration 1.

Table 6-7: Accuracy measurements per iteration of proposed segmentation method on left ventricle per MRI slice in the short axis view at end diastolic cardiac phase.

LV / SAV Slice Number	Starting Set		Iteration 1		Iteration 2		Iteration 3	
	Haus	Dice	Haus	Dice	Haus	Dice	Haus	Dice
1	8.3958	0.8978	7.2111	0.6472	3.8079	0.8000	2.8284	0.8864
2	7.7471	0.9270	7.1589	0.7301	4.5000	0.7611	2.5495	0.9008
3	4.4216	0.9036	4.2426	0.7936	3.6401	0.8218	2.5495	0.8845
4	3.3243	0.9433	3.5355	0.9010	2.5000	0.9030	2.5000	0.9008
5	3.8544	0.9142	3.1623	0.8784	2.5495	0.9003	2.2361	0.9078
6	5.0643	0.8745	3.6056	0.8621	2.8284	0.8919	2.2361	0.9048
7	8.0654	0.8875	4.0311	0.8803	3.5000	0.8864	2.2361	0.8956
8	8.0082	0.8932	3.2016	0.8681	2.9155	0.8578	2.1213	0.8956
9	5.4301	0.8288	4.7434	0.8387	3.1623	0.8621	2.5000	0.8864
10	5.1021	0.8515	3.3541	0.8314	2.5000	0.8344	2.5000	0.8681

Haus = Hausdorff Distance of proposed segmentation in comparison to expert delineation.
Dice = Dice Coefficient of proposed segmentation in comparison to expert delineation.

Table 6-8: Accuracy measurements per iteration of proposed segmentation method on left ventricle per MRI slice in the 2 chamber view at end diastole cardiac phase

LV / 2CV Slice Number	Starting Set		Iteration 1		Iteration 2		Iteration 3	
	Haus	Dice	Haus	Dice	Haus	Dice	Haus	Dice
1	4.8811	0.7428	3.1623	0.8288	2.5495	0.8621	2.2361	0.8919
2	4.6165	0.9134	3.6401	0.9078	2.8284	0.9134	2.5495	0.9030
3	6.4284	0.9423	4.0311	0.9343	2.9155	0.9423	2.5000	0.9423
4	6.3876	0.9037	4.2426	0.9008	2.5495	0.9008	2.5000	0.9078
5	6.2867	0.8977	4.7434	0.9003	3.6056	0.8919	2.8284	0.9008

Table 6-9: Accuracy measurements per iteration of proposed segmentation method on left ventricle per MRI slice in the 4 chamber view at end diastole cardiac phase

LV / 4CV Slice Number	Iteration 1		Iteration 2		Iteration 3		Iteration 4	
	Haus	Dice	Haus	Dice	Haus	Dice	Haus	Dice
1	6.7082	0.5926	5.6569	0.6840	3.3541	0.8288	2.9155	0.8681
2	8.2462	0.8321	5.4301	0.8537	3.5000	0.8726	2.8284	0.8921
3	6.5277	0.8515	3.1623	0.9172	2.6926	0.9196	2.5000	0.9182
4	6.0000	0.8887	4.7434	0.8803	2.9155	0.8932	2.5495	0.9078
5	3.5000	0.8148	3.0000	0.8621	2.9155	0.8515	2.6401	0.8745

The convergence measures were chosen such that Hausdorff distance convergence, $Conv_H$, is 1.5 and the Dice Coefficient convergence, $Conv_D$, is 0.98. It was observed that on an average of the ten patients the convergence was achieved at the fourth iteration. The final accuracy measures at the fourth iteration are also displayed in Table 6-7, Table 6-8 and Table 6-9.

As a final test of accuracy of the proposed segmentation method, several clinical measures were calculated on both the left and right ventricle segmentation at Iteration 4. These measures included end systolic volume, end diastolic volume, stroke volume and ejection fraction as depicted in Table 6-10. The stroke volume error between the left and right ventricle is thus calculated.

Table 6-10: Volumetric measurement of proposed segmentation method in the three MRI views for a patient

MRI View		EDV (ml)	ESV (ml)	SV (ml)	EF (%)	SV Error (%)
SAV	LV	79.6	28.1	51.5	64.7	4.7
	RV	97.4	43.5	53.9	55.3	
2CV	LV	90.7	38.8	51.9	57.2	11.9
	RV	97.9	52.2	45.7	46.7	
4CV	LV	109.7	44.7	65	59.3	4.8
	RV	105.1	43.2	61.9	58.9	

From the results depicted in Table 6-7, Table 6-8 and Table 6-9, the segmentation accuracy increases per iteration. This can be visualised in Figure 6-6 and Figure 6-7. The accuracy can be attributed to the region of interest being refined per iteration and thus the Difference of Gaussian intensity model ignores points outside the region of interest. The volumetric measures of Table 6-10, provides further justification for the use of the proposed algorithm, showing an average stroke volume error of 7.1%.

An in depth analysis of the results also reveal the difficulty in performing segmentation at the ventricle ends, showing a decreased accuracy in comparison to the expert delineation. This is due to other artefacts being present, such as the valves, and also partial volume effect. Also to

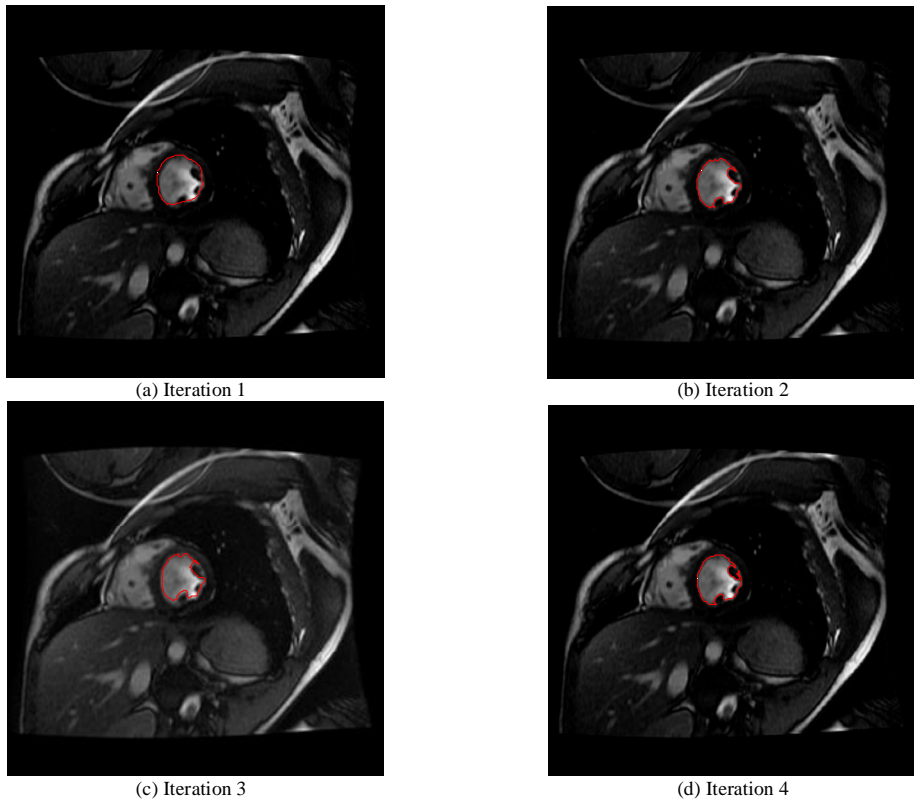


Figure 6-6: Segmentation per iteration of proposed method on left ventricle for slice 6 in the short axis view.

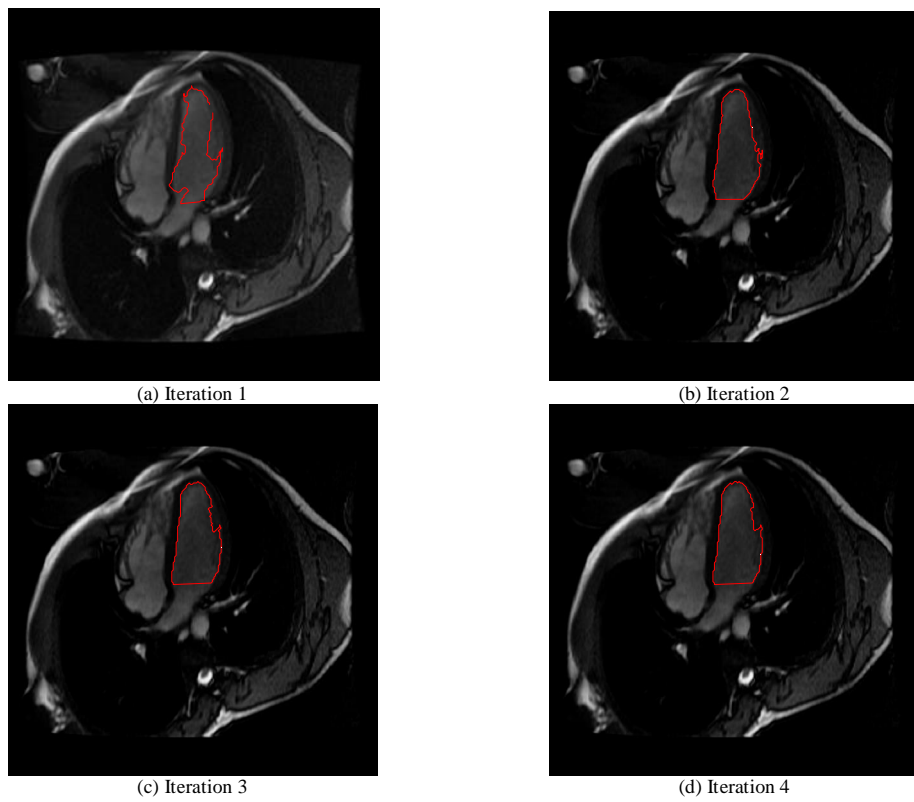


Figure 6-7: Segmentation per iteration of proposed method on left ventricle for slice 3 in the 4 chamber view.

be considered is the fact that experts also find difficulty in delineating the ventricles in these regions. However, the accuracy was still within a three pixel length and 85% overlap showing the ability of this algorithm to adapt to these effects. The other factor that played a negative role in the accuracy is the voxel error, which is due to the 9mm slice thickness. Figure 6-8 depicts visually the segmentation of the proposed algorithm in comparison to expert manual delineation in the SAV. The remaining figures, Figure 6-9, Figure 6-10, Figure 6-11, Figure 6-12 and Figure 6-13 shows the effect of the proposed algorithm segmenting the left and right ventricles in the SAV, 4CV and 2CV.

Although convergence of the algorithm is achieved on the fourth iteration, this is still a time consuming process as the translation from one plane to another is processing intensive. With the majority of the algorithm being automatically processed, the average time taken per ventricle segmentation is approximately fifteen minutes on the MATLAB simulation engine. Thus optimisation of the algorithm implementation is required if the clinical results, calculated from the proposed segmentation, are to be used in a real time diagnosis environment.

The proposed method was used to segment the left and right ventricles for all ten patients from the UFS dataset at the end diastole and end systole cardiac phases. Table 6-11 shows the average of the Hausdorff distance and Dice coefficient for all patients at both cardiac phases for each MRI view. These metrics fall within the acceptable level of the state-of-art measures from [1]. A final assessment of the effectiveness of this algorithm is done by comparing the results obtained on the SAV for multiple MRI views (Table 6-7) and single MRI view (Table 6-1). The Hausdorff distance and Dice coefficient at iteration 3 from Table 6-7 is 2.43 and 0.89 respectively and that of Table 6-1 is 3.01 and 0.92 respectively. It can therefore be concluded that by providing more information from other MRI views, the average distance of the points is much closer to the representation of the ground truth by 24% in this instance.

Table 6-11: Average Dice coefficient and Hausdorff distance of the proposed segmentation algorithm in all MRI

	SAV	2CV	4CV	All
Average Haus	2.2901	2.3105	2.5979	2.3995
Average Dice	0.9025	0.9213	0.9034	0.9090

views on the UFS dataset for all 10 patients.

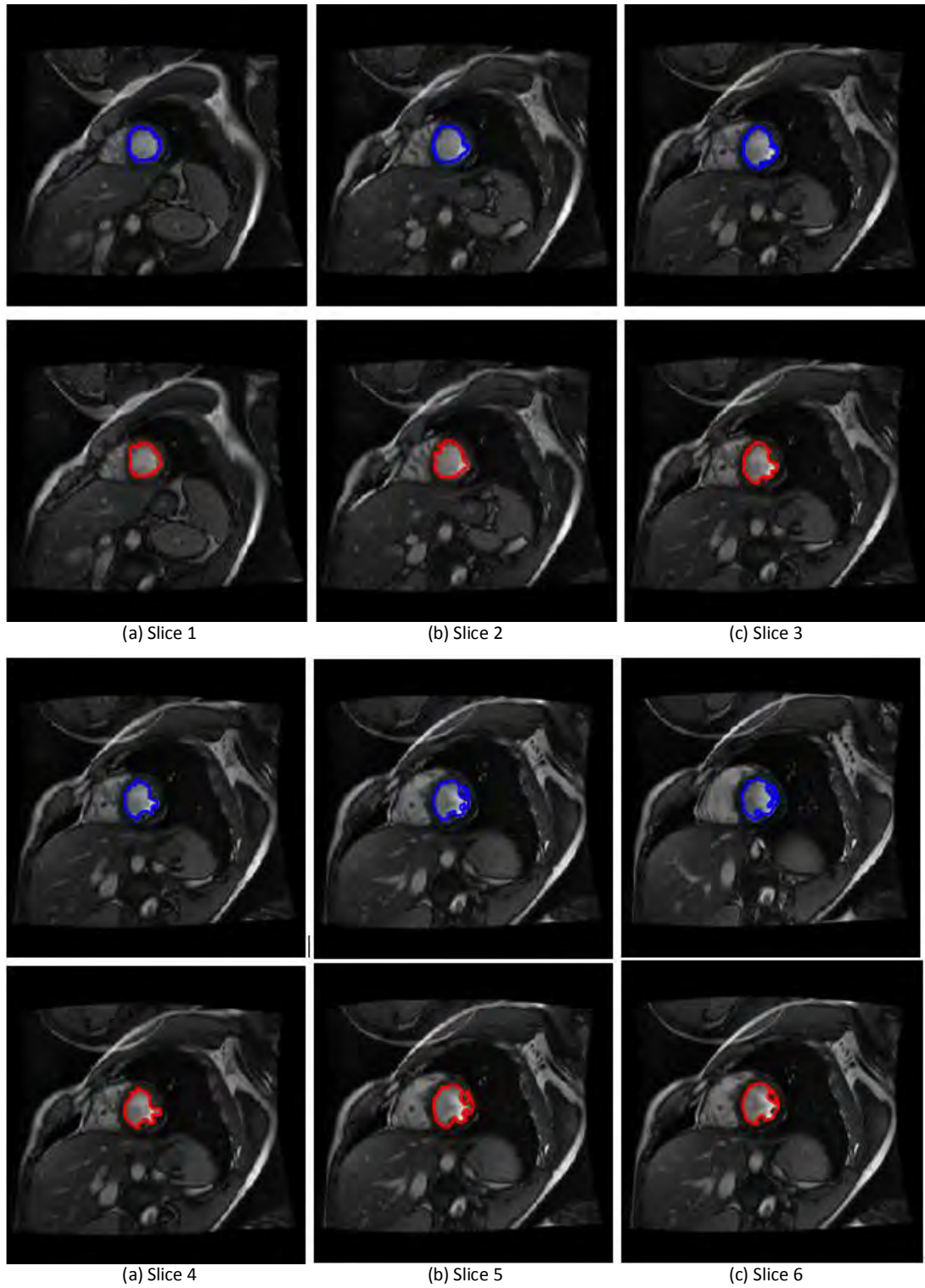


Figure 6-8: Segmentation of left ventricle in the SAV performed by expert manual delineation (blue contours) and proposed algorithm (red contours) for multiple slices from a patient in the UFS dataset.

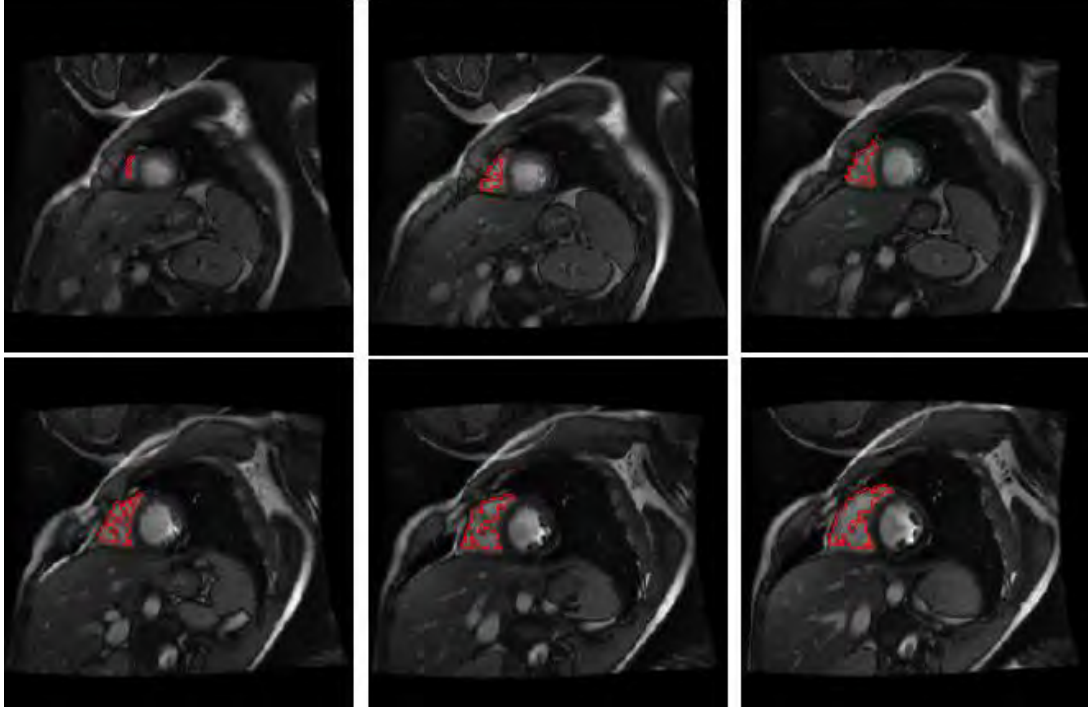


Figure 6-9: Segmentation of right ventricle in the SAV performed by proposed algorithm (red contours) for multiple slices from a patient in the UFS dataset.

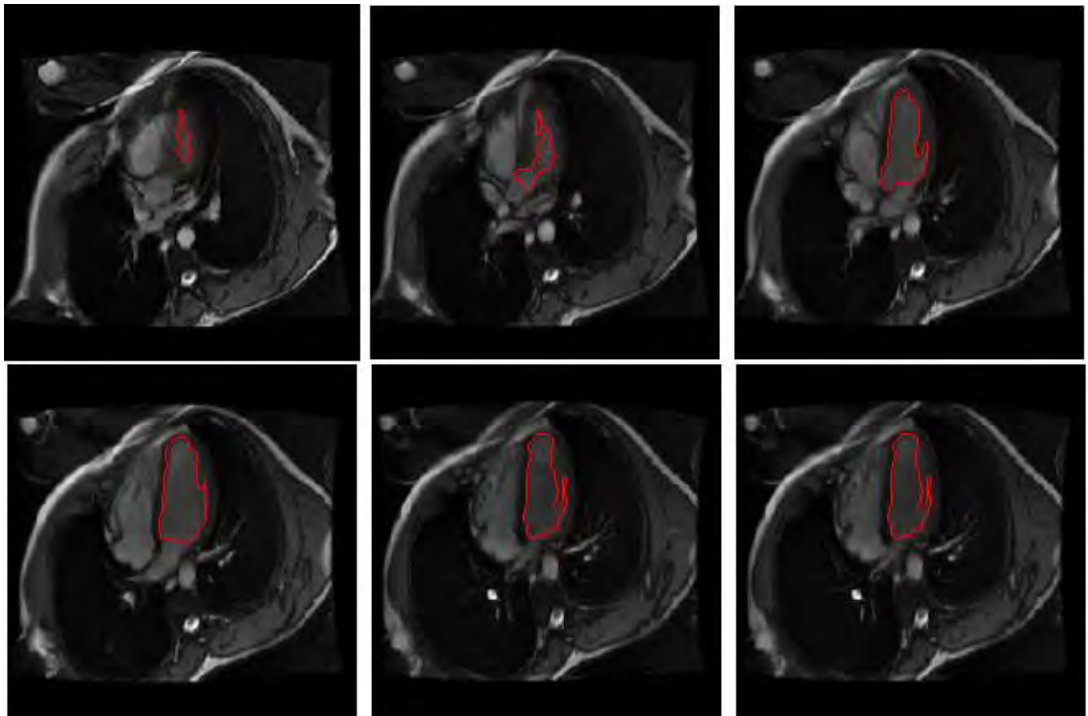


Figure 6-10: Segmentation of left ventricle in the 4CV performed by proposed algorithm (red contours) for multiple slices from a patient in the UFS dataset.

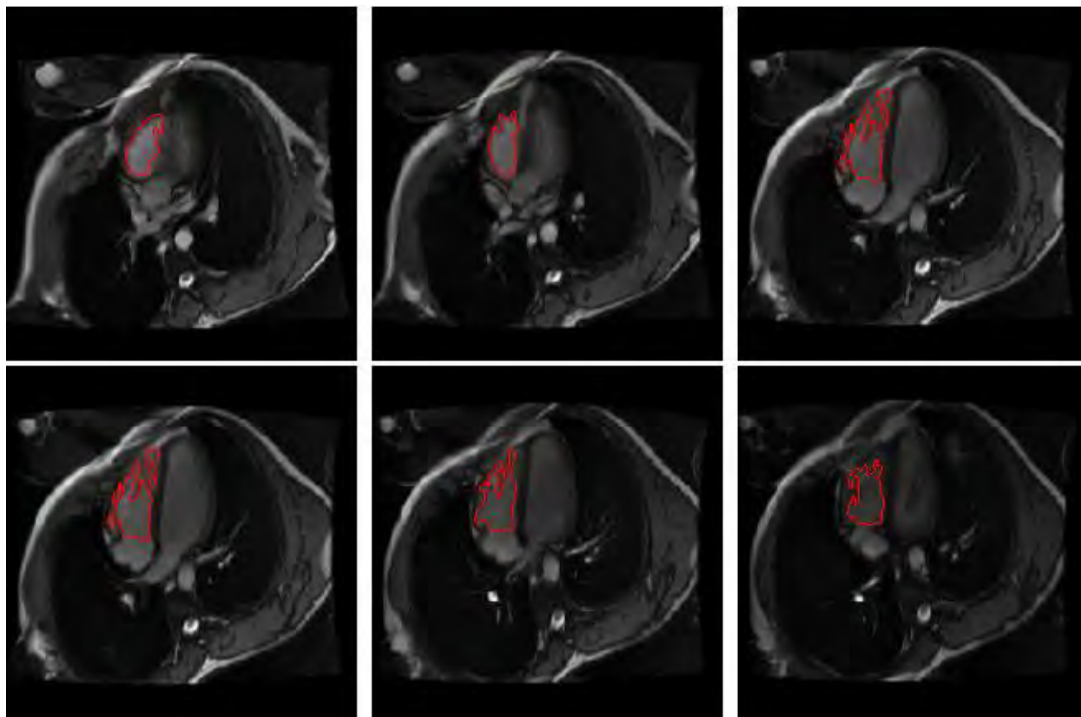


Figure 6-11: Segmentation of right ventricle in the 4CV performed by proposed algorithm (red contours) for multiple slices from a patient in the UFS dataset.

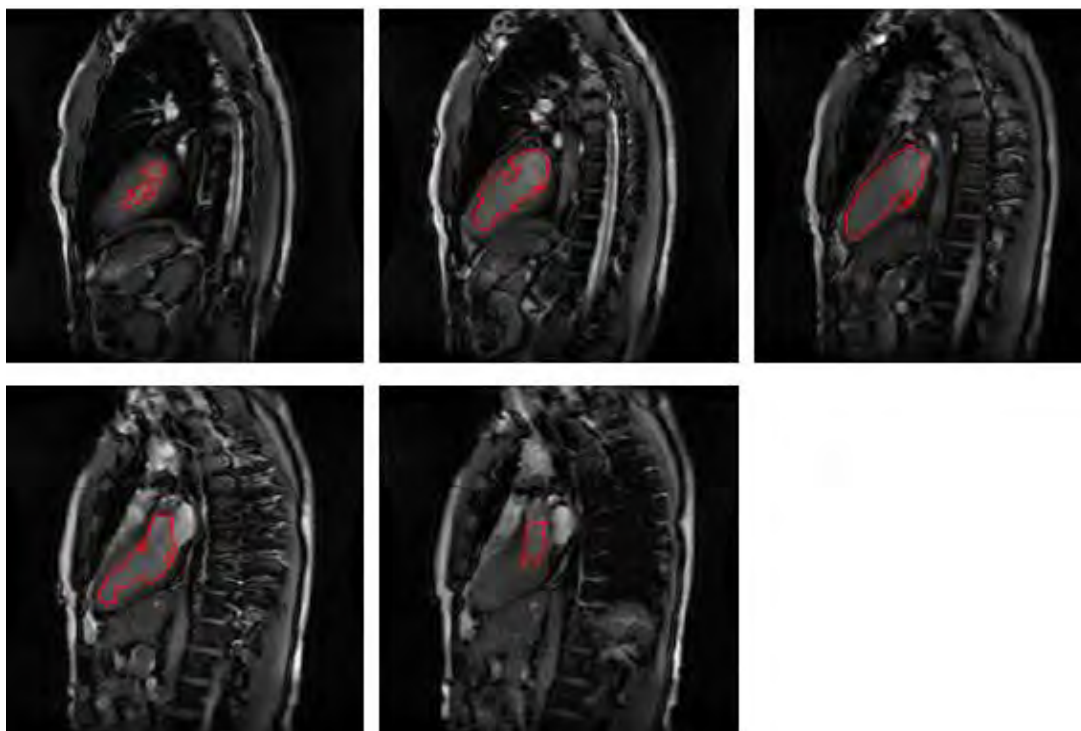


Figure 6-12: Segmentation of left ventricle in the 2CV performed by proposed algorithm (red contours) for multiple slices from a patient in the UFS dataset.

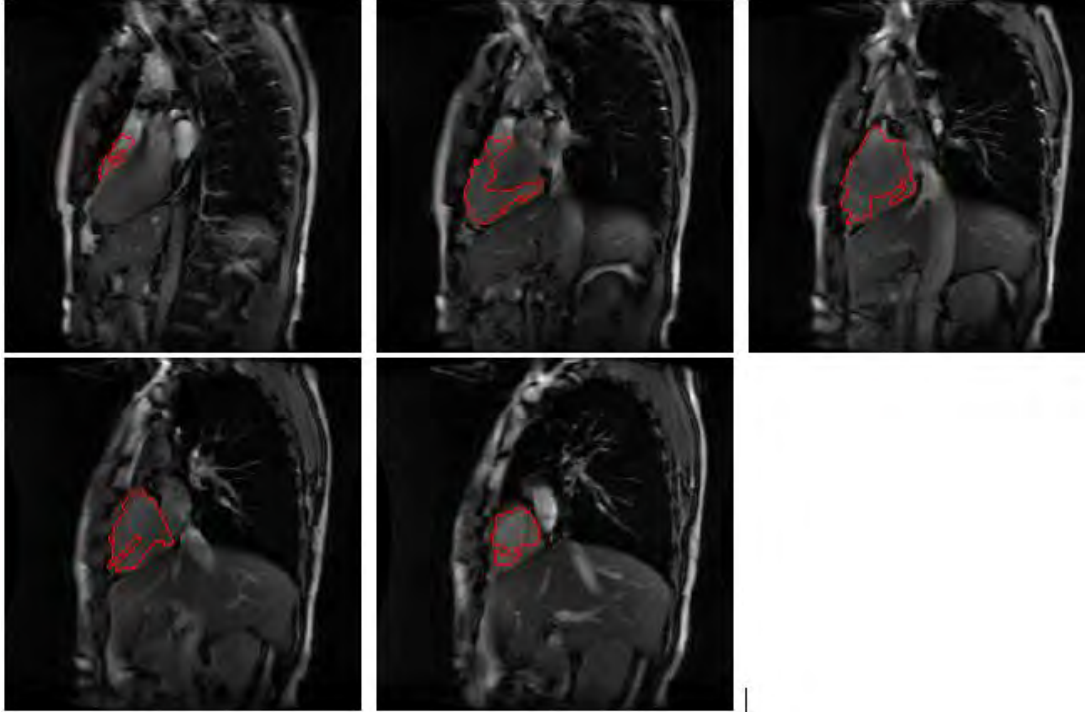


Figure 6-13: Segmentation of right ventricle in the 2CV performed by proposed algorithm (red contours) for multiple slices from a patient in the UFS dataset.

6.4 Summary

This chapter has provided details on the testing methodology and results obtained by the proposed segmentation algorithm on cardiac MRI. Left ventricle segmentation on the SCD dataset has shown comparable results with other state of the art segmentation methods. The main reason for the divergence is that the proposed method removes papillary muscles and trabeculae from the segmentation contour, whereas the representation of the ground truth contour did not. However, the segmentation of the right ventricle from the RVSCD dataset using the proposed algorithm has shown excellent results when compared to state of the art approaches. The results of the segmentation of the locally obtained MRI dataset from the University of the Freestate has depicted measures in the acceptable range for all three MRI views.

CHAPTER 7 - VISUALISATION OF CARDIAC VENTRICLES

Image segmentation of an object of interest, such as the ventricles, will produce a set of points that is a subset of the respective MRI per slice. Combining segmentation of MRI slices for that object will create a set of points in the three dimensional space, known as the three dimensional point set. The natural follow up from the segmentation is to produce a visualisation in the three dimensional space. Surface reconstruction is the process of finding a mathematical description of the physical shape created from the three dimensional point set [45]. Once the surface mesh is created for the object of interest, the volume within the mesh can be calculated which can then provide several quantification measures.

Section 7.1 provides a background into triangular mesh reconstruction. Thereafter, two methods of improving the ventricle volumetric calculation is proposed in Section 7.2. These methods will in turn improve the visualisation. The first method uses segmentation from three cardiac MRI views to obtain a better visualisation of the ventricles. This removes the uncertainty of whether to use the end slice thickness. The second proposed approach fits a surface mesh around the outer segmentation points using Delaunay triangulation, convex hulls and alpha hulls. The ventricle volume is then calculated after converting the closed surface mesh into a voxel volume. Results of these two proposed methods on an MRI dataset are presented in 7.3.

7.1 Triangular Surface Mesh Reconstruction

A triangular mesh consists of the three dimensional point set as its vertices and a structure that connects these vertices to form triangles or faces. The mesh is normally continuous with the ability of having different triangle sizes to achieve good approximation of the physical surface [45]. The Delaunay triangulation is defined as the collection of edges from the three dimensional point set. The edge is a part of the collection if and only if there exists a circle that passes through the vertices of that edge and the circle does not contain any other vertex within [46]. This is visually represented in Figure 7-1 where it can be seen that the circumscribed circles do not contain any of the other points within. An example of the Delaunay triangulation on a three dimensional point set is shown in Figure 7-2.

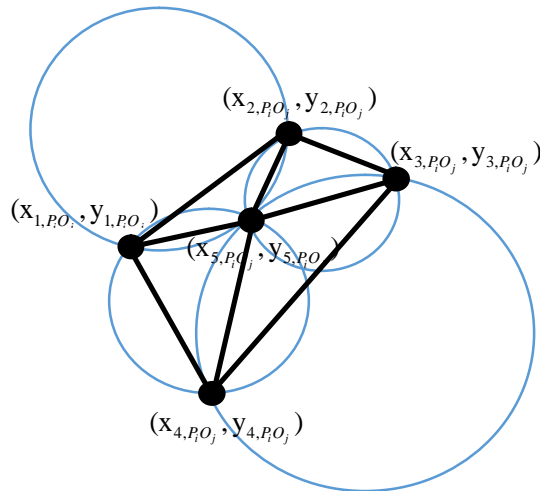


Figure 7-1: Delaunay Triangulation on a set of five points with circumscribed circles.

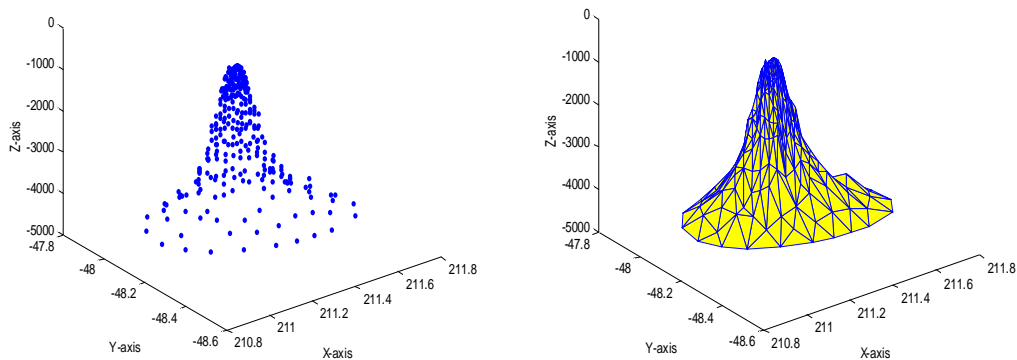


Figure 7-2: Delaunay Triangulation on a three dimensional point set.

The Delaunay triangulation normally describes convex type surfaces due to the circular fit. There have several algorithms in literature that adapts and improves on the Delaunay triangulation to describe concave and other types of surfaces. These include the alpha shapes or alpha hulls algorithm, crust algorithm and Cocone algorithm. A full review of these algorithms is provided in [45] and [47].

7.2 Ventricle Visualisation Methods

An MRI, acquired from a machine, consists of a two dimensional matrix of pixels derived from a corresponding set of three dimensional volume elements which is known as a voxels. The size of the voxel is dependent on the MRI slice thickness, field of view and matrix size [3]. As a general rule of thumb, as the voxel size decreases, the MRI resolution increases, which will in turn provide a better representation of the object of interest. In clinical practice, an optimal slice thickness is sought. Thinner slices can be susceptible to a high level of RF noise, whereas

thicker slices are associated with issues such as increased partial volume effect [3]. From Section 3.2, it can be concluded that a more accurate ventricle volumetric calculation algorithm is required, especially when the slice thickness is large.

7.2.1 Utilising MRI Segmentation Information from Three Views

As discussed in Section 2.2 and 2.3, standard cardiac MRI acquires orthogonal slices in three views namely two chamber view (2CV), four chamber view (4CV) and short axis view (SAV) [1]. Images in each of these views have a link to the patient co-ordinate system and several slices can be obtained per view. The DICOM [17] header describes the parameters of conversion from the slice plane to the patient co-ordinate system.

To enhance ventricle volume visualisation, it is proposed that multiple slices in the 2CV and 4CV be acquired per patient together with the ventricle segmentation dataset on all three views. Ventricle segmentation can be performed using manual delineation or using existing semi-automatic or fully automatic algorithms from Chapter 4. This proposed method of volume visualisation can be supported by Figure 7-3, where the additional points (three dimensional point set) generated by the 2CV and 4CV segmentation (in red), reveals additional volume portions that were not included by the application of Simpsons rule in Figure 3-9.

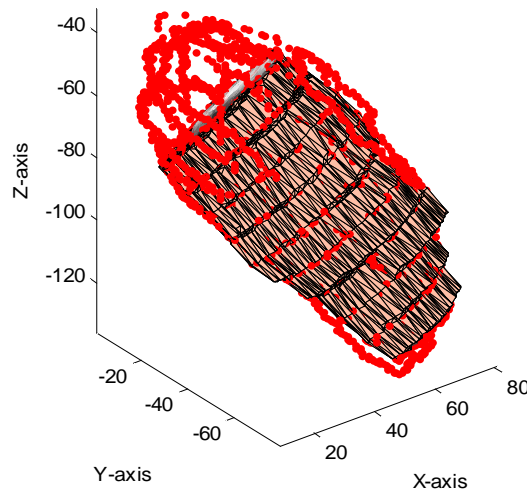


Figure 7-3: Additional segmentation information from two chamber and four chamber MRI view (red plot) projected onto short axis segmented portions of the left ventricle encased in a surface plot using Simpsons rule.

It must be noted that if the slice thickness was considered above slice 10 in Figure 3-9, the volume excluded by the Simpson's method will be reduced. However there will still be some degree of error.

It can also be seen from Figure 7-3 that the ventricle ends are rounded, allowing a better fit to the actual left ventricle shape. Furthermore, the step surface also encloses some of the boundary points which could result in volume over estimation. Figure 7-4 extracts and displays all segmented areas per MRI view per slice of both the left and right ventricle collated on a single three dimension view.

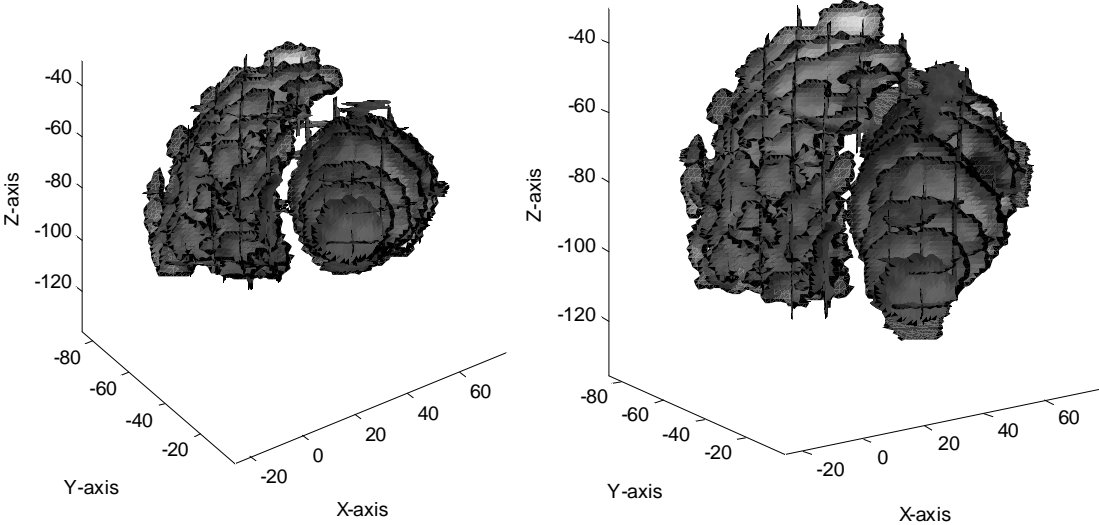


Figure 7-4: Two three dimension plots of segmented area of the left and right ventricle from the two chamber view, four chamber view and short axis view.

From Figure 7-4, an improved visualisation of the ventricle shapes is achieved. In order to calculate the volume contained within the information obtained from the three MRI views, a surface must enclose all the segmented areas. This is discussed in Section 7.2.2 below.

7.2.2 Triangular surface mesh formation and volume calculation

The three dimensional point set defined by the segmentation from all three MRI views does not contain enough information to enable accurate calculation of the enclosed volume. In this section it is proposed that a triangular surface mesh reconstruction algorithm be used to extract the ventricle surface from the three dimensional point set and calculate the enclosed volume of the surface.

Let $S_{SAV,2CV,4CV,RV}$ denote the three dimensional point set obtained by combining the right ventricle segmentation of slices from the SAV, 2CV and 4CV, where:

$$S_{SAV,2CV,4CV,RV} = \{S_{P,O_j}\} : 1 \leq i \leq a, j = 1, \tag{7.1}$$

and a is the total number of MRIs that cover the right ventricle in all the views. The Delaunay triangulation (DT) algorithm [63] is used to perform the initial surface reconstruction which

returns the set of vertices and faces (FV_{DT}) that represents the triangular surface mesh and is represented as:

$$FV_{DT} = DT(S_{SAV,2CV,4CV,RV}). \quad (7.2)$$

An example of the three dimensional point set for the right ventricle is shown in Figure 7-5 and the resultant Delaunay triangulation is depicted in Figure 7-6.



Figure 7-5: Three dimensional point set of the right ventricle obtained by combining segmentation from all three MRI views.

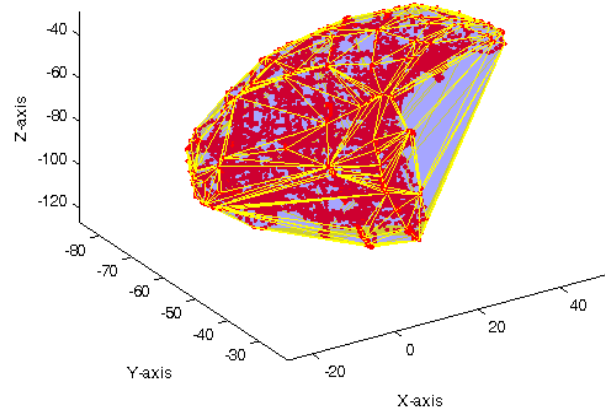


Figure 7-6: Three dimensional point set (red) and Delaunay triangulation (transparent blue faces and yellow edges) of the right ventricle.

From Figure 7-6 it is apparent that the reconstruction produces the convex hull of the point set and does not accurately reproduce the concaved shape of the right ventricle. To overcome this problem it is proposed that the alpha hull (AH) [64] of the Delaunay triangulation be computed, which will produce another set of faces and vertices FV_{AH} , which is denoted as follows:

$$FV_{AH} = AH(DT(S_{SAV,2CV,4CV,RV})). \quad (7.3)$$

The alpha radius (α_R) of the AH controls the level of detail of the resultant surface mesh. A value of $\alpha_R = \infty$ returns the convex hull of the points and if α_R is chosen too small there will be holes in the reconstructed mesh surface. Determining the optimal α_R is often done by experimentation [65], however a novel method of calculating the α_R is proposed as follows for a given point set:

$$\alpha_R = L \times \left(1 - \frac{N_{EAV}}{N_E} \right) \quad (7.4)$$

L is the average edge length of the triangles in the convex hull of $S_{SAV,2CV,4CV,RV}$, N_{EAV} is the number of edges that are longer than L and N_E is the total number of edges in the convex hull. This method to calculate the α_R produces a tight triangular surface mesh with no holes as shown in Figure 7-7. It is important that no holes are present in the final surface mesh as each of the mesh faces are used in determining the bounding volume.

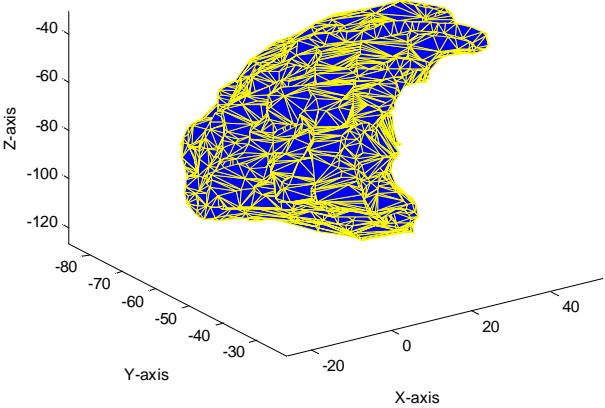


Figure 7-7: Alpha hull accurately represents the concaved structure of the right ventricle (blue faces and yellow edges).

To improve the resolution of the triangular surface mesh model created in (7.3), a ray tracing mesh voxelisation technique similar to that described in [62] is used. This method begins with a $100 \times 100 \times 100$ voxel cube and traces rays along the X, Y and Z axis until they intersect with the mesh faces. The points of intersection along the rays are marked off as the voxel surface. The result is a high resolution voxel representation of the original surface mesh. The volume enclosed by the mesh (or three dimensional point set) is then computed by performing a count of the number of voxels making up the high resolution voxel representation multiplied by the volume of an individual voxel. The computation of the left ventricle volume follows the same procedure as described above.

7.3 Results of Ventricle Visualisation Method

A cardiac MRI dataset was obtained from the Universitas Hospital (University of the Free State) which consisted of five volunteers with no cardiac abnormalities. Full imaging in the SAV, 2CV and 4CV were performed on each volunteer. MRI's were of size 256x256 pixels, 20 images per cardiac cycle and a slice thickness of 9mm in all views. The dataset also consisted of expert manual delineation of the left ventricle and right ventricle in the SAV, 2CV and 4CV at the end diastole and end systole cardiac times. It must be noted that papillary muscles were excluded in the expert ventricular segmentation.

Using the expert manual segmentation, the left and right ventricles were extracted for each MRI view per volunteer and combined to form two three dimensional point sets, one at the end diastolic cardiac time and the other at the end systolic. Thereafter the proposed triangular surface mesh method described in Section 7.2.2 was applied to each point set. The three dimensional point set for the left ventricle of a volunteer contained 4145 vertices from the segmentation of the three views and obtained a higher resolution after voxelisation by containing 194951 voxels. Table 7-1 provides the comparative results per volunteer between Simpsons rule and the proposed method for calculating volume at the end-diastolic cardiac time. The calculated average of the Simpsons rule across all MRI view is also depicted. The average volume value only holds true if the segmentation of all three views cover the entire volume, which is not the case.

Table 7-1: Volumetric measurements of Simpsons Rule versus Proposed method for all MRI views at the end diastolic cardiac time.

Volunteer Number	Left Ventricle Volume Measures using Simpsons Rule (ml)				Right Ventricle Volume Measures using Simpsons Rule (ml)				Volume Measures using Proposed Method (ml)		% Difference Between Simpsons Rule and Proposed Method	
	2CV	4CV	SAV	Avg.	2CV	4CV	SAV	Avg.	Left Ventricle	Right Ventricle	Left Ventricle	Right Ventricle
1	94.82	97.38	87.52	93.24	97.47	82.00	84.89	88.12	94.55	98.09	1.39	10.16
2	67.73	67.19	78.93	71.29	52.77	60.80	71.25	61.61	76.80	70.26	7.18	12.32
3	81.32	72.47	72.19	75.33	76.30	68.02	61.15	68.49	75.29	70.85	0.05	3.33
4	92.76	89.31	70.00	84.03	87.72	83.12	52.29	74.38	100.30	93.18	16.22	20.18
5	67.83	85.53	61.59	71.65	60.29	77.82	60.34	66.15	81.36	78.33	11.93	15.55

Avg. = Average volume value of Simpsons Rule in the three MRI views.

2CV = Two Chamber View

4CV = Four Chamber View

SAV = Short Axis View

Figure 7-8 shows the visualisation of the left and right ventricles at the end diastolic cardiac time for one of the volunteers. Due to the smooth surface fit, papillary muscles are included within the surface. Table 7-2 and Figure 7-9 provides a comparison of the stroke volume per volunteer, showing on an average a stroke volume error 2.14%.

Table 7-2: Stroke Volume measurements of Simpsons Rule versus Proposed method.

Volunteer Number	Simpsons Rule			Proposed Method		
	Stroke Volume Left Ventricle (ml)	Stroke Volume Right Ventricle (ml)	Stroke Volume Error (%)	Stroke Volume Left Ventricle (ml)	Stroke Volume Right Ventricle (ml)	Stroke Volume Error (%)
1	52.7	47.3	5.3	48.51	47.99	1.07
2	47.1	35.1	12	38.00	36.51	3.93
3	50.7	40.8	9.9	40.60	41.82	2.99
4	59.8	47.0	12.8	56.74	55.69	1.86
5	44.6	30.1	14.4	43.08	43.45	0.86

From Figure 7-8 it can be clearly seen that a high quality visualisation of the cardiac ventricles is achieved, with a smooth surface covering the entire ventricle without any holes. The presence of the ellipsoidal (or oval) shape of the left ventricle and the combined crescent/triangular shape

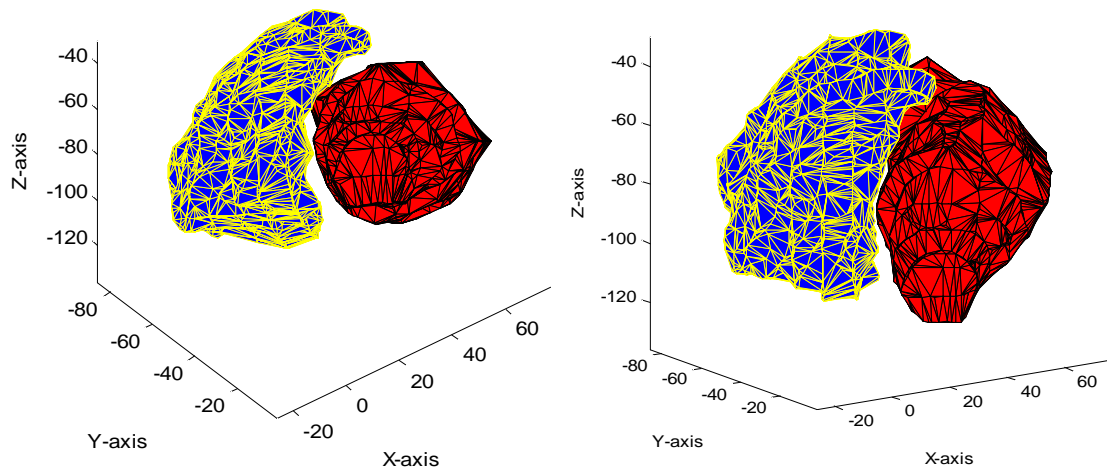


Figure 7-8: Two mesh surface plots of segmented area of the left and right ventricle using the proposed algorithm.

of the right ventricle can clearly be observed. There is also a space between the ventricles which can be attributed to the ventricle walls.

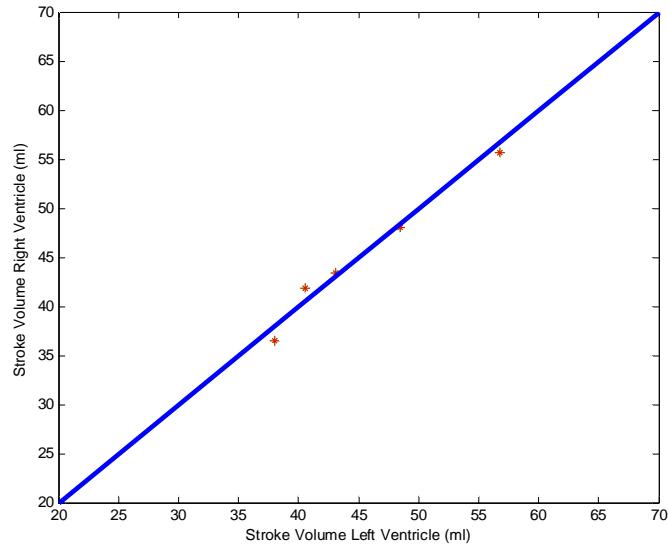


Figure 7-9: Visual comparison of the left and right ventricle stroke volume after applying the proposed method of volume calculation.

There is a slight difference between the ventricle volume calculation of the proposed method in comparison to Simpsons rule, indicating on average a 7.35% deviation in the left ventricle and 12.31% deviation in the right ventricle across the five volunteers. In some volunteers the volume difference is not that significant, since some of the points from the three dimensional point set lie within the slice thickness area of the Simpsons rule and the remaining on the outside. Thus no clear trend could be established in the volume data from both methods, due to the volume over-estimation and under-estimation by the Simpsons rule. Another comparison done was to use the segmentation results for a patient using the proposed segmentation algorithm (Table 6-10) and apply the proposed volumetric calculation method to the segmentation contours. This is depicted in Table 7-3, where the difference is similar to that obtained from Table 7-1.

Table 7-3: Comparison of Volumetric measurements of Simpsons Rule versus Proposed method for all MRI views at both cardiac phases for a patient whose results is obtained by using the proposed segmentation algorithm (Table 6-10).

Cardiac Phase	Left Ventricle Volume Measures using Simpsons Rule (ml)				Right Ventricle Volume Measures using Simpsons Rule (ml)				Volume Measures using Proposed Method (ml)		% Difference Between Simpsons Rule and Proposed Method	
	2CV	4CV	SAV	Avg.	2CV	4CV	SAV	Avg.	Left Ventricle	Right Ventricle	Left Ventricle	Right Ventricle
End-Diastole	90.7	109.7	79.6	93.3	97.9	105.1	97.4	100.1	97.6	99.1	4.3	1.0
End-Systole	38.8	44.7	28.1	37.2	52.2	43.2	43.5	46.3	40.2	42.4	3.0	3.9

Avg. = Average volume value of Simpsons Rule in the three MRI views.

The high accuracy of the proposed method of volume calculation is achieved by the low stroke volume error, which can be credited to both the segmentation of all three MRI views as well as the ability of the proposed algorithm to accurately approximate the surface mesh by voxelisation.

7.4 Summary

In this Chapter an improved method of calculating cardiac ventricular volumes is proposed using convex and alpha hulls to obtain the triangular surface mesh. Thereafter, a high resolution voxelisation of the ventricle mesh is performed, from which the volume is calculated. A higher quality visualisation of the ventricles is thus achieved, showing a smooth surface cover. The results indicate that this method performs better than Simpsons rule for volume calculation as the stroke volume errors calculated over all volunteers using the proposed algorithm are lower than that obtained using Simpsons rule.

CHAPTER 8 - CONCLUSION

This thesis has presented and discussed several aspects of cardiac MRI ventricle segmentation and proposed a new ventricle segmentation algorithm as well as a new ventricle volumetric calculation algorithm. In this chapter, the important findings and conclusions of each of the chapter are initially presented. Thereafter, future work and recommendations, which could improve the overall performance of the proposed algorithms are described.

8.1 Chapter Summaries

The thesis starts with an introduction to MRI and segmentation, focussing on the human heart. Literature review of state of the art cardiac MRI segmentation methods, in Chapter 4, showed that there are many image processing approaches that could be used to segment both the left and right ventricles, with approximately 65% of the methods focussing on the left ventricle. However, the results presented by more than 90% of the authors was achieved using their own cardiac MRI dataset. This posed a major problem in comparing the different ventricle segmentation algorithms.

To address this issue, a framework for the evaluation of segmentation algorithms on cardiac MRI is presented in Chapter 3, by using mathematical, statistical and clinical measures on publically available MRI datasets. More specifically the framework recommended that the Hausdorff distance, Dice coefficient and stroke volumes be used. The effectiveness of each measure is quantified through a series of tests that manipulates the ground truth segmentation contour. It was shown that mathematical or distance based measures are particularly sensitive to the 'panhandle problem', where a strong local deviation that does not necessarily take up much volume, results in a high distance value. On the other hand, statistical measures are sensitive to misplacement of the segmentation contour. The major contribution in the framework was to introduce the clinical measure of stroke volume error between the left and the right ventricle. As shown in the results, this measure provided a good estimation of segmentation accuracy. However, this method is affected by systematic left and right ventricle segmentation errors such as slice thickness error. Thus it is proposed that a combination of all of these measures must be used to assess the accuracy of any MRI ventricle segmentation algorithm.

Chapter 5 introduced a robust novel three dimensional automatic left and right ventricle segmentation algorithm. This technique was split into two parts, depending on the type of cardiac MRI dataset presented to segment. Both approaches performed ventricle localisation as the initial step and thereafter applied the difference of Gaussian image filter. It was shown that the difference of Gaussian image filter provides good ventricle segmentation if the filter parameters are chosen properly. Thus a novel system was developed to choose these parameters by looking at the pixel intensity profile within the ventricle region of interest.

If the dataset only contained the short axis MRI view, the ventricle region of interest was formed by the use of standard deviation motion maps in combination with the wavelet transform. This approach allowed comparison to state of the art methods, where left ventricle on the SCD had shown comparable results and the right ventricle segmentation has shown significant improvement. The main reason for the divergence is that the proposed method removes papillary muscles and trabeculae from the segmentation contour, whereas the representation of the ground truth contour did not. In addition, the robustness of the algorithm was tested against simulated noisy and blurry images, which also displayed encouraging results.

The second approach of ventricle localisation was formed if the cardiac MRI dataset contained three MRI views (SAV, 2CV and 4CV). A novel, iterative three dimensional left and right ventricle segmentation algorithm was presented, in which the segmentation is automatically performed in the third MRI view by projecting the segmentation from the other two views into the patient coordinate system. It was shown that the region of interest created by the projection accurately splits the ventricle from the atrium in MRI views, where the intensity and texture values are the same for both chambers, as in the 2CV and 4CV. The results provided revealed that segmentation accuracy increases per iteration and convergence is achieved in approximately four iterations.

A new algorithm for the visualisation of the segmented ventricles and computation of ventricle volumes was described in Chapter 7, to account for the inaccuracy measure due to the slice thickness. The method included using Delaunay triangulation during the surface mesh reconstruction. The volumetric calculation was compared against the commonly used Simpsons method, exhibiting an improved performance. It was also revealed in this chapter 7 that using segmentation information from the three orthogonal MRI views yields a better visualisation of the ventricles. Thus the resultant surface mesh was much smoother as more points were available for the triangulation method.

8.2 Future Work

All results were obtained using the Matlab software environment [51] with little processing or memory optimisation used on matrix and image processing. Furthermore, it was beyond the scope of this research to time profile each simulation. Thus, for the two proposed MRI ventricle segmentation algorithms to be used for real time diagnosis, it is recommended that another programming language such as Microsoft Visual C++ be used.

Another optimisation that could be performed is to use a more accurate initial segmentation algorithm to the method proposed in Section 5.4, especially in the 2CV or 4CV MRI. This will result in quicker convergence of the algorithm as well as provide more accurate volumetric measurements.

The visualisation algorithm that appears in the chapter 7 does not make provision for the presence of papillary muscles, even though the segmentation per MRI may consider these muscles. Thus an improvement could be made where the papillary muscles could be fit with a triangular surface mesh. The actual ventricle volume will now be the difference between the total mesh coverage and the volume of the papillary mesh.

This work can readily be extended to segment the outer surfaces of the cardiac muscle and thus a segmentation of the entire heart and not only the cavities off the ventricles could be achieved using the algorithms proposed here.

REFERENCES

- [1] N. Willemse, "Manual Quantification for Right and Left Ventricular Function using Cardiac Magnetic Resonance Imaging," M.Sc. Thesis, University of the Free State, July 2012.
- [2] C. Petitjean, J.N. Dacher, "A Review of Segmentation Methods in Short Axis Cardiac MR Images," *Medical Image Analysis Journal*, Vol. 15, Issue 2, Pages 169-184, 2011.
- [3] D. Weishaupt, V.D. Köchli, B. Marincek, "How Does MRI Work? An Introduction to the Physics and Function of Magnetic Resonance Imaging," 2nd Edition, Springer Berlin, 2006.
- [4] P.A. Laizzo, "Atlas of Human Cardiac Anatomy: A Web Based Textbook", Regents of the University of Minnesota, 2005. Available at: <http://www.vhlab.umn.edu/atlas>.
- [5] World Health Organisation, "Global Status Report on Non Communicable Diseases 2010", World Health Organisation, Geneva, 2011.
- [6] F. Grothues, J.C. Moon, N.G. Bellenger, G.S. Smith, H.U. Klein, D.J. Pennell, "Interstudy Reproducibility of Right Ventricular Volumes, Function, and Mass with Cardiovascular Magnetic Resonance," *American Heart Journal*, Vol. 147, Issue 2, Pages 218-223, 2003.
- [7] D. Drake, R. Gupta, S.G. Lloyd, H. Gupta, "Right Ventricular Function Assessment: Comparison of Geometric and Visual Method to Short-Axis Slice Summation Method," *Echocardiography*, Vol. 24, Issue 10, Pages 1013-1019, 2007.
- [8] C.B. Marcu, A.M. Beek, A.C Van Rossum, "Cardiovascular Magnetic Resonance Imaging for the Assessment of the Right Heart Involvement in Cardiac and Pulmonary Disease," *Heart and Lung Circulation*, Vol. 15, Issue. 6, Pages 362-370, 2006.
- [9] A. Andreopoulos, J.K. Tsotsos, "Efficient and Generalisable Statistical Models of Shape and Appearance for Analysis of Cardiac MRI," *Medical Image Analysis*, Vol. 12, Issue 3, Pages 335-357, 2008.
- [10] G.M. Davis, A. Nosratinia, "Wavelet-based Image Coding: An Overview," *Applied and Computational Control, Signals, and Circuits*, Vol. 1, Issue 1, 1998.
- [11] R.C. Gonzalez, R.E. Woods, "Digital Image Processing," 2nd Edition, Prentice Hall Inc., New Jersey, 2002.
- [12] Yale Medical Group, "Valvuloplasty," Yale School of Medicine, New Haven, 2013. Available at <http://yalemedicalgroup.org/info/health.aspx?ContentTypeId=92>.
- [13] D.U. Silverthorn, "Human Physiology: An Integrated Approach," 2nd Edition, Prentice Hall Inc., New Jersey, 2001.
- [14] K.B. Chandran, S.E. Rittgers, A.P. Yoganathan, "Biofluid Mechanics: The Human Circulation," CRC Press, Taylor and Francis Group, New York, 2007.
- [15] M.B. Stegmann, "Generative Interpretation of Medical Images," Ph.D. thesis, Informatics and Mathematical Modelling, Technical University of Denmark, 2004.
- [16] J.P. Hornak, "The Basics of MRI," Interactive Learning Software, Henrietta, New York, 2010. Available at <https://www.cis.rit.edu/htbooks/mri/>.

- [17] National Electrical Manufacturers Association, "Digital Imaging and Communications in Medicine (DICOM), Part 1: Introduction and Overview," Rosslyn, Virginia, 2011.
- [18] A. Fedorov, R. Beichel, J. Kalpathy-Cramer, J. Finet, J.-C. Fillion-Robin, S. Pujol, et al., "3D Slicer as an Image Computing Platform for the Quantitative Imaging Network," *Magnetic Resonance Imaging*, Vol. 30, Issue 9, 2012.
- [19] R. Zaharia, "DICOM is Easy: Introduction to DICOM." Available at <http://dicomiseasy.blogspot.com/>.
- [20] M. Gao, C. Chen, S. Zhang, Z. Qian, D. Metaxas, et al., "Segmenting the Papillary Muscles and the Trabeculae from High Resolution Cardiac CT through Restoration of Topological Handles," *Information Processing in Medical Imaging, Computer Science*, Vol. 7917, Issue 1, Pages 184-195, 2013.
- [21] T. Geva, D.J. Sahn, A.J. Powell, "Magnetic Resonance Imaging of Congenital Heart Disease in Adults," *Progress in Paediatric Cardiology*, Vol. 17, Issue 1, Pages 21-39, 2003.
- [22] The University of Chicago, "Cardiac MRI," The University of Chicago Medical Centre, 2014. Available at: www.uchospitals.edu/specialities/heart/services/imaging/mri.html.
- [23] P. Carreno-Moran, J. Breeze, M. Rees, "The Top Ten Cases in Cardiac MRI and the Most Important Differential Diagnoses," Intech Open Access Publisher, 2013.
- [24] A. Sharma, P. Kaur, "Review of CAD Techniques for Liver Tumor Detection," *International Journal of Advanced Research in Computer Science and Software Engineering*, Vol. 3, Issue 10, 2013.
- [25] J.S. Suri, "Computer Vision, Pattern Recognition and Image Processing in Left Ventricle Segmentation: The Last 50 Years," *Pattern Analysis and Applications*, Vol. 3, Issue 3, Pages 209-242, 2000.
- [26] D. Baswaraj, A. Govardhan, P. Premchand, "Active Contours and Image Segmentation: The Current State of the Art," *Global Journal of Computer Science and Technology Graphics & Vision*, Vol. 12, Issue 11, 2012.
- [27] V. Murali, S. Boopathi, "Comparative Analysis of Various Segmentation Techniques in Brain Tumor Image," *International Journal of Application or Innovation in Engineering & Management*, Vol. 3, Issue 6, 2014.
- [28] F.M. Abubakar, "A Study of Region Based and Contour Based Image Segmentation," *Signal & Image Processing: An International Journal*, Vol. 3, Issue 6, 2012.
- [29] T. Lindeberg, "Scale-Space Theory: A Basic Tool for Analyzing Structures at Different Scales," *Journal Of Applied Statistics*, Vol. 21, Issue 1, Pages 225-270, 1994.
- [30] H. Winnemöller, J.E. Kyprianidis, S.C. Olsen, "XDoG: An Extended Difference of Gaussians Compendium Including Advanced Image Stylization," *Computers & Graphics*, Vol. 36, Issue 6, Pages 740-753, 2012.
- [31] D.R.C.L. Cheung, "Motion Segmentation Incorporating Active Contours for Spatial Coherence," Master of Applied Sciences Thesis, University of Toronto, 2004.
- [32] T.F. Cootes, G.J. Edwards, C.J. Taylor, "Comparing Active Shape Models with Active Appearance Models," *Proceedings of British Machine Vision Conference*, Pages 173-182, 1999.

- [33] T.F. Cootes, G.J. Edwards, and C.J. Taylor, "Active Appearance Models," Proceedings of European Conference on Computer Vision, Vol. 2, Pages 484-498, 1998.
- [34] L.I. Smith, "A tutorial on Principle Component Analysis," University of Otago, 2002. Available at: http://www.cs.otago.ac.nz/cosc453/student_tutorials/principal_components.
- [35] S.C. Mitchell, B.P.F. Lelieveldt, R.J. van der Geest, J.G. Bosch, J.H.C. Reiber, and M. Sonka, "Multistage Hybrid Active Appearance Model Matching: Segmentation of Left and Right Cardiac Ventricles in Cardiac MR Images," IEEE Transactions on Medical Imaging, Vol. 20, Pages 415-423, 2001.
- [36] J.G. Bosch, S.C. Mitchell, B.P.F. Lelieveldt, F. Nijland, O. Kamp, M. Sonka and J.H.C. Reiber, "Automatic Segmentation of Echocardiographic Sequences by Active Appearance Motion Models," IEEE Transactions on Medical Imaging, Vol. 21, Pages 1374-1383, 2002.
- [37] S.C. Mitchell, B.P.F. Lelieveldt, R.J. van der Geest, J.G. Bosch, J.H.C. Reiber, and M. Sonka, "3D Active Appearance Models: Segmentation of Cardiac MR and Ultrasound images," IEEE Transactions on Medical Imaging, Vol. 21, Pages 1167-1178, 2002.
- [38] C. Davatzikos, X. Tao and D. Shen, "Hierarchical Active Shape Models, Using the Wavelet Transform," IEEE Transactions on Medical Imaging, Pages 414-423, 2003.
- [39] P.D. Sozou, T.F. Cootes, C.J. Taylor and E.C. Di Mauro, "A Non-Linear Generalisation of Point Distribution Models using Polynomial Regression," Image and Vision Computing Journal, Vol. 13, Issue 5, Pages 451-457, 1995.
- [40] Ü. Mehmet, "Constrained Segmentation of Cardiac MR Image Sequences," Universal Press, Veenendaal, The Netherlands, 2007.
- [41] Y. Yuan, K. Barner, "An Active Shape Model Based Tactile Hand Shape Recognition with Support Vector Machines," IEEE Information Sciences and Systems, Issue 22-24, Pages 1611-1616, 2006.
- [42] R. Beichel, H. Bischof, F. Leberl, and M. Sonka, "Robust Active Appearance Models and Their Application to Medical Image Analysis," IEEE Transactions on Medical Imaging, Vol. 24, Pages 1151-1167, 2005.
- [43] T. Rohlfing, R. Brandt, R. Menzel, D.B. Russakoff, J. Maurer, R. Calvin, "Quo Vadis Atlas-Based Segmentation?," The Handbook of Medical Image Analysis, Vol. 3, Kluwer Academic/Plenum Publishers, New York, Pages 435-486, 2005.
- [44] M. Lorenzo-Valdes, G. Sanchez-Ortiz, R. Mohiaddin, D. Rueckert, "Atlas-Based Segmentation and Tracking of 3D Cardiac MR Images Using Non-Rigid Registration," Medical Image Computing and Computer Assisted Intervention, MICCAI, 2002.
- [45] I. Soderkvist, "Introductory Overview of Surface Reconstruction Methods," Department of Mathematics, Lulea University of Technology, 1999.
- [46] S. Peterson, "Computing Constrained Delaunay Triangulations," Minnesota Centre for Industrial Mathematics University of Minnesota, 1998.
- [47] R. Tang, S. Halim, M. Zulkepli, "Surface Reconstruction Algorithms: Review and Comparison," 8th International Symposium on Digital Earth, 2013.
- [48] H.C. van Assen, "3D Active Shape Modelling for Cardiac MR and CT Image Segmentation," Department Radiology, Faculty of Medicine, Leiden University, May 2006.

- [49] I. Daubechies, "Ten Lectures on Wavelets," Society for Industrial and Mathematics, Philadelphia, PA, 1992.
- [50] S.G. Mallat, "Multifrequency Channel Decompositions of Images and Wavelet Models," IEEE Transactions on Acoustic, Speech Signal Processing, Vol. 37, Pages 2091-2110, 1989.
- [51] The Mathworks Inc., "Matlab, The Language of Technical Computing," Version 7.9.0.592 Release 2009b, August 2002.
- [52] X. Lin, R. Cowan, A. Young, "Automated Detection of Left Ventricle in 4D MR Images: Experience from a Large Study," Proceedings of Medical Image Computing and Computer-Assisted Intervention (MICCAI), Vol. 9, Pages 7286735, 2006.
- [53] M. Kass, A. Witkin, D. Terzopoulos, "Snakes: Active Contour Models," International Journal of Computer Vision 1, Pages 3216332, 1988.
- [54] C. Xu, D.L. Pham, J.L. Prince, "Medical Image Segmentation Using Deformable Models", Handbook of Medical Imaging, Medical Image Processing and Analysis, Vol. 2, SPIE Press, Pages 1296174, 2000.
- [55] R.J. van der Geest, J.H.C. Reiber, "Quantification in Cardiac MRI," Journal of Magnetic Resonance Imaging, Vol. 10, Pages 602-608, 2000.
- [56] M.S. Nacif, A.D. Barranhas, E. Türkbey, E. Marchiori, N. Kawel, R.A.F. Mello, et al, "Left Atrial Volume Quantification Using Cardiac MRI in Atrial Fibrillation: Comparison of The Simpson's Method with Biplane Area-Length, Ellipse, and Three-Dimensional Methods," Diagnostic and Interventional Radiology, Vol. 19, Pages 213-220, 2013.
- [57] Y. Tsadok, Y. Petrank, S. Sarvari, T. Edvardsen, D. Adam, "Automatic Segmentation of Cardiac MRI Cines Validated for Long Axis Views," Computerised Medical Imaging and Graphics, Vol. 37, Issue 8, pages 5006511, 2013.
- [58] R. Sharma, A. Sharma, C.D. Williams, "A Simple Assessment of Left Ventricular Function and Mass with Cine MRI," Informatica Medica Slovenica, Vol. 12, Issue 2, Pages 22-28, 2007.
- [59] H. Thiele, I. Paetsch, B. Schnackenburg, A. Bornstedt, O. Grebe, E. Wellnhofer, et al, "Improved Accuracy of Quantitative Assessment of Left Ventricular Volume and Ejection Fraction by Geometric Models with Steady-State Free Precession," Journal of Cardiovascular Magnetic Resonance, Vol. 4, Issue 3, Pages 3276339, 2002.
- [60] S. Haji-Momenian, K. Chang, D. Grand, F. Sheehan, M. Atalay, "Measuring Right Ventricular Volume and Ejection Fraction with Simpson's Method: Which MRI Axis is Best? Comparison with a Gold Standard," Journal of Cardiovascular Magnetic Resonance, Vol.11, 2009.
- [61] A.J. Duerinckx, "Coronary Magnetic Resonance Angiography," Springer-Verlag New York Inc., 2002.
- [62] S. Patil, B. Ravi. "Voxel-Based Representation, Display and Thickness Analysis of Intricate Shapes," Computer Aided Design and Computer Graphics, 2005. Ninth International Conference on. IEEE, 2005.
- [63] B. Delaunay, "Sur La Sphere Vide," Izv. Akad. Nauk SSSR, Otdelenie Matematicheskii i Estestvennyka Nauk, Pages 793-800, 1934.

- [64] H. Edelsbrunner, E. P. Mücke, "Three-Dimensional Alpha shapes," *ACM Transactions on Graphics*, Vol. 13, Issue 1, Pages 43-72, 1994.
- [65] H. Edelsbrunner, "Alpha Shapes-a Survey," *Tessellations in the Sciences*, Vol. 27, 2010.
- [66] J. Lötjönen, J. Koikkalainen, K. Lauerma, "Improved Quantification of the Heart by Utilizing Images from Different Imaging Directions," *ERCIM News No. 60*, 2005.
- [67] L.G. Rudski, W.W. Lai, J. Afilalo, M.D. Handschumacher, K. Chandrasekaran, S.D. Solomon, et al, "Guidelines for the Echocardiographic Assessment of the Right Heart in Adults," *Journal American Society of Echocardiography*, Vol. 23, Pages 685-713, 2010.
- [68] A. Fenster, B. Chiu, "Evaluation of Segmentation algorithms for Medical Imaging," *Proceedings of the 2005 IEEE Engineering in Medicine and Biology 27th Annual Conference*, Shanghai, China, 2005.
- [69] C. Petitjean, M.A. Zuluaga, J.N. Dacher, D. Grosgeorge, J. Caudron, et al, "Right Ventricle Segmentation from Cardiac MRI: A Collation Study," *Medical Image Analysis*, Vol. 19, Issue 1, Pages 187-202, 2015.
- [70] H. Zhang, J.E. Fritts, S.A. Goldman, "Image Segmentation Evaluation: A Survey of Unsupervised Methods," *Computer Vision and Image Understanding*, Vol. 110, Pages 260-280, 2008.
- [71] P. Radau, U. Lu, K. Connelly, G. Paul, A.J. Dick, G.A. Wright, "Evaluation Framework for Algorithms Segmenting Short Axis Cardiac MRI," *The MIDAS Journal - Cardiac MR Left Ventricle Segmentation Challenge*, 2009. Available at: <http://hdl.handle.net/10380/3070>.
- [72] J. Caudron, J. Fares, V. Lefebvre, P.H. Vivier, C. Petitjean, J. N. Dacher, "Cardiac MR Assessment of Right Ventricular Function in Acquired Heart Disease: Factors of Variability," *Academic Radiology*, Vol. 19, Issue 8, Pages 991-1002, 2012.
- [73] J.K. Udupa, V.R. LeBlanc, Y. Zhuge, C. Imielinska, H. Schmidt, et al, "A Framework for Evaluating Image Segmentation Algorithms," *Computerised Medical Imaging and Graphics*, Vol. 30, Pages 75-87, 2006.
- [74] H.N. Boone, D.A. Boone, "Analyzing Likert Data," *Journal of Extension*, Vol. 50, Issue 2, 2012.
- [75] L.A. Soberano, "The Mathematical Foundation of Image Compression," *University of North Carolina, Wilmington, North Carolina*, 2000.
- [76] W.R. Crum, O. Camara, D.L.G Hill, "Generalised Overlap Measures for Evaluation and Validation in Medical Image Analysis," *IEEE Transactions on Medical Imaging*, Vol. 25, Issue 11, Pages 1451-1461, 2006.
- [77] Y. Zhu, X.Y. Luo, H. Gao, C. McComb, C. Berry, "A Numerical Study of a Heart Phantom Model," *International Journal of Computer Mathematics*, Vol. 91, Issue 7, Pages 1535-1551, 2014.
- [78] A. Akhondi-Asl, S.K. Warfield, "A Tutorial Introduction to STAPLE," *Computational Radiology Laboratory, Children's Hospital Boston, Harvard Medical School*, 2009.
- [79] T. Ino, L.N. Benson, H. Mikalian, R.M. Freedom, R.D. Rowe, "Determination of Left Ventricular Volumes by Simpson's Rule in Infants and Children with Congenital Heart Disease," *British Heart Journal*, Vol. 61, Issue 2, Pages 182-185, 1989.

- [80] K. Babalola, B. Patenaude, P. Aljabar, J. Schnabel, D. Kennedy, et al, "Comparison and Evaluation of Segmentation Techniques for Subcortical Structures in Brain MRI," *Medical Image Computing and Computer Assisted Intervention, MICCAI 2008*, Pages 409-416, Berlin, 2008.
- [81] A. Goshtasby, D. Turner, "Segmentation of Cardiac Cine MR Images for Extraction of Right and Left Ventricular Chambers," *IEEE Transactions on Medical Imaging*. Vol. 14 (1), Pages 566-64, 1995.
- [82] S. Kaushikkar, D. Li, E. Haale and V. Davila-Rom, "Adaptive Blood Pool Segmentation in Three-dimensions: Application to MR Cardiac Evaluation," *Journal of Magnetic Resonance Imaging*, Vol. 6, Pages 690-697, 1996.
- [83] J. Weng, A. Singh and M. Chiu, "Learning-based Ventricle Detection from Cardiac MR and CT Images," *IEEE Transactions on Medical Imaging*, Vol. 16 (4), Pages 378-391, 1997.
- [84] E. Nachtomny, R. Cooperstein, M. Vaturi, E. Bosak, Z. Vered and S. Akselrod, "Automatic Assessment of Cardiac Function from Short-axis MRI: Procedure and Clinical Evaluation," *Journal of Magnetic Resonance Imaging*, Vol. 16, Pages 365-376, 1998.
- [85] G. Waiter, F. McKiddie, T. Redpath, S. Semple and R. Trent, "Determination of Normal Regional Left Ventricular Function from Cine-MR Images using a Semi-automated Edge Detection Method," *Journal of Magnetic Resonance Imaging*, Vol. 17(1), Pages 99-107, 1999.
- [86] A. Katouzian, E. Konofagou and A. Prakash, "A New Automated Technique for Left-and Right-ventricular Segmentation in Magnetic Resonance Imaging," *Conference Proceedings IEEE Engineering Medical Biological Society*, Vol. 1, Pages 3074-3077, 2006.
- [87] H. Liu, H. Hu, X. Xu and E. Song, "Automatic Left Ventricle Segmentation in Cardiac MRI using Topological Stable-state Thresholding and Region Restricted Dynamic Programming," *Academic Radiology Journal*, Vol. 19(6), Pages 723-731, 2012.
- [88] H. Lee H, N.C. Codella, M.D. Cham, J.W. Weinsaft, Y. Wang Y, "Automatic Left Ventricle Segmentation using Iterative Thresholding and an Active Contour Model with Adaptation on Short-axis Cardiac MRI," *IEEE Transactions on Biomedical Engineering*, Vol. 57, Pages 905-913, 2010.
- [89] S. Ranganath, "Contour Extraction from Cardiac MRI Studies using Snakes," *IEEE Transaction of Medical Imaging*, Vol. 14 (2), Pages 328-338, 1995.
- [90] E. Heiberg, L. Wigstrom, M. Carlsson, A. Bolger and M. Karlsson, "Time Resolved Three-dimensional Segmentation of the Left ventricle," *Proceedings of IEEE Computers in Cardiology*, Vol. 32, Pages 599-602, 2005.
- [91] G. Hautvast, S. Lobregt, M. Breeuwer and F. Gerritsen, "Automatic Contour Propagation in Cine Cardiac Magnetic Resonance Images," *IEEE Transactions on Medical Imaging*, Vol. 25 (11), Pages 1472 - 1482, 2006.
- [92] L. Zhukov, J. Bao, I. Guskov, J. Wood, and D. Breen, "Dynamic Deformable Models for 3D MRI Heart Segmentation," *Proceedings of SPIE. Medical Imaging*, Pages 1398-1405, 2002.
- [93] A. Chakraborty, L. Staib and J. Duncan, "Deformable Boundary Finding in Medical Images by Integrating Gradient and Region Information," *IEEE Transaction on Medical Imaging*, Vol 15, Pages 859-870, 1996.

- [94] S. Mitchell, J. Bosch, B. Lelieveldt, R. van der Geest, J. Reiber and M. Sonka, "3-D Active Appearance Models: Segmentation of Cardiac MR and Ultrasound Images," *IEEE Transactions on Medical Imaging*, Vol. 21 (9), Pages, 1167-1178, 2002.
- [95] B. Lelieveldt, S. Mitchell, J. Bosch, R. van der Geest, J. Reiber and M. Sonka, "Time-Continuous Segmentation of Cardiac Image Sequences using Active Appearance Motion Models," *Information Processing in Medical Imaging: 17th International Conference (IPMI)*. Pages 446, 2001.
- [96] M. Urschler, H. Mayer, R. Bolter and F. Leberl, "The Livewire Approach for the Segmentation of Left Ventricle Electron-Beam CT Images," *Proceedings 26th Workshop of the Austrian Association for Pattern Recognition: Vision with Non-traditional Sensors, Volume: OCG 160*, 2002.
- [97] J. Loucky and T. Oberhuber, "Graph Cuts in Segmentation of a Left Ventricle from MRI Data," *Proceedings of the Czech-Japanese Seminar in Applied Mathematics 2010*, Pages 46-54, 2010.
- [98] D. Grosgeorge, C. Petitjean, S. Ruan, J. Caudron and J.N. Dacher, "Right Ventricle Segmentation by Graph Cut with Shape Prior," *MICCAI International Workshop, Right Ventricle Segmentation Challenge*, 2012.
- [99] D. Mahapatra and J.M. Buhmann, "Automatic Cardiac RV Segmentation using Semantic Information with Graph Cuts," *IEEE International Symposium Biomedical Imaging*, Pages 1094-1097, 2013.
- [100] O. Maier, D. Jimenez, A. Santos and M. Ledesma-Carbayo, "Segmentation of RV in 4D Cardiac MR Volumes using Region-Merging Graph Cuts," *IEEE Computing in Cardiology*, Pages 697-700, 2012.
- [101] A. Boudraa, "Automated Detection of the Left Ventricular Region in Magnetic Resonance Images by Fuzzy C-Means Model," *International Journal on Cardiovascular Imaging*, Vol. 13 (4), Pages 347-355, 1997.
- [102] D. Gering, "Automatic Segmentation of Cardiac MRI," *Proceedings of Medical Image Computing and Computer-Assisted Intervention (MICCAI)*. No. 1 in LNCS, Pages 524-532, 2003.
- [103] M. Lynch, O. Ghita and P. Whelan, "Automatic Segmentation of the Left Ventricle Cavity and Myocardium in MRI Data," *Computers in Biology and Medicine*, Vol. 36 (4), Pages 389-407, 2006.
- [104] G. Kedenburg, C. Cocosco, U. Kothe, W. Niessen, E. Vonken and M. Viergever, "Automatic Cardiac MRI Myocardium Segmentation Using Graphcut," *Proceedings of SPIE*. No. 6144 in *Medical Imaging*, 2006.
- [105] A. Pednekar, U. Kurkure, R. Muthupillai and S. Flamm, "Automated Left Ventricular Segmentation in Cardiac MRI," *IEEE Transactions on Biomedical Engineering*, Vol. 53 (7), Pages 1425-1428, 2006.
- [106] C. Cocosco, W.N. Wiro, T. Netsch, E.J. Vonken, G. Lund, et al., "Automatic Image-driven Segmentation of the Ventricles in Cardiac Cine MRI," *Journal of Magnetic Resonance Imaging*, Vol. 28 (2), Pages 366-374, 2008.
- [107] J. Huang, X. Huang, D. Metaxas, and L. Axel, "Dynamic Texture based Heart Localization and Segmentation in 4-D Cardiac Images," *Proceedings of the IEEE Intl Symposium on Biomedical Imaging: From Nano to Macro (ISBI)*, Pages 852-855, 2007.

- [108] M.P. Jolly, "Automatic Recovery of the Left Ventricular Blood Pool in Cardiac Cine MR Image," *Medical Image Computing and Computer-Assisted Intervention – MICCAI 2008*, Vol. 5241, Pages 110-118, 2008.
- [109] M.M.A. Hadhoud, M.I. Eladawy, A. Farag, F.M. Montevecchi, U. Morbiducci, "Left Ventricle Segmentation in Cardiac MRI Images," *American Journal of Biomedical Engineering*, p-ISSN: 2163-1050, e-ISSN: 2163-1077, Pages 131-135, 2012.
- [110] C. Cocosco, T. Netsch, J. Senegas, D. Bystrov, W. Niessen and M. Viergever, "Automatic Cardiac Region-of-interest Computation in Cine 3D Structural MRI," *Proceedings of the Conference on Computer Assisted Radiology and Surgery (CARS)*, Pages 1126-1131, 2004.
- [111] C. Petitjean, M.A. Zuluaga, W. Bai, J.N. Dacher, D. Grosgeorge, et al., "Right Ventricle Segmentation From Cardiac MRI: A Collation Study," *Medical Image Analysis*, Vol. 19, Pages 187-202, 2015.
- [112] N.C. Codella, M.D. Cham, R. Wong, C. Chu C, J.K. Min JK, et al., "Rapid and Accurate Left Ventricular Chamber Quantification Using a Novel CMR Segmentation Algorithm: A Clinical Validation Study," *Journal of Magnetic Resonance Imaging*, Vol. 31(4), Pages 845-853, 2010.
- [113] R.A. Young, "The Gaussian Derivative Model for Spatial Vision: I. Retinal Mechanisms," *Spatial Vision*, Vol. 2, Issue 4, Pages. 273-293, 1987.
- [114] J. Schaerer, C. Casta, J. Pousin, P. Clarysse, "A Dynamic Elastic Model for Segmentation and Tracking of the Heart in MR Image Sequences," *Medical Image Processing and Analysis*, Vol. 14, Pages 738-749, 2010.
- [115] A. Gupta, L. von Kurowski, A. Singh, D. Geiger, C.C Liang, M.Y. Chiu, "Cardiac MR Image Segmentation using Deformable Models," *Computers in Cardiology, Proceedings 1993*, Pages 747-750, 1993.
- [116] J.C. Fu, J.W. Chai, S.T.C Wong, "Wavelet-Based Enhancement for Detection of Left Ventricular Myocardial Boundaries in Magnetic Resonance Images," *Magnetic Resonance Imaging*, Vol. 18, Pages 1135-1141, 2000.
- [117] M. Hadhoud, M. Eladawy, A. Farag, "Automatic Global Localisation of The Heart from Cine MRI images," *IEEE International Symposium on IT in Medicine & Education*, Pages 35-38, 2011.
- [118] S. P. Dakua, J. S. Sahambi, "LV Contour Extraction Using Difference of Gaussian Weighting Function and Random Walk Approach," *India Conference (INDICON), 2009 Annual IEEE*, Pages 1-4, 2009.
- [119] A. Andreopoulos, J.K. Tsotsos, "Efficient and Generalisable Statistical Models of Shape and Appearance for Analysis of Cardiac MRI," *Medical Image Analysis*, Vol. 12, Issue 3, Pages 335-357, 2008.
- [120] M. Santarelli, V. Positano, C. Michelassi, M. Lombardi and L. Landini, "Automated Cardiac MR Image segmentation: Theory and Measurement Evaluation," *Medical Engineering and Physics*, Vol. 25 (2), Pages 149-159, 2003.
- [121] Y. Wang and Y. Jia, "Segmentation of the Left Ventricle from Cardiac MR Images Based On Degenerated Minimal Surface Diffusion and Shape Priors," *Proceedings of the 18th International Conference on Pattern Recognition*, Vol. 4, Pages 671-674, 2006.

- [122] R. El Berbari, I. Bloch, A. Redheuil, E. Angelini, E. Mousseaux, et al., "An Automated Myocardial Segmentation in Cardiac MRI," *Proceedings IEEE Engineering in Medicine and Biology Society*, Pages 4508-4511, 2007.
- [123] Y. Wu, Y. Wang and Y. Jia, "Segmentation of The Left Ventricle in Cardiac Cine MRI Using a Shape-Constrained Snake Model," *Computer Vision and Image Understanding*, Vol. 117(9), Pages 990-1003, 2013.
- [124] Q. Pham, F. Vincent, P. Clarysse, P. Croisille and I. Magnin, "A FEM-Based Deformable Model for the 3D Segmentation and Tracking of the Heart in Cardiac MRI," *Proceedings of the 2nd International Symposium on Image and Signal Processing and Analysis*, Pages 2506-254, 2001.
- [125] T. Pieciak, "Segmentation of the Left Ventricle Using Active Contour Method With Gradient Vector Flow Forces in Short-Axis MR," *ITIB*, Vol. 7339, Pages 24-35, 2012.
- [126] P. Gotardo, K. Boyer, J. Saltz and S. Raman, "A New Deformable Model for Boundary Tracking in Cardiac MRI and Its Application to the Detection of Intra-Ventricular Dyssynchrony," *IEEE Computer Society Conference on Computer Vision and Pattern Recognition*, Vol. 1, Pages 7366-743, 2006.
- [127] R. Battani, C. Corsi, A. Sarti, C. Lamberti, T. Piva and R. Fattori, "Estimation of Right Ventricular Volume Without Geometrical Assumptions Utilizing Cardiac Magnetic Resonance Data," *Computers in Cardiology*, Pages 816-84, 2003.
- [128] M. Ammar, S. Mahmoudi, M.A. Chikh and A. Abbou, "Endocardial Border Detection in Cardiac Magnetic Resonance Images Using Level Set Method," *Journal on Digital Imaging*, Vol. 25(2), Pages 294-306, 2012.
- [129] C. Pluempitawiriyawej, J. Moura, Y. Wu and C. Ho, "STACS: New Active Contour Scheme for Cardiac MR Image Segmentation," *IEEE Transactions on Medical Imaging*, Vol. 24(5), Pages 5936-603, 2005.
- [130] N. Paragios, "A Variational Approach for the Segmentation of the Left Ventricle in Cardiac Image Analysis," *International Journal of Computer Vision*, Vol. 50(3), Pages 345-362, 2002.
- [131] A. Yezzi, S. Kichenassamy, A. Kumar, P. Olver and A. Tannenbaum, "A Geometric Snake Model for Segmentation of Medical Imagery," *IEEE Transactions on Medical Imaging*, Vol. 16(2), Pages 199-209, 1997.
- [132] M. Lynch, O. Ghita and P. Whelan, "Segmentation of the Left Ventricle of the Heart in 3D+T MRI Data Using an Optimised Non-Rigid Temporal Model," *IEEE Transactions on Medical Imaging*, Vol. 27(2), Pages 195-203, 2008.
- [133] I. Ben Ayed, S. Li and I. Ross, "Embedding Overlap Priors in Variational Left Ventricle Tracking," *IEEE Transactions on Medical Imaging*, Vol. 28(12), Pages 1902-1913, 2009.
- [134] T.A. Ngo and C. Gustavo, "Left Ventricle Segmentation from Cardiac MRI Combining Level Set Methods with Deep Belief Networks," *20th IEEE International Conference on Image Processing*, Pages 695-699, 2013.
- [135] S. Ordas, H. van Assen, L. Boisrobert, M. Laucelli, J. Puente, et al, "Statistical Modeling and Segmentation in Cardiac MRI Using a Grid Computing Approach," *Advances In Grid Computing*, Pages 66-15, 2005.

- [136] M. Stegmann and D. Pedersen, "Bi-Temporal 3D Active Appearance Models With Applications to Unsupervised Ejection Fraction Estimation," *International Symposium on Medical Imaging* 2005, Vol. 5747, Pages 3366-350, 2005.
- [137] J. Abi-Nahed, M.P. Jolly and G.Z. Yang, "Robust Active Shape Models: A Robust, Generic and Simple Automatic Segmentation Tool," *Proceedings of Medical Image Computing and Computer-Assisted Intervention*, Vol. 2, Pages 168, 2006.
- [138] S. Zambal, J. Hladuvka and K. Buhler, "Improving Segmentation of the Left Ventricle Using a Two-Component Statistical Model," *Proceedings of Medical Image Computing and Computer-Assisted Intervention*, Pages 1516-158, 2006.
- [139] H. Zhang, A. Wahle, R. Johnson, T. Scholz and M. Sonka, "4-D Cardiac MR Image Analysis: Left and Right Ventricular Morphology and Function," *IEEE Transactions on Medical Imaging*, Vol. 29 (2), Pages 350 - 364, 2010.
- [140] M. Lorenzo-Valdes, G. Sanchez-Ortiz, A. Elkington, R. Mohiaddin and D. Rueckert, "Segmentation of 4D Cardiac MR Images Using a Probabilistic Atlas and the EM Algorithm," *Medical Image Analysis*, Vol. 8(3), Pages 255-265, 2004.
- [141] J. Lotjonen, S. Kivisto, J. Koikkalainen, D. Smutek and K. Lauerma, "Statistical Shape Model of Atria, Ventricles and Epicardium from Short and Long-Axis MR Images," *Medical Image Analysis*, Vol. 8(3), Pages 371-386, 2004.
- [142] X. Zhuang, K. Rhode, S. Arridge, S. Razavi, D. Hill, et al. "An Atlas-Based Segmentation Propagation Framework Using Locally Affine Registration - Application To Automatic Whole Heart Segmentation," *Medical Image Computing and Computer-Assisted Intervention* 2008, Pages 425-433, 2008.
- [143] X. Zhuang, K. Rhode, S. Razavi, D. Hawkes and S. Ourselin, "A Registration-Based Propagation Framework for Automatic Whole Heart Segmentation of Cardiac MRI," *IEEE Transactions on Medical Imaging*, Vol. 29(9), Pages 1612-1625, 2010.
- [144] M. A. Zuluaga, M.J. Cardoso, M. Modat and S. Ourselin, "Multi-Atlas Propagation Whole Heart Segmentation from MRI and CTA Using a Local Normalised Correlation Coefficient Criterion," *Functional Imaging and Modeling of the Heart*, Pages 174-181, 2013.
- [145] Y. Ou, J. Doshi, G. Erus and C. Davatzikos, "Multi-Atlas Segmentation of the Right Ventricle in Cardiac MRI," *Proceedings of MICCAI RV Segmentation Challenge*, 2012.
- [146] W. Bai, W. Shi, H. Wang, N.S. Peters and D. Rueckert, "Multi-Atlas Based Segmentation with Local Label Fusion for Right Ventricle MR Images," *Proceedings of MICCAI RV Segmentation Challenge*, 2012.
- [147] X. Zhuang, D.J. Hawkes, W.R. Crum, R. Boubertakh, S. Uribe, et al. "Robust Registration Between Cardiac MRI Images and Atlas for Segmentation Propagation," *Medical Imaging - International Society for Optics and Photonics*, Pages 691408-691408, 2008.
- [148] H.A. Kirisli, M. Schaap, S. Klein, L.A. Neeffjes, A.C. Weustink, et al. "Fully Automatic Cardiac Segmentation from 3D CTA Data: A Multi-Atlas Based Approach," *Medical Imaging - International Society for Optics and Photonics*, Pages 762305-762305, 2010.

- [149] C. Hoogendoorn, N. Duchateau, D. Sanchez-Quintana, T. Whitmarsh, F.M. Sukno, et al, "A High-Resolution Atlas and Statistical Model of the Human Heart from Multislice CT," *IEEE Transactions on Medical Imaging*, Vol. 32(1), Pages 28-44, 2013.
- [150] G. Yang, Y. Chen, L. Tang, H. Shu, and C. Toumoulin, "Automatic Left Ventricle Segmentation Based on Multiatlas Registration in 4D CT Images," *IEEE 11th International Symposium on Biomedical Imaging*, Pages 413-416, 2014.
- [151] I. Išgum, M. Staring, A. Rutten, M. Prokop, M. Viergever and B. Van Ginneken, "Multi-Atlas-Based Segmentation With Local Decision Fusion" Application to Cardiac and Aortic Segmentation in CT Scans," *IEEE Transactions on Medical Imaging*, Vol. 28(7), Pages 1000-1010, 2009.
- [152] D Mahapatra, "Cardiac MRI Segmentation using Mutual Context Information from Left and Right Ventricle," *Journal on Digital Imaging*, Vol. 26(5), Pages 898-908, 2013.
- [153] D.R. Chittajallu, S.K. Shah and I.A. Kakadiaris, "A Shape Driven MRF Model for the Segmentation of Organs in Medical Images," *Computer Vision and Pattern Recognition*, Pages 3233-3240, 2010.
- [154] J.F. Dreijer, B.M. Herbst and J.A. Du Preez, "Left Ventricular Segmentation from MRI Datasets with Edge Modelling Conditional Random Fields," *Biomedical Central medical imaging*, Vol. 13(1), Pages 13-24, 2013.
- [155] S. Osher and J. Sethian, "Fronts Propagating with Curvature-Dependent Speed: Algorithms Based on Hamilton's Cahn-Cahn Formulation," *Journal Computer Physics*, Vol. 79, Pages 12-49, 1988.
- [156] V. Caselles, F. Catte, T. Coll and F., "A Geometric Model for Active Contours," *Numerische Mathematik*, Vol. 66, Pages 1-31, 1993.